POLITECNICO DI MILANO

School of Industrial and Information Engineering

M. Sc. Course of
Energy Engineering

Innovative techniques to reduce energy consumption of household refrigerators

Advisor: Prof. Cesare Maria Joppolo

Co-advisor: Prof. Marco Carlo Masoero
Prof. Luca Molinaroli

M. Sc. Thesis of:

Marcello Fantini
Matr. 782587

Academic Year 2012 - 2013

Table of Contents:

Index of figures:

Index of tables:

Sommario

Negli ultimi decenni la legislazione correlata ai refrigeratori domestici ha forzato i produttori a ridurre i consumi energetici di questi elettrodomestici. Pertanto si è deciso di studiare una particolare tecnologia di refrigeratori, chiamata Doppio Evaporatore Sequenziale, che ha mostrato caratteristiche positive in termini di consumi energetici.
In questa tesi l'attenzione si è focalizzata sulla misurazione e sulla previsione dei consumi energetici di un prototipo di refrigeratore su cui si sono provate diverse tecnologie innovative.
Nei capitoli secondo e terzo, si sono cercati di ottimizzare alcuni parametri del refrigeratore costruendo il sistema di acquisizione delle grandezze rilevanti della refrigeratore e conducendo una campagna sperimentale per capire i possibili miglioramenti che si potrebbero avere adottando dei materiali in cambiamento di fase con diverse temperature di congelamento all'interno dello scomparto frigorifero.
Nel quarto capitolo, si è condotta un'altra campagna di misurazioni per avere input sperimentali per il modello di simulazione dell'intero ciclo. In particolare si sono caratterizzati diversi ventilatori e multiflow (ovvero canalizzazioni per l'aria) installati sulla parete posteriore della cavità del refrigeratore al fine di aumentare lo scambio termico lato aria tra evaporatore e aria interna allo scomparto.
Nei quattro capitoli successivi del lavoro, si è cercato di integrare il codice di simulazione del ciclo con un nuovo modello di compressore che predica con accuratezza la potenza richiesta, la portata di refrigerante e la quantità di refrigerante disciolta nell'olio lubrificante. In particolare si è sviluppato sia un modello politropico che un modello differenziale del compressore confrontando i risultati prodotti e sottolineando vantaggi e svantaggi di ogni modello. Si è anche creato un semplice modello per prevedere la solubilità del refrigerante nell'olio del compressore basandosi sulla legge di Raoult.
Infine nell'ultimo capitolo della tesi sono mostrati i risultati delle simulazioni stazionarie dell'intero ciclo in termini di consumi energetici di alcune particolari configurazioni del prototipo.
Alla fine della tesi i risultati del lavoro hanno suggerito alcune possibili strade per alcuni miglioramenti futuri dei refrigeratori con tecnologia a Doppio Evaporatore Sequenziale.

Parole chiave: refrigeratori SDE, modellizzazione di compressori, scambio termico dell'aria, temperatura di congelamento del PCM.

Abstract

In the last decades the legislation related to the household refrigerators forced the manufacturers to reduce the energy consumptions of the appliances. Thus we decided to study a particular refrigeration technology, called Sequential Dual Evaporator, that showed relevant benefits in lowering the energy expenses.
In this thesis we chose to focus on the measure and the prevision of the energy consumptions of a refrigerator prototype coupled with different innovative technologies.
In the second and third chapters, we built up the acquisition system of the relevant parameters of the refrigerator and we ran several tests to optimize the freezing temperature of the Phase Change Material that is positioned in the refrigerator cabinet.
In the fourth chapter we conducted an experimental campaign to gather some experimental inputs for the simulation model of the entire thermodynamic cycle. We made several tests to understand the possible heat transfer improvements between the evaporator and the refrigerator internal air related to the adoption of different fans and multiflows (i.e. air channels) positioned on the back wall of the cabinet.
In the next four chapters of the thesis, we tried to merge a new compressor model into the cycle simulation code to predict accurately the required compressor power, the refrigerant mass flow rate and the quantity of refrigerant dissolved in the lubricant oil. In particular we developed both a polytrophic and a differential model for the compressor and we compared the predicted values of the outputs to understand the benefits and the disadvantages of every model. We also generated a simple solubility model of the refrigerant in the compressor oil using the Raoult's law.
In the last chapter we showed the results of the stationary simulation of the thermodynamic cycle in terms of energy consumptions of different configurations of the prototype.
At the end of the thesis we proposed some suggestions for future improvements of the Sequential Dual Evaporator refrigerators.

Keywords: SDE refrigerators, compressor modeling, air heat transfer, PCM freezing temperature.

Sommario esteso

Negli ultimi decenni la legislazione correlata ai refrigeratori domestici ha forzato i produttori a ridurre i consumi energetici di questi elettrodomestici. In particolare sono state implementate due diverse tipologie di legislazioni: il labelling e l'ecodesign. La prima categoria di normative ha introdotto le classi di consumo energetico, permettendo al cliente di avere informazioni chiare e intuitive riguardo all'argomento. La legislazione ha consentito di orientare il mercato verso un'ottica di competitività riguardo ai consumi energetici dei refrigeratori. Il risultato di questo fenomeno si è visto negli ultimi anni in cui è avvenuto un netto movimento dei refrigeratori verso classi meno energivore. La seconda tipologia di normative ha permesso ai produttori di creare degli accordi per promuovere una progettazione più ecologica di prodotti venduti in grandi quantità e che dunque hanno un impatto significativo sui consumi energetici finali nel settore residenziale. La seconda estensione normativa ha creato i presupposti per l'analisi e l'efficientamento di ogni passo della progettazione dei refrigeratori. All'inizio del lavoro di tesi è stata fatta un'analisi delle tecnologie di refrigeratori domestici esistenti, al fine di individuare quella che meglio si armonizzi con l'attuale quadro normativo e con i conseguenti trend di mercato. L'analisi introduttiva ha portato all'individuazione dell'oggetto di tesi nei refrigeratori con tecnologia a Doppio Evaporatore Sequenziale (SDE). Tale tecnologia si basa sull'utilizzo di due evaporatori diversi per lo scomparto del frigorifero e per quello del freezer permettendo così l'ottimizzazione individuale di ogni circuito. Il flusso di refrigerante è guidato tramite una valvola bi-stabile che lo indirizza alternativamente verso uno dei due evaporatori.
In questa tesi la nostra attenzione si è focalizzata sulla misurazione e sulla previsione dei consumi energetici di un prototipo di refrigeratore su cui si sono provate diverse tecnologie innovative. Da una parte si è svolta un'attività sperimentale per misurare i consumi del refrigeratore in alcune particolari configurazioni, dall'altra parte si è utilizzato un modello di simulazione stazionario dell'intero ciclo in cui si sono inseriti degli input sperimentali per prevedere i consumi del prototipo in altre situazioni caratteristiche.
In primis si è costruito un apparato sperimentale che permettesse di raggiungere un duplice scopo. Da una parte l'esigenza è stata quella di acquisire i valori di pressione, temperatura e potenza del prototipo di refrigeratore, dall'altra si è anche voluto riuscire a controllare gli organi interni alla macchina per regolarne il funzionamento in vista di futuri test. Si sono dunque studiati, selezionati e acquistati tutti i componenti hardware utili per il nostro problema. Il risultato di tutte queste operazioni si è concretizzato nella creazione di un box di controllo in cui sono stati inseriti tutti i componenti elettrici ed elettronici utili per i due obiettivi. Successivamente, tramite piccole modifiche a un programma Labview

già disponibile, si è potuto comandare il refrigeratore e acquisirne i parametri voluti, tramite un personal computer.
Successivamente, si è svolta un'altra attività sperimentale al fine di ottimizzare la temperatura di congelamento del materiale in cambiamento di fase posto all'interno dello scomparto frigorifero del prototipo. Usando l'apparato sperimentale precedentemente creato, si sono potuti acquisire la potenza del compressore e diverse temperature che hanno permesso la scelta di una temperatura di congelamento ottima per ridurre i consumi energetici. L'obiettivo dell'attività sperimentale è stato quello di ridurre i consumi del refrigeratore in particolari condizioni fissate dalla specifica norma riguardante gli "*energy consumption tests*". In seguito si è cercato di regolare al meglio tutte le strumentazioni in nostro possesso per poter lanciare i test nelle condizioni prescritte dalla norma. Questa operazione è stata completata con successo per tutti i parametri richiesti, tranne che per la temperatura ambiente. Infatti si è potuto regolare quest'ultima solo mediamente, ma non puntualmente, affinché rientrasse nel range voluto dallo standard. Anche se quindi i test non possono essere equiparati a degli "*energy consumption tests*" i risultati non vengono significativamente influenzati dagli andamenti puntuali della temperatura ambiente, bensì dalla media temporale e pertanto i risultati sono stati considerati validi per lo scopo prefisso. Una volta applicate le costrizioni presenti nella normativa, si sono potuti lanciare i test. Inizialmente sono stati svolti dei test per tre predeterminate frequenze del compressore senza la presenza di materiale in cambiamento di fase. In seguito si sono svolti altri test per le stesse frequenze usando dell'acqua come materiale in cambiamento di fase. Ogni singolo test ha richiesto circa una giornata e mezza di misure ininterrotte in modo da ottenere risultati affidabili in condizioni stazionarie, in cui il frigorifero attraversa dei cicli di funzionamento simili tra loro. Al fine di scegliere la frequenza migliore del compressore per la quale eseguire altri test supplementari, si è considerato come indicatore di scelta il COP medio sui periodi di misura. Andando dunque a calcolare e analizzare quale dei test avesse il COP medio più alto, la frequenza di 54 Hz è risultata quella ottima dal punto di vista dei consumi energetici. Facendo funzionare il compressore a questa frequenza, sono stati lanciati altri test aggiungendo NaCl all'acqua per ottenere diverse temperature di cambiamento di fase (-2 °C e - 4°C). Unendo i risultati in termini di COP medio a quelli relativi al tempo di funzionamento del compressore, si è potuto individuare la temperatura ottimale di cambiamento di fase, pari a -1°C Per questa temperatura si attende un miglioramento del COP medio, rispetto al caso senza materiale in cambiamento di fase, di circa il 10%.
In seguito la nostra attenzione si è rivolta allo studio dello scambio termico lato aria tra l'evaporatore e l'aria interna della cavità frigorifera di un refrigeratore identico al prototipo, ma senza materiale in cambiamento di fase nella cavità. I risultati di questa campagna sperimentale sono stati poi integrati nell'ultimo capitolo della tesi allo scopo di prevedere i consumi di un possibile futuro

prototipo di refrigeratore con materiali in cambiamento di fase, nuovi ventilatori e multiflow (ovvero canalizzazioni per l'aria) nella cavità frigorifera. In particolare la macchina analizzata è composta da un evaporatore affogato nella parete posteriore della cavità frigorifera e dunque il nostro interesse si è focalizzato su come aumentare lo scambio termico lato aria su questa parete. In particolare l'obiettivo fissato si è rilevato essere duplice: da una parte si sono volute provare le configurazioni esistenti presenti in frigoriferi simili a quello sezionato, dall'altra parte sono state caratterizzate nuove configurazioni combinando diversi ventilatori e multiflow al fine di incrementare lo scambio termico. Tutti i test sono stati condotti tramite la misura delle velocità dell'aria utilizzando anemometri a filo caldo con adeguate caratteristiche di accuratezza. I test sono stati svolti con il frigorifero spento, la porta frontale chiusa e i tre ripiani interni nelle posizioni standard identificate dalla relativa normativa. Utilizzando poi le misure di velocità dell'aria si è potuto stimare lo scambio termico tramite l'utilizzo di specifiche correlazioni. Al fine di stimare i possibili miglioramenti nello scambio termico, si è dovuta definire quantitativamente una configurazione base. Questa configurazione consiste nel considerare solo la convezione forzata e l'irraggiamento come fenomeni per lo scambio termico tra l'aria interna al frigorifero e la superficie posteriore della cavità frigorifera. Si è proceduto poi a caratterizzare due ventilatori e una tipologia di multiflow già presente. I risultati delle misure delle velocità e delle conseguenti applicazioni delle correlazioni hanno mostrato come le configurazioni esistenti non abbiano un impatto significativo in termini di aumento dello scambio termico. Queste configurazioni sono infatti state progettate per esigenze di marketing al fine di dare ai clienti un'immagine di freschezza e pulizia dell'interno del frigorifero. Successivamente è stato caratterizzato un ventilatore centrifugo al quale sono stati accoppiati diversi multiflow progettati appositamente per sfruttare al meglio le caratteristiche di questa macchina. In questo caso si sono riusciti ad ottenere sensibili incrementi dello scambio termico fino al 40 % in più rispetto al caso base. Alla fine di questi test è stato possibile identificare chiaramente che una caratteristica rilevante del flusso d'aria necessario per incrementare lo scambio termico consiste nella uniformità del profilo di velocità. A questo proposito è stato individuato e ordinato un ventilatore tangenziale dal quale ci si aspettava una maggior uniformità del flusso d'aria soffiato. I test successivi hanno validato questa ipotesi identificando nel ventilatore tangenziale la migliore tecnologia tra quelle provate per incrementare lo scambio termico. Anche in questo caso la macchina è stata caratterizzata accoppiandola a un multiflow progettato per lo scopo. Il ventilatore tangenziale ha mostrato brillanti caratteristiche sia per quanto riguarda l'uniformità del flusso d'aria soffiato, sia per quanto riguarda la potenza richiesta. Infatti, ad esempio, utilizzando questo ventilatore si è riuscito ad ottenere lo stesso incremento di scambio termico della migliore configurazione in cui è stato usato il ventilatore centrifugo (circa 40%) con un terzo della potenza elettrica associata. I risultati di tutte le misure

sperimentali della velocità dell'aria ci hanno permesso di concludere che l'adozione di un ventilatore tangenziale e di un multiflow potrebbe essere una strada percorribile per incrementare lo scambio termico interno alla cavità frigorifera. In particolare questa attività sperimentale ha mostrato come il fenomeno dei moti dell'aria sulla parete posteriore del frigorifero sia un fenomeno complesso che meriterebbe di essere analizzato tramite simulazioni CFD. Inoltre date le esigue potenze richieste da questo tipo di ventilatori sembra che questa tecnologia possa anche portare a un risparmio sui consumi energetici globali del refrigeratore. Altri studi e ricerche sono oggigiorno portate avanti in questa direzione.

Nei quattro capitoli successivi del lavoro, si è cercato di integrare il codice di simulazione dell'intero ciclo termodinamico con un nuovo modello di compressore che predica con accuratezza la potenza richiesta, la portata di refrigerante e la quantità di refrigerante disciolta nell'olio lubrificante.

Dopo aver analizzato i modelli di compressori presenti in letteratura, si è inizialmente optato per la creazione di un modello basato sull'assunzione che il refrigerante segua una trasformazione politropica durante il processo di compressione. Il modello predice la potenza richiesta dal compressore e la temperatura alla quale si porta l'esterno del compressore. Per ottenere gli output, il modello richiede in input sia alcuni parametri peculiari del compressore (l'efficienza volumetrica , l'efficienza meccanica e quella elettrica, alcuni dati geometrici e l'esponente della politropica) sia le condizioni operative di funzionamento (la temperatura ambiente, la temperatura e la pressione del refrigerante in aspirazione, la velocità di rotazione del compressore e la pressione del refrigerante in mandata). In particolare si è identificato l'esponente della politropica per la nostra compressione minimizzando l'errore medio tra i valori previsti dal modello e i dati sperimentali. Questo tipo di modellizzazione si basa sull'assunzione di poter considerare il refrigerante come un gas ideale durante il processo di compressione. La validità di tale assunzione è stata descritta criticamente evidenziandone vantaggi e svantaggi. In letteratura sono presenti diversi modelli di tipo politropico che hanno mostrato come questa semplificazione della realtà possa comunque portare ad ottenere dei buoni risultati; quelli ottenuti con il modello proposto sono stati poi confrontati con i dati misurati presenti nella scheda tecnica del compressore. Confrontando i valori calcolati con i novanta punti sperimentali, si è ottenuto un errore che varia da -15% a +14% con un errore medio del 7 %. In particolare il modello predice accuratamente i valori sperimentali per i valori più bassi di potenza richiesta. Questi punti corrispondo a valori di bassi rapporti di compressione ed in particolare a punti in cui sia ha la più bassa temperatura di condensazione considerata. Il comportamento del modello si spiega analizzando l'ipotesi di gas ideale, che risulta infatti esser significativamente valida proprio per i valori di rapporto di compressione e temperatura di condensazione per i quali il modello predice più meticolosamente i valori sperimentali. Alla fine dello sviluppo del

modello politropico, è nata l'esigenza di predire sia la potenza richiesta dal compressore che la portata fornita con un grado di precisione maggiore. In particolare ci si è posti l'obiettivo di riuscire a calcolare questi due parametri con la stessa incertezza presente nelle misure sperimentali. Pertanto si è deciso di mantenere il modello politropico solo per calcoli preliminari e di implementare un altro modello di compressione per ottenere l'accuratezza voluta dei risultati.
Successivamente si è sviluppato un modello diverso che si basa sulle equazioni differenziali riguardanti il bilancio di massa ed energia al'interno della camera di compressione. Facendo opportune ipotesi semplificative per la risoluzione delle equazioni, è stato possibile ottenere la potenza richiesta dal compressore e la portata di refrigerante associata. Si sono poi utilizzati alcuni coefficienti correttivi per tradurre gli output delle equazioni dal caso semplificato di compressione adiabatica per cui sono stati calcolati al caso di compressione reale. Tutti i coefficienti correttivi sono stati identificati minimizzando l'errore medio tra i valori predetti dal modello e i dati sperimentali. Parallelamente si è anche sviluppato un semplice modello termico del compressore, basato su correlazioni di scambio termico nelle diverse parti della macchina, che permette di calcolare il calore liberato e la temperatura del guscio esterno. Le equazioni differenziali sono state risolte tramite il software Engineering Equation Solver (EES) mentre la minimizzazione tra dati previsti e valori reali è stata fatta in Microsoft Excel. Gli input per risolvere le equazioni differenziali in EES sono stati sia alcune caratteristiche geometriche del compressore (cilindrata, corsa, area del canale di aspirazione e di mandata) sia le condizioni operative (la temperatura ambiente, la pressione del refrigerante in aspirazione, la velocità di rotazione del compressore e la pressione del refrigerante in mandata). Gli output del calcolo effettuato in EES si identificano nella potenza e nell'efficienza volumetrica nelle condizioni ideali di compressione adiabatica. A questo punto è stata condotta un'analisi di sensitività su alcuni parametri peculiari del modello, al fine di individuare i valori che permettessero di ottenere il maggiore accordo tra i valori predetti di potenza e portata di refrigerante e i dati sperimentali. Si sono poi calcolati i coefficienti correttivi per trasferire i risultati dal caso di compressione adiabatica a quello di compressione reale minimizzando l'errore medio tra valori previsti e dati sperimentali. Una volta identificati i coefficienti correttivi si è potuta sviluppare la parte termica del modello tramite l'implementazione di alcune correlazioni di scambio termico. I risultati del modello sono risultati essere in accordo con le misure sperimentali. Infatti, per quanto riguarda la potenza del compressore, i valori previsti dal modello mostrano di avere un errore medio di 2.4 % rispetto agli 81 punti sperimentali sui quali è stato provato. Il modello riesce a prevedere con un'accuratezza del 5% 77 degli 81 punti sperimentali, assumendo un valore di errore massimo del 9.1 %. Inoltre, per quanto concerne la portata di refrigerante, i risultati previsti dal modello si caratterizzano con un errore medio di 1.5 % rispetto agli 81 punti sperimentali sui quali è stato provato. Infine la modellizzazione prevede la

temperatura del guscio della macchina con un'accuratezza del 10 %. Inoltre il modello è stato anche applicato su altri compressori di tipo reciproco dello stesso produttore. Per i compressori con caratteristiche geometriche più simili a quello inizialmente considerato, la modellizzazione ha mostrato buoni risultati in termini di accordo tra valori previsti e dati sperimentali. Per i compressori con caratteristiche geometriche molto diverse rispetto a quelle del nostro caso base, il modello riesce a prevedere con un'accuratezza minore i valori richiesti. Questo fatto si spiega riconoscendo che il modello è stato sviluppato anche attraverso un'analisi di sensitività personalizzata sul compressore considerato. Pertanto, fino a quando le caratteristiche geometriche di altri compressori risultano essere simili a quello iniziale, il modello risulta essere accurato mantenendo gli stessi parametri identificati con l'analisi di sensitività iniziale. In caso contrario, bisognerebbe calibrare nuovamente la modellizzazione tramite una nuova analisi di sensitività sui parametri. Inoltre si è anche svolto un confronto tra il modello politropico e il modello differenziale evidenziando benefici e costi computazionali di ognuno. Il paragone è stato infine allargato comprendendo anche il classico modello matematico utilizzato dalle aziende per i compressori, che si basa su un'interpolazione dei dati sperimentali tramite 10 coefficienti.
Si è poi passati a sviluppare un modello di solubilità del refrigerante (nel nostro caso isobutano) nell'olio del compressore per provare a validare l'ipotesi di basso contenuto di massa di refrigerante nel compressore. Infatti nei refrigeratori con tecnologia SDE la distribuzione della massa di refrigerante nei diversi componenti della macchina è un fenomeno basilare per poter procedere all'ottimizzazione del ciclo. Nel capitolo 8 si è dimostrato che la quantità di refrigerante presente nel compressore, ovvero disciolta nell'olio lubrificante, può essere effettivamente trascurata nei calcoli riguardanti la distribuzione di massa di refrigerante nel refrigeratore. Si è dunque sviluppato un semplice modello basato sull'equilibrio chimico delle specie espresso tramite ipotesi semplificative con la legge di Raoult. Per questo studio preliminare l'obiettivo è stato quello di prevedere la solubilità dell'isobutano nell'olio del compressore per diverse condizioni operative con un'accuratezza del 20 %. I risultati ottenuti mostrano un accordo tra le previsioni del modello e i dati sperimentali caratterizzato da un errore medio del 4.2 % e un errore massimo compreso nella banda di accuratezza voluta. Infine si è anche provato ad applicare il modello di solubilità ad altre miscele di refrigeranti e oli ottenendo risultati più o meno accurati a seconda del grado di idealità della miscela. Quanto più la miscela analizzata mostra un comportamento simile a una miscela ideale, tanto più il nostro modello e le nostre ipotesi risultano delineare precisamente il problema.
Infine nell'ultimo capitolo sono stati riportati i risultati delle simulazioni stazionarie dell'intero ciclo in termini di consumi del refrigeratore. In primis, si sono provate a simulare le diverse condizioni del materiale in cambiamento di fase nelle quali si sono misurati i consumi nel terzo capitolo. Questo primo passo ci ha permesso di provare e validare il modello di simulazione.

Successivamente si è provato a simulare un possibile prototipo di refrigeratore in cui siano posti un materiale in cambiamento di fase, i ventilatori e multiflow analizzati nel quarto capitolo, allo scopo di provare a stimare i risparmi energetici delle diverse configurazioni. In particolare si è identificata una configurazione ottima in cui assieme al materiale in cambiamento di fase viene anche posto un ventilatore tangenziale con il relativo multiflow all'interno della cavità frigorifera.
Alla fine del lavoro di tesi sono state individuate due direzioni future per ulteriori miglioramenti dei refrigeratori SDE. Da una parte viene proposto di produrre un nuovo prototipo di refrigeratore in cui si uniscano le caratteristiche positive riguardanti l'utilizzo del materiale in cambiamento di fase e del ventilatore tangenziale all'interno della cavità frigorifera. Questo prototipo dovrebbe essere sviluppato sia utilizzando i risultati del lavoro di tesi, sia conducendo un'analisi approfondita dei movimenti dell'aria all'interno del refrigeratore tramite l'utilizzo di software CFD. Dall'altra parte si reputa che la creazione di un modello dinamico di simulazione dell'intero ciclo termodinamico del prototipo possa essere un passo fondamentale per l'individuazione di futuri miglioramenti dal punto di vista dei consumi energetici. Questo modello dinamico potrebbe partire dal modello differenziale di compressore sviluppato in questo lavoro di tesi per poi proseguire sviluppando e armonizzando i modelli dinamici degli altri componenti presenti nel ciclo frigorifero.

Introduction

In this thesis we focus on the development of the Sequential Dual Evaporator (SDE) refrigeration technology for the household appliances that already showed positive attributes in terms of energy consumptions. We divided the work in an experimental and a simulation part. Both the two sections were then merged in the last chapter of the thesis to run stationary simulations of the entire cycle to predict the energy consumptions in new possible configurations.
The first two chapters of the work regards the experimental activities that we performed on a SDE prototype at Politecnico di Milano. The aim of this section was to select the most appropriate freezing temperature of a PCM positioned into the refrigerator cabinet to lower the energy expenses. At the beginning, we made the experimental apparatus to acquire the relevant pressures, temperatures and to measure the compressor power of the prototype. Building up the electronic circuits and using three National Instruments (NI) boards, we were able to perform and save the measurements through a Labview software directly on a personal computer. We analyzed the EN ISO 15502 standard for the testing of refrigerator and we tried to run the tests in the so called "energy consumption test" conditions.. The final result of this experimental campaign consisted in the identification of the PCM freezing temperature that minimized the energy consumptions of the appliance.
Furthermore we went through another experimental campaign to measure the overall heat transfer coefficient between the foamed-in evaporator and the refrigerator cabinet air. In particular we considered the variations of the air side heat transfer coefficient related to the adoption of different fans and multiflows (i.e. air channels) positioned on the back wall of the cabinet. In every test we measured the air speeds provided by the different fans (standard fan, centrifugal fan, tangential fan) and multiflows and then we computed the overall heat transfer coefficient of the back wall to individuate the best configuration in terms of heat transfer enhancement.
In the next four chapters of the thesis, we developed a new compressor model to be included in the available cycle simulation code. We wanted to predict accurately the required compressor power, the refrigerant mass flow rate and the quantity of refrigerant dissolved in the lubricant oil. At the beginning we created a polytrophic model that was not enough accurate for our purposes. So we chose another modeling approach based on the differential energy and mass balances in the compressor chamber. The increase of the complexity of the compressor model was balanced by a very good fitting between the simulated and the experimental values of the outputs. We finally made a comparison between the outputs of the two compressor models that we developed and the results of the compressor model prescribed by the EN 12900 standard to understand the advantages and the drawbacks of every approach. Furthermore we also

developed a simple solubility model of the refrigerant in the compressor oil based on the Raoult's law.
In the final chapter we merged the compressor differential model in the available stationary simulation code of the SDE refrigerator. At the beginning we tested the stationary simulation model making a comparison between the simulated values of energy consumption per day and COP and the experimental values that we measured in chapter 2. Finally we tried to simulate the energy consumptions of a possible future SDE prototype that utilizes both the PCM and the tangential fan in the RC cabinet.

1. State of the art

In the last 20 years the reduction of energy consumption has become a central issue in government policies. Governments implemented different policies for energy efficiency in order to save energy. Various policies have been introduced to deal with efficiency in different final energy uses. In this thesis we focus our attention on the residential sector. In 2010 the final energy consumption for the residential sector in the European Union (EU) 27 accounted for 26.65 % of the total final energy consumption [1] . Between 2005 and 2010 while the total final consumption fell by 3.29 %, the final consumption for the residential sector increased by 1.69 %. The reason behind this fact is linked with global trend of population. In fact, between 1999 and 2010, in the EU-27 we had both a growth of 4.05% of the population and an increase of the residential energy consumption of 5.7%. Economic growth is also positively related to the enlargement of the total final energy consumption. In the last years economic development in the EU-27 was also accompanied by more efficient ways of using energy.
In particular it is very interesting to study the electricity final use consumption. In 2010 the residential sector accounted for 29.71% of the total final electricity consumption. Between 2005 and 2010 we can see both that the total final electricity consumption grew by 2.42 % and that the final electricity consumption for the residential sector increased by 4.70 %. Although many appliances became more efficient in the last years we see that residential electricity consumption still increases. In particular, in 2009 in the EU-27 cold appliances electricity consumptions accounted for 14.5% of the total residential electricity consumption.
So if we consider that the reduction of consumptions is nowadays a crucial policy issue, the residential consumptions will deserve a deep study. In particular we choose to focus our attention on the cold appliances sector because some particular policies, especially in Italy, allowed manufacturers to have profit from their innovations in short periods of time.

1.1 Energy efficiency legislation in the residential sector in the EU

The policies for energy efficiency in the residential sector focused on identifying appliances consumptions through labels and on setting minimum consumption requirements (eco-design).
Labelling was first introduced by 92/75/EEC Directive and then it was revised by 2010/30/EU Directive. Directive 92/75/EEC introduced the European energy labeling scheme for household appliances. In particular the Directive applied

this scheme also to refrigerators, freezer and their combinations. In July 2011 directive 2010/30/EU replaced Directive 92/75/EEC and proposed a new labeling scheme. It introduced new energy consumption classes (A+, A++ and A+++) in addition to the existing classes (G-A). The indicator that distinguishes different classes is the Energy Efficiency Index (EEI). The Directive stated also that a maximum of seven energy classes should be maintained.
The first standard for the eco-design was the 2005/32/EC Directive that nowadays is implemented through the newer 2009/125/EC Directive. These two Directives are the main normatives for consumption regulation of product utilization. The eco-design directives are framework directives. This means that the two directives give only general conditions and criteria for the eco-design of the product without providing specific requirements for the different typologies of the products. Manufacturers should implement legislation regarding the specific requirements. In particular for refrigerators and freezer the Directive 2005/32/EC was implemented in July 2009. These directives allow manufacturers to make voluntary agreements for eco-design of very spread products (sales volume should be approximately more than 200.000 units per year) with substantial environmental impact (with a total final consumption of more than 1000 Petajoules per year).

1.2 Results of policies: actual situation of cold appliances

Energy efficiency policies had a great impact on the white appliance sector (i.e. cold appliances, washing machines, dishwashers and dryers). In Fig. 1.1 we show some results of these policies.

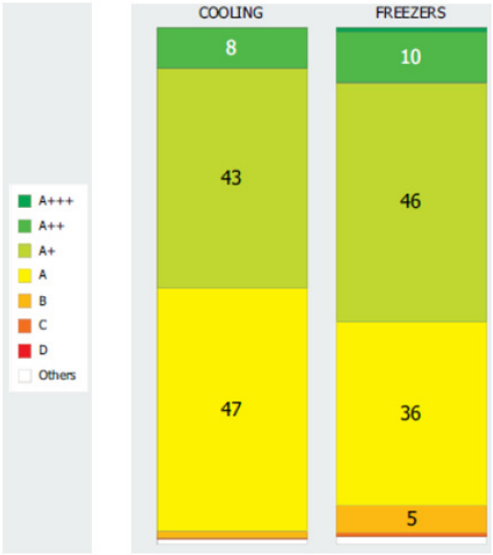

Figure 1.1 Percentages of refrigerators and freezers in the different energy classes[1].

As Bertoldi[1] states, the implementation of the EU directives by the manufacturers was very successful. As shown in Fig 1.1, for example, in the period between January and February 2011 already 51 % of the sold refrigerators and 56% of the sold freezers are in A+ ,A++ or A+++ class.
The author also points out that from 2005 to 2010 the white appliance sector showed a reduction of the average annual consumption per appliance. In the most prominent 23 EU countries we passed from 265 kWh in 2005 to 245 kWh in 2010 with a reduction of 7%. In particular Italy shows one of the best results with a decrease of the average annual consumption per appliance of 11 %.
The cold appliances sector has been a very positive example of implementation of the EU policies regarding energy efficiency. The report estimated that in 2005 in the EU-27 the refrigerator stock was around 190,577 million units and the freezer stock was around 54,292 million units. In 2005, 82 TWh/y were consumed by refrigerators and 82 TWh/y by freezers. A large number of these stocks turned into more efficient appliances between 2005 and 2010. This successful change was driven by both cost reducing policies of manufacturers and public policies of incentives. In Fig. 1.2 we show the results of this policies in terms of appliance price.

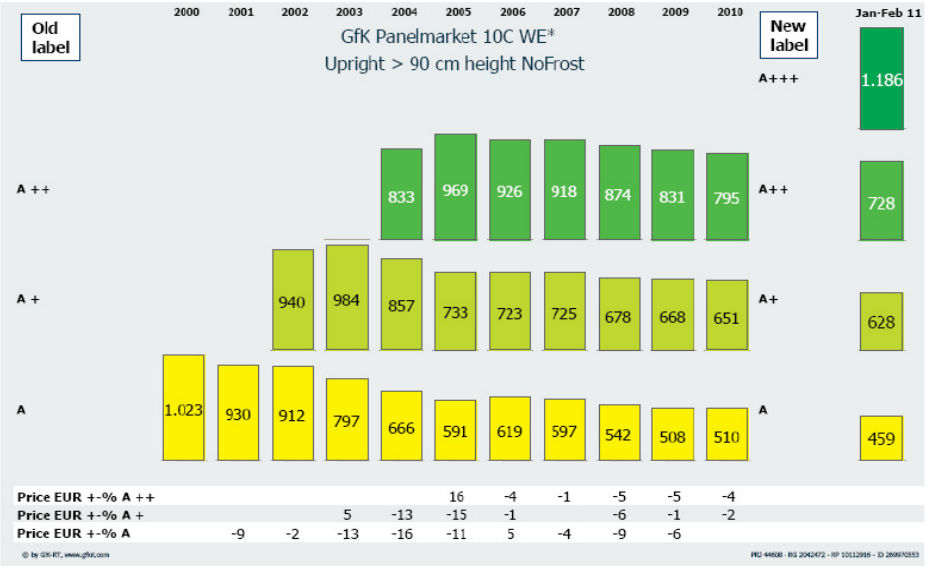

Figure 1.2 Average prices of energy classes of cold appliances and price gap in ten EU countries [1].

As we can see in Fig. 1.2, between 2005 and 2010 A++ appliances reduced their price of 25% and A+ appliances of 14%.
Between 2005 and 2010 the prices of the different classes allowed gradually to move the interest of the average customer from lower to upper classes. This

target was reached reducing the gap between the prices of the different classes. For example in Fig. 1.2 we can observe that the price gap between a A++ appliance and a A+ appliance moved from 236 € in 2005 to only 100 € in 2011. Furthermore in some countries the introduction of more efficient cold appliances was also helped by public policies. For example in January 2007 Italy set up a tax deduction programme in order to encourage the adoption of new freezer and refrigerators. The incentive allows the consumers that buy a new A+ or A++ cold appliance to deduct 20% of the cost of the refrigerator or freezer from their income tax. We show the brilliant results of this policy in Fig. 1.3.

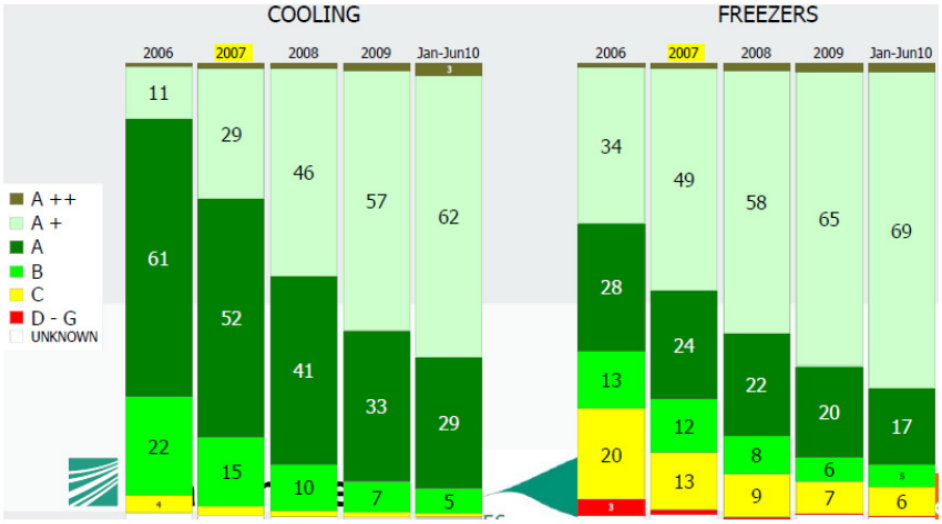

Figure 1.3 Shares of different energy classes in sales for domestic cold appliances in Italy [1].

In Fig. 1.3 we can see the percentages of the different energy classes in the total amount of sales of refrigerators and freezers in Italy. We can notice that the introduction of the incentive in 2007 increased the share of the A+ class from 11 % in 2006 to 29% in 2007 for refrigerators and from 34% in 2006 to 49% in 2007 for freezers. As an effect of the incentive policy, the percentage of sales of A+ refrigerator increased by a factor of 2.64 and , the percentage of sales of A+ freezer grew by a factor of 1.44.

1.3 Technological evolution in household refrigerators

The refrigerator field has been a very innovative sector during its technological development. To understand how a refrigerator is made today, we must trace back a short story of the evolution of the household refrigeration technology. Knowing the advantages and the disadvantages of the previous refrigerator

technologies, we can understand and appreciate which are the state of the art and the future perspectives of this sector nowadays.

1.3.1 Traditional household refrigerators

The conventional refrigeration cycle of household refrigerator is represented in Fig. 1.4.

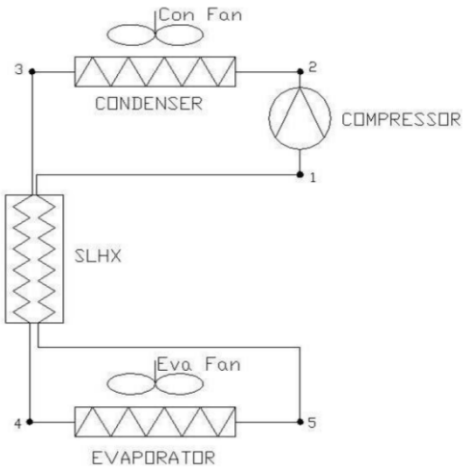

Figure 1.4 Diagram of a traditional refrigeration cycle [2].

As we can see in the picture, it is composed by a fixed speed compressor, an evaporator , a condenser and a Suction Line Heat eXchanger (SLHX) that includes also the capillary. The SLHX has a double role: on the one hand the refrigerant that exits the evaporator is superheated in order to protect the compressor, on the other hand the liquid that exits the condenser is subcooled in order to reduce the losses of the expansion process. Moreover, since the appliance should provide two different temperatures for the two different compartments (refrigerator and freezer), dampers are installed near the evaporator. When the freezer needs to be cooled the compressor starts running and the required cooling capacity is provided activating a fan that blows fresh air through the evaporator to the Freezer Compartment (FC). The refrigerator temperature is controlled by dampers that allow a precise amount of cold air blown by the fan to be directed to the refrigerator compartment. The control system detects the temperature in the refrigerator compartment and decides the right amount of air that dampers should pass to bring the refrigerator temperature to the set point temperature. There are three main negative points about this technology.

In primis, the refrigerator and the freezer temperatures cannot be controlled individually. In this systems the refrigerator temperature depends on the freezer

temperature that could activate the compressor. So, for example, we can have a situation where we do not manage to cool the refrigerator even if cooling would be required.
Another negative point of this conventional technology is that we cannot control the humidity. Humidity level plays a crucial role for food conservation. With this technology we only limit the humidity because the water of the air blown by the fan freezes on the cold evaporator surface before entering the compartment. Anyway we do not manage to have a strict control on the humidity level that could help us in preserving fresh foods.
The last negative aspect of the traditional cold appliances is that they cannot have different evaporation temperatures for the refrigerator and for the freezer. In particular our cycle works only with the freezer evaporation temperature. This fact means that our cycle cannot have the benefit on energy savings related to the use of higher evaporation temperature to control the refrigerator temperature.

1.3.2 Two evaporation temperatures in household refrigerators

In order to solve the third problem related to the conventional refrigerators, engineers developed refrigeration cycles that allow to have two different evaporation temperatures for refrigerator and freezer compartments. The two evaporation temperature technology can be divided in two categories: single evaporator and double evaporator.
In 1998 Park [3] presented the so called Single Evaporation Dual Source (SEDS) cycle. In Fig. 1.5 we display a schematization of the thermodynamic cycle.

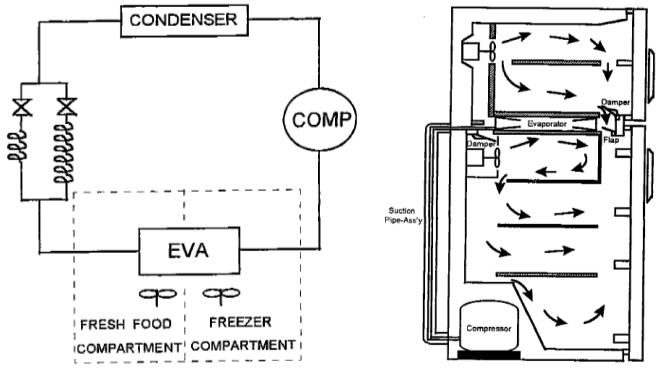

Figure 1.5 Diagram of the SEDS cycle [2].

In this cycle on the one hand we still have one fixed speed compressor, one evaporator and one condenser, on the other hand we have a double system of fans and dampers, two independent solenoid valves and two independent capillary tubes.
As we can see in Fig. 1.5 the airs in the two compartments never mix. Moreover using the valve and the capillary system we are also able to have different evaporation temperatures during refrigerator and freezer operation. When a compartment needs to be cooled the corresponding solenoid valve is activated and the refrigerant passes through the consequent capillary tube. The relative fan and damper are also activated in order to blow cold air only in the chosen compartment. This refrigeration technology showed the expected good results in terms of energy consumption. The measured consumption of the cold appliance diminished of 5.2 % of the total energy.
The simplest technology to implement a double evaporator cycle is to have two separate refrigeration cycles: one for the refrigerator and one for the freezer. This technology was called dual loop refrigeration circuit. In Fig. 1.6 we show a schematization of the thermodynamic cycle.

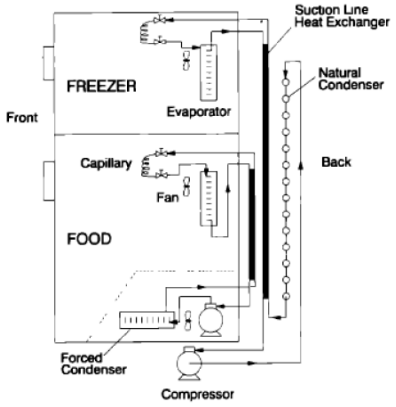

Figure 1.6 Example of a dual loop refrigeration system [2].

It consists in having two separate optimized cycles for the two compartments. From the theoretical point of view this solution could bring to the biggest reduction in energy consumption. Every cycle could be studied separately to minimize the energy required by compressors. In reality dual loop cycles face the penalty of using smaller compressor with lower isentropic efficiencies.
Obviously this technology should also deal with the problems related to cost and space issues. On the one hand dual loop systems do not show a decrease of the energy consumption, on the other hand they need more space and money to be built. These are the main reasons because the study of this technology has been partially abandoned.

In the last years different single cycles with two evaporators have been proposed. The difference among the available different technologies mostly relies in the typology of connection of the two evaporators. So we can divide the existing two evaporator cycles in two different categories: two series evaporator cycles and two parallel evaporator cycles.
Lorenz and Meutzner [4] invented a two series evaporator cycle with two internal heat exchangers. In Fig. 1.7 we can see the structure of the cycle.

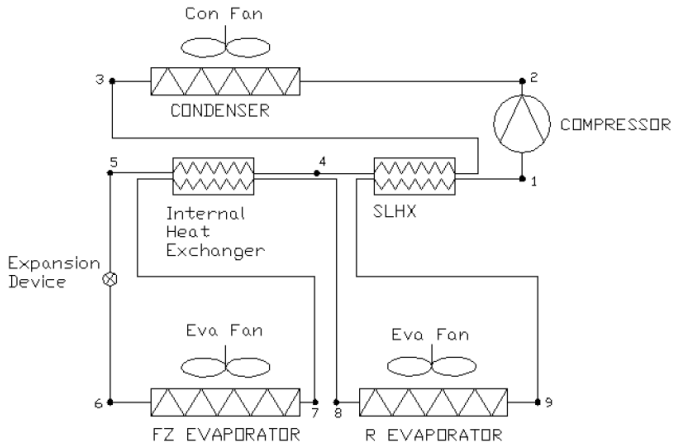

Figure 1.7 Lorenz and Meutzner two series evaporator cycle [2].

We can see that this cycle is composed by a freezer evaporator (i.e. FZ evaporator) and a refrigerator evaporator (i.e. R evaporator) that are placed in series. Moreover both the SLHX and the internal heat exchanger help to reduce the losses related to the expansion process sub-cooling the liquid that exits the condenser. In fact the authors reported that their cycle using a mixture of R22/R11 showed 20% energy reduction compared to a traditional cycle with R12. The zeotropic mixture was chosen to match the required evaporation temperatures. The main disadvantage of this cycle was that the refrigerators and the freezer temperatures could not be controlled separately. Other scientists [5] tried to solve this issue adding bypass loops to the Lorenz and Meutzner cycle, but they did not obtain good results. The use of bypass loops always brought to large decrease of the efficiency of the cycles versus the initial cycle of Lorenz and Meutzner. For example Simmons succeeded in creating an independent control of the refrigerator and the freezer temperature, but his cycle had a penalty of around 10% in energy saving compared to the initial cycle.

The most successful two parallel evaporator cycle was invented and patented by Radermacher [6] in 1998. In Fig. 1.8 we show a schematization of the thermodynamic cycle.

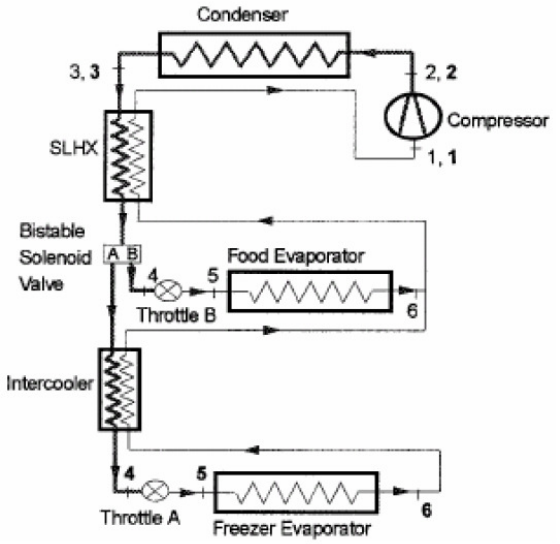

Figure 1.8 Alternative evaporator duty cycle [2].

This technology was called Alternative Evaporator Duty cycle (AED) and it showed very good energy saving characteristics. Radermacher et al. proved that AED cycle shows a 9% less energy consumption versus a traditional two series evaporator cycle. The system cools alternatively the refrigerator or the freezer compartments switching the position of the bistable solenoid valve and activating only one evaporator at the time. During the refrigerator operation we will have a high evaporation temperature that will positively affect the Coefficient Of Performance (COP). So the averaged COP of the refrigerator will be higher than traditional two series evaporator cycle. This cycle managed also to overcome the disadvantages of the dual loop technology. In fact in this case on the one hand we use only one medium-size compressor with good values of isentropic efficiency, on the other hand we save space and money because we have few components than in a dual loop cycle.

1.4 Conclusions

Based on the energy consumption data of the actual appliances, we chose to focus this thesis on the development of innovative cold appliance based on two parallel evaporator cycles technology. In particular we decided to study the Sequential Dual Evaporator (SDE) circuits because they showed to have the strongest potential to improve energy efficiency characteristics of both freezer and refrigerator. In Fig. 1.9 we show a schematization of the thermodynamic cycle of the considered refrigeration technology.

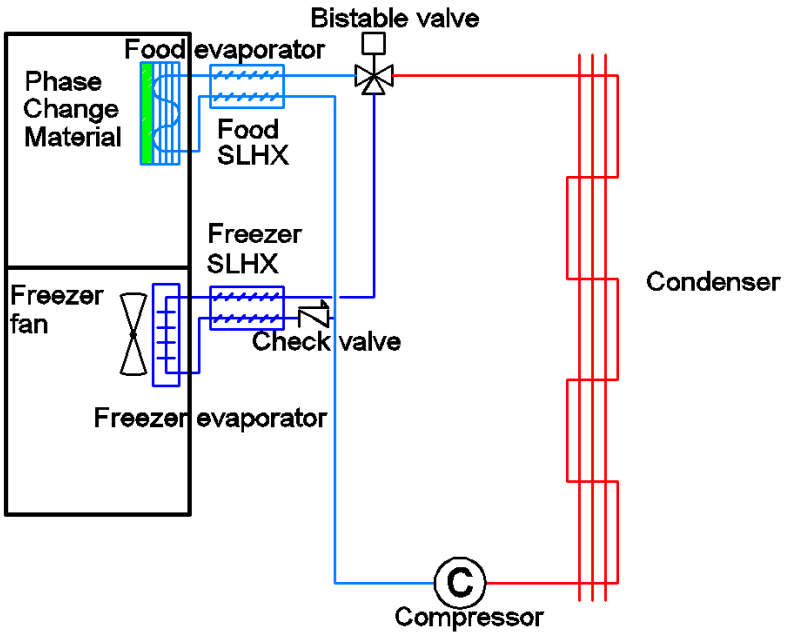

Figure 1.9 Main components of the SDE cycle.

As we can see both the suction line heat exchangers with the included capillaries are positioned after the bistable valve, so that we can adjust independently the pressure conditions in every evaporator. Moreover the cycle contains a check valve to reduce the charge migration phenomenon during the off periods of the compressor. In chapter 2 we will describe deeply every component of this cycle. In the thesis we create models of the involved components and we also optimize some peculiar characteristics of the cycle through experimental campaigns.

2. Experimental apparatus

2.1 General characteristics

The prototype is a bottom-mount refrigerator-freezer built-in appliance. It is equipped with a variable speed compressor and a visible roll-bond evaporator in refrigerator compartment (RC). The device consists of two compartments: one on the bottom where the freezer is positioned and one on the top where the refrigerator is placed. We have two different air operating temperatures for the two compartments: –18°C for the freezer and 5 °C for the refrigerator.
The insulation of the compartments from the external ambient is made both with polyurethane foam panels and vacuum panels. In particular our appliance has the vacuum panels in the lateral walls and in the doors.
The adoption of the vacuum thermal panels allows a sharp decrease of the thermal load of both the refrigerator and the freezer. In fact normally the vacuum panel has a high porous inner part usually made by fiber glass or silica with a very low thermal conductivity. This inner section is sealed in an envelope prepared with a thin aluminum foil. The vacuum insulation panel usually reaches values of thermal resistance much lower than the standard polyurethane foams. Normally the thermal conductivity of these panels lies betwenn $1.4 * 10^{-3}$ W/mK and $5 * 10^{-3}$ W/mK, while the normal range of the thermal conductivity of the polyurethane foams is from 10 to 5 times higher. Anyway these panels have also two main disadvantages related to the aging and the cost. During the time these panels decrease their thermal resistance because of air infiltration. Moreover they have also a high initial manufacturing cost. In Tab. 2.1 we show the main geometrical characteristics of the VIPs installed on the considered appliance.

Table 2.1 Relevant characteristics of the VIPS installed on the appliance.

Conductivity [W/mK]	*Position*	*Size [cm]*	*Pieces*
From $1.4 * 10^{-3}$ to $5 * 10^{-3}$ W/mK	Side walls	45x125	2x
	RC door	30x40	2x
	FC door	30x40	1x

In Fig. 2.1 we show the roll-bond evaporator in the refrigerator cabinet.

Figure 2.1 Foamed-in evaporator in the RC.

The foamed-in roll-bond evaporator is placed into the back wall of the refrigeration compartment in the way that only one side of the evaporator manages to exchange heat with the air inside the cabinet through the foaming. The refrigeration compartment has also a fan that is not used to increase the heat transfer, but it is useful for food preservation. The purpose of this fan is to move the air inside the cabinet to have a uniform humidity in order to preserve the quality of the food along the time. So the back wall of the refrigeration compartment should be designed to maximize the natural convection heat transfer coefficient. By now, since there are some issues regarding the acceptability of a different designs of the back wall by customers, the back wall is the standard one with the foamed-in roll bond evaporator and flat surfaces around it.

Roll-bond evaporator is connected to the suction of the compressor through counter flow capillary tube 1.5 m long completely foamed in the cabinet's back wall. The RC capillary tube has a inner diameter of 0.6 mm and a total length of 2.28 m. The capillary tube is designed according to the relative standard. In particular our capillary tube allows 4.9 l/min volume flow of the N_2 in the standard conditions.

The FC has an evaporator of the fins and tubes type. In particular it consists of 50 Al fins and a Al tube of 5.5 m placed in 2 rows with 9 tubes per row. The freezer evaporator has a device that prevents itself from freezing (i.e. it is a, so called, "no frost" evaporator) and it has also a fan on the back to increase the

heat transfer through forced convection. The no frost technology consists of a small heater installed on the evaporator external surface that heats the evaporator for a short period of time and melts the ice that has probably formed on it. The defrosting process is controlled by an electronic timer that starts the defrost procedure with a scheduled timing during the refrigerator operation. Moreover the FC capillary tube has a inner diameter of 0.8 mm it is designed according to the relative standard to allow 8 l/min volume flow of the N_2 in the standard conditions.
Condenser is the typical one made of a steel tube covered by steel plate with fins cut and bended placed in the back of the appliance. It covers all the rear cabinet wall area. In Tab. 2.2 we sum up the main characteristics of the evaporators, the condenser and the suction line heat exchangers.

Table 2.2 Main characteristics of the evaporators, the condensers and the suction line heat exchangers

Component	*Peculiar characteristics*	*Geometrical features*
RC capillary tube	It allows 4.9 l/min volume flow of N_2 from the pressure 10 bar to the ambient pressure.	0.6 mm inner diameter and overall length 2.28 m
RC suction line heat exchanger	RC SLHX consists of counter flow capillary in suction tube heat exchanger.	Contact length: 1.4 m.
RC evaporator	Foamed-in roll-bond evaporator.	External area: 0.456 m^2 Internal area: 0.211 m^2 Evaporator height: 0.535 m Channel inner diameter: 0.0055 m Channel outer diameter: 0.0085 m Channel length: 6.12 m
FC capillary tube	It allows 8 l/min volume flow of N_2 from the pressure 10 bar to the ambient pressure.	0.8 mm inner diameter.
FC suction line heat exchanger	FC SLHX consists of counter flow capillary in suction tube heat exchanger	Contact length: 1.5 m.
FC evaporator	"No frost" evaporator.	Channel length: 5.5m (2 rows and 9 tubes per row). 50 Aluminum fins.

Moreover the appliance is equipped with the VEMC9C variable speed compressor made by Embraco. The revolution speed could be set through an external frequency regulator in the range between 1200 rpm and 4500 rpm.
Finally the system is charged with 42 g of isobutene. This fluid is a typical choice in the refrigeration field. In fact, even if it is flammable, it shows good parameters regarding the environmental aspects. In particular R600a has a Ozone Depletion Potential (ODP) equal to zero and a Global Warming Potential (GWP) equal to 3.

2.2 Thermodynamic cycle description

In order to deeply understand the test that we will perform on the appliance, we should describe the thermodynamic cycle. In Fig. 2.2 we can see a sketch of the cycle. As we can see from the picture, our refrigeration cycle shows some peculiar characteristics that differentiate it from a classical sequential dual evaporator cycle.
On the one hand we have the classical suction line heat exchangers both on the refrigerator (RC-SLHX) and the freezer line (FC-SLHX). We also have an electro valve that decides which compartment should be cooled (EV). On the other hand we have a check valve (CV) that could be bypassed using a manual valve (MV1) through a different line on the end of the freezer line. Thanks to the bypass line we can try to assess the impact of the check valve on the energy consumption.

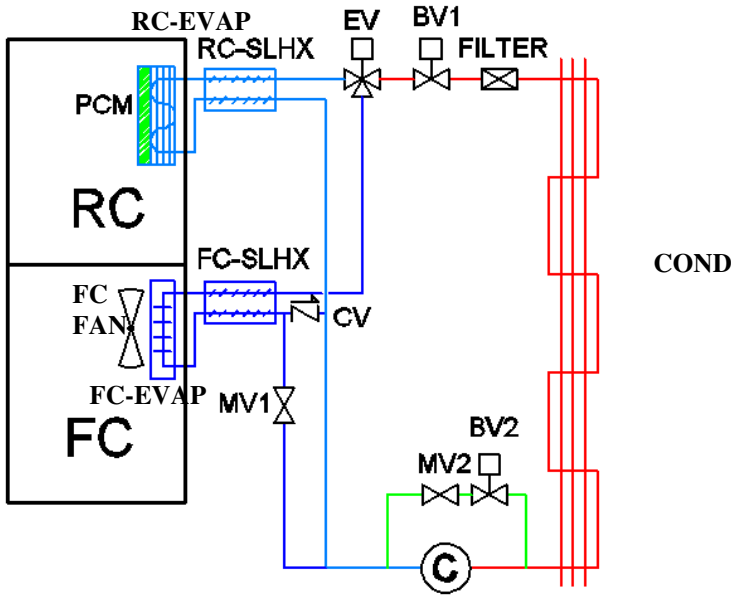

Figure 2.2 Sketch of the thermodynamic cycle of the appliance.

We also have a block valve (BV1) on the output line of the condenser (COND) that is useful to perform the so called "pump out procedure". This procedure is very important to promote the cooling effectiveness of both the compartments. In the sequential dual evaporator cycle we have a problem related to the charge migration. When we switch from the freezer to the refrigerator cooling, the refrigerant migrates according to the pressure difference between freezer and refrigerator evaporators (FC-EVAP and RC-EVAP). Since we have lower temperatures in the freezer than in the refrigerator a big amount of charge will be trapped in the freezer. So we need to perform the pump out procedure before switching to the cooling of the refrigerator compartment. The pump out is made by running the compressor with a closed valve in the output line of the condenser. Usually the pump out is performed till the power of the compressor becomes so low that means that the compressor is no more pumping out refrigerant from the freezer.
In our cycle we also have a bypass line for the compressor starting. In the starting conditions we will have a big pressure drop on the sides of the compressor that could prevent it from switching on. So, if necessary, we can open the valves (MV2 and BV2) of the bypass line equalizing the pressure before the compressor start.

2.3 Sensors

The appliance is equipped with 26 T-type thermocouples with an accuracy of ± 0.5 °C. Four thermocouples are directly positioned in the Phase Change Material (PCM). Table 2.3 summarizes the positions where the thermocouples are placed.

Table 2.3 Names and positions of the 26 thermocouples.

	Condenser	
1	TcMID	Middle of the condenser
2	TcOUT	Outlet of the condenser
3	Tfilter	Surface of the filter
	RC Evaporator	
4	TeRC_IN	Entrance of the evaporator
5	TeRC_M	Middle of the evaporator
6	TeRC_OUT	Exit of the evaporator
7	TeBWB	Bottom of the back wall
8	TeBWT	Top of the back wall
9	Tpcm2	10 cm from the top left of the PCM inside the plastic bag
10	Tpcm4	30 cm from the top left of the PCM inside the plastic bag
11	Tpcm3	10 cm from the top right of the PCM inside the plastic bag
12	Tpcm1	30 cm from the top right of the PCM inside the plastic bag
	FC evaporator	
13	TeFC_IN	Entrance of the evaporator
14	TeFC_MID	Middle of the evaporator

15	TeFC_OUT	Exit of the evaporator
	RC Cabinet	
16	TrcT	Hanged in the upper part of the cabinet
17	TrcM	Hanged in the middle part of the cabinet
18	TrcB	Hanged in the lower part of the cabinet
	FC Cabinet	
19	TfcT	Hanged in the upper part of the cabinet
20	TfcM	Hanged in the middle part of the cabinet
21	TfcB	Hanged in the lower part of the cabinet
22	TfcF	Outside the evaporator inlet to start the defrosting procedure
	Others	
23	T1	Compressor Suction Tube
24	Tdisch	Compressor Outlet Tube
25	Tshell	Compressor Shell
26	Tamb	Ambient Temperature

In particular both the refrigerator and the freezer compartments are equipped with 3 thermocouples to measure the internal air temperature according to the ISO 15502 standard (ISO, 2005). So in both the compartments there are 3 T-type thermocouples inserted in the middle of a cylinder made of brass with a mass equal to 25g and a diameter and height equal to 15mm. Using the approach of the ISO 15502 we are able to measure the temperature gradient in both the compartments.
Moreover, as we can see in Fig. 2.3, some thermocouples were directly used to determine the thermodynamic conditions of the cycle. All these thermocouples were fastened to the external side of the tubes considering the thermal resistance of the tube negligible for our purposes. Since the filter is placed just few centimeters from the outlet of the condenser, we assume that the temperature of the fluid in the filter is equal to the temperature at the outlet of the condenser.

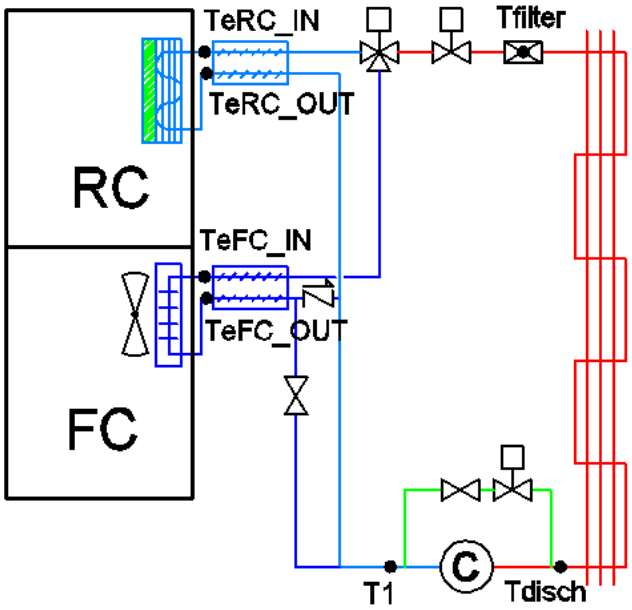

Figure 2.3 Sketch of the positions of the thermocouples used to determine thermodynamic cycle.

The appliance is also equipped with two pressure transducers to measure the two levels of pressure of the thermodynamic cycle. In particular these pressure transducers are made by Gems-sensors and they have an operating range from 0.5 to 10 bar with an accuracy equal to 0.15% of the full scale. The two pressure transducers are soldered at the inlet and at the outlet of the compressor. These instruments were manually calibrated on a dedicated device before the installation on our appliance. In Fig.2.4 we can see the calibration curve for one of our pressure transducers.

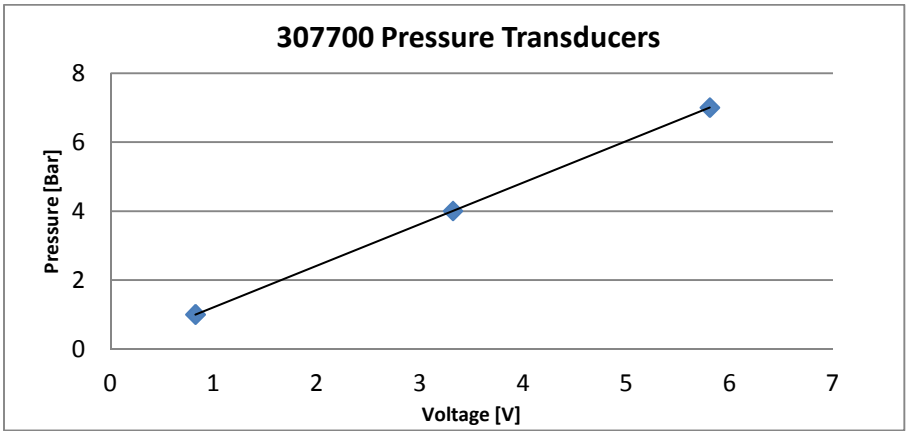

Figure 2.4 Calibration curve for the 307700 pressure transducer.

As we can see from Fig. 2.4 the pressure transducers show a linear trend between the voltage and the pressure. So to calibrate them we should specify the slope and the offset of the straight line. In Tab. 2.4 we show these parameters for our pressure transducers.

Table 2.4 Calibration parameters for the pressure transducers.

Low pressure (serial 307700)		High pressure (serial 307708)	
Slope	1,204	Slope	1,20363
Offset	0,01238	Offset	0,0283

The pressure transducer needs a particular shielded cable to be connected to the control box.
Moreover two thermistors of the Negative Temperature Coefficient type with an accuracy of ± 0.5 °C are installed on the appliance. These devices are useful to determine very quickly the temperature variations in the cabinets. They are protected with little plastic structures to prevent them from impacts.

2.4 Acquisition hardware

We used three different National Instruments boards to acquire the signal of the sensors.
We adopt National Instruments (NI) 9205 to acquire the voltage signals of the two pressure transducers and the compressor frequency. The board has 16 channels for input analogue signals. It reads voltage signals in the range ± 10V. This range fits perfectly the voltage signal coming from the pressure transducers. In fact the voltage for the calibrated devices varies from 0.3 V (i.e. 0.5 bar) to 9 V (i.e. 10 bar). Moreover we also acquire the Negative Temperature Coefficient (NTC) thermistors with the same board. Fig.2.5 shows the electrical circuit that we made to acquire the voltage signals coming from these sensors.

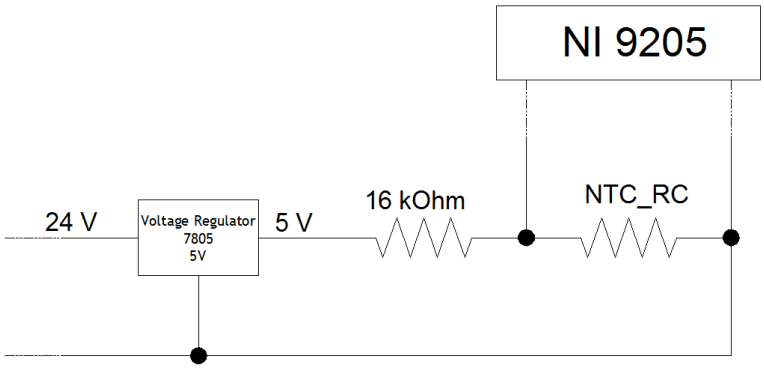

Figure 2.5 Sketch of the acquiring system related to the NTC thermistors.

Every component of the circuit was chosen according to two main purposes. First we want to acquire the signal having an accuracy of at least 1 °C. Secondly we want to limit the current that can flow through the NTC thermistor in order to prevent it from overheating during the time. In particular the current must not be higher than 20 mA. In order to determine all the necessary components of the circuit, at the beginning we write the following equation.

$$\frac{1}{T} = A + B * \ln(R_{NTC}) + C * ln^3(R_{NTC}) \quad (2.1)$$

The equation (2.1) is known as the Steinhart-Hart's equation. This formula approximates the link between the temperature and the resistance of every NTC thermistor. In particular our thermistors have the coefficients shown in Tab. 2.5.

Table 2.5 The Steinhart-Hart's coefficients for our thermistors.

A	0,0014072515
B	0,000241263
C	0,00000008506116466

Normally the NTC thermistors are acquired measuring the voltage drop on the thermistor, knowing the reference voltage and the resistance of the acquiring circuit. In order to fulfill both our purposes we installed a voltage regulator of the 7805 type to have a reference voltage equal to 5 V. Fig 2.6 shows the trend of the measured voltage by the NI9205 versus the measured temperature of the NTC thermistor.

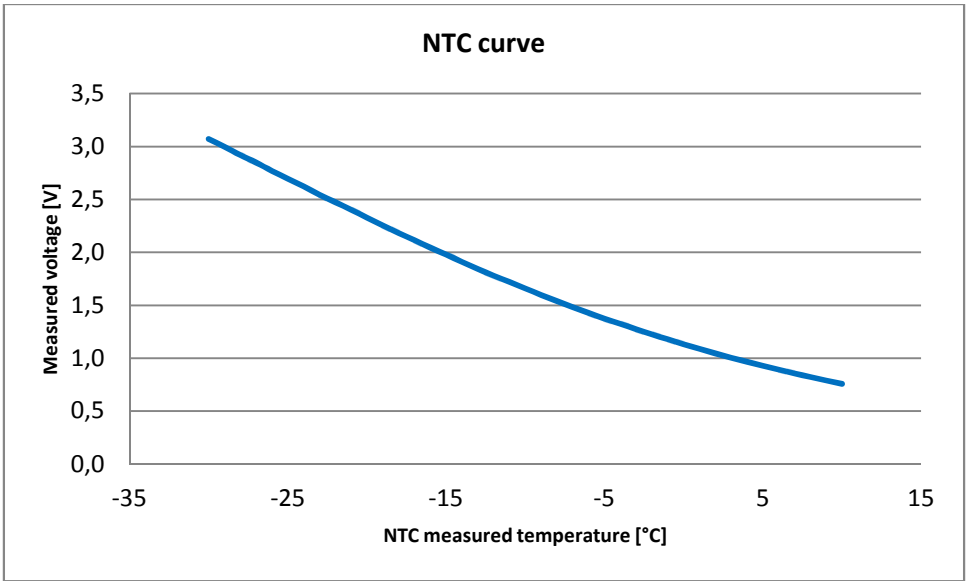

Figure 2.6 Voltage drop on the NTC thermistor related to the measured temperature.

As we can see in Fig.2.6 the voltage follows an almost linear behavior according to Steinhart-Hart's equation. Moreover we can see that in the range of temperatures that we want to measure the voltage remains in the range ±10V that the NI 9205 can acquire.
All the channels of the board share a common ground that is perfectly isolated from the other parts of the board.
The thermocouples are acquired with the NI 9213 board. Since this board has only 16 channels, we are able to acquire at the same time only 16 thermocouples out of the 26 installed on the appliance.
Finally we also measure the compressor power acquiring a current signal with the NI 9203 board. The board has 8 channels for analogue input signals. We use only one channel for the current signal related to the power meter. This signal comes from a power meter carefully selected for this application. The DPT221-401 power meter from CEWE was finally chosen. It has a high accuracy (0.2 class). The instrument has 10 pulses/kW. We configure the power transducer to acquire an expected range of power from 30 W to 300 W through the software ConfigView. Moreover we also program the output signal to be in the range ±20mA in order to match the NI 9203 input's range.

2.5 Control hardware

In order to control our appliance we create a board to send signals to the electro valve, to the block valves, to the refrigerator fan, to the freezer fan and to the compressor.

All the valves, except from the block valve on the bypass line of the compressor, are bi-stable valves. So once we switch the valve from one position to another, it will always remain in the last position till it receives a new signal. On the contrary the valve on the bypass line of the compressor is a solenoid valve (normally closed). When we supply the coil inside of the valve, the shutter opens till the valve is powered. Once we switch off the power, the valve closes. As shown in Fig. 2.7, the bi-stable valves needs 4 half waves to switch from one position to another.

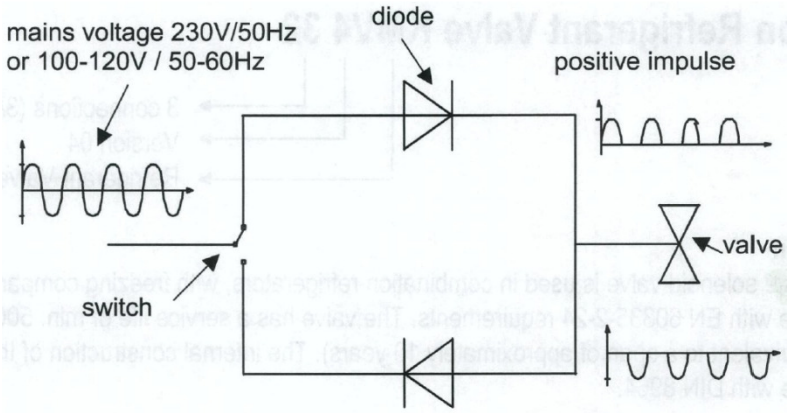

Figure 2.7 Conceptual scheme of the control of a bi-stable valve.

In order to cut the voltage wave, we create a small electronic circuit with two diodes on each way. The bi-stable valve is controlled by the NI9205 through two different relays. On the board side of the relay we also put a Zener diode to limit the peak of voltage when the switch opens and so to prevent the board from serious damages. So for every bi-stable valve we built the electronic circuit shown in Fig 2.8.

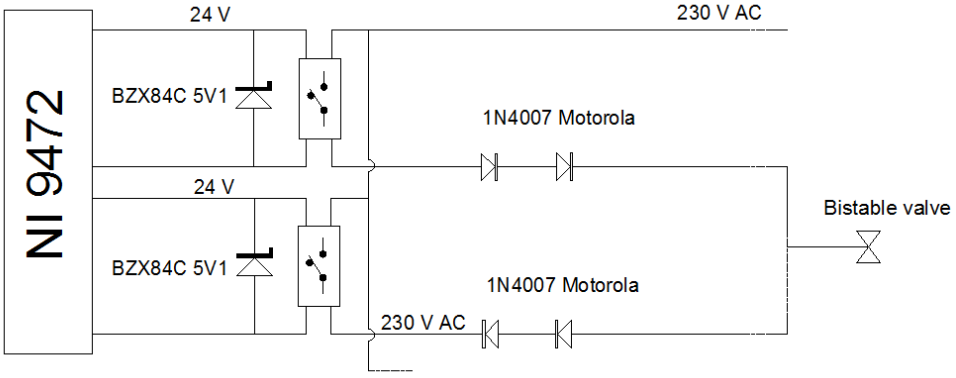

Figure 2.8 Electronic circuit utilized to control a bi-stable valve.

As we can see from Fig.2.8 we use the NI 9472 board for the control part. This board has eight 24 V digital outputs. All the channels of the board share a common ground that is perfectly insulated from the other parts of the board.
The block valve on the bypass line of the compressor is controlled by the board through a relay that allows us to supply the valve only when it is requested. Fig. 2.9 shows the electronic circuit for the control of the valve.

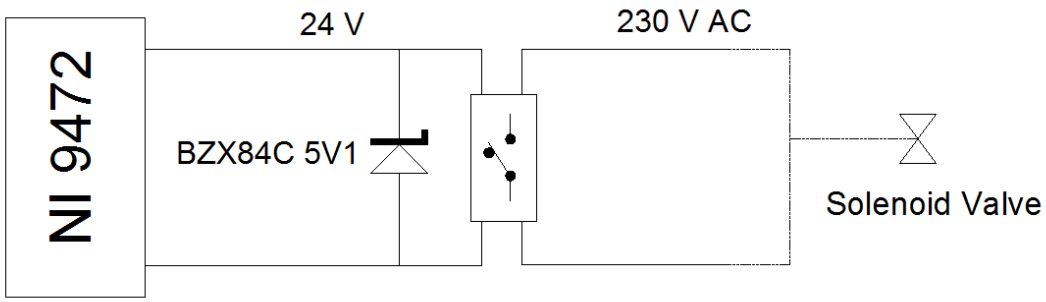

Figure 2.9 Electronic circuit utilized to control a solenoid valve.

The electronic circuit shown in Fig. 2.9 is also used to control both the refrigerator and the freezer fan. The only difference is that the freezer fan should be supplied with 24 V.
The variable speed compressor is equipped with an inverter. It controls and protects the compressor. We controlled the system sending a square signal of 5 V amplitude at different frequencies. We observe a linear trend between the frequency of the square signal and the revolution speed of the compressor. So we developed the electronic circuit shown in Fig 2.10.

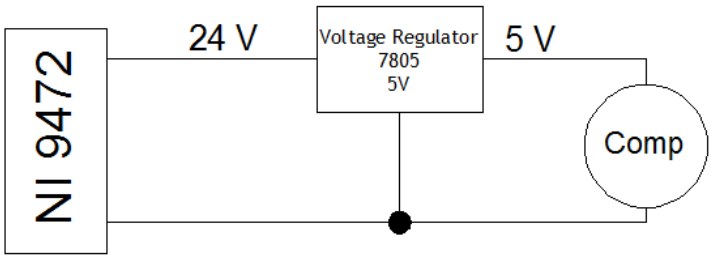

Figure 2.10 Electronic circuit utilized to control the revolution speed of the compressor.

At the beginning we try to control the compressor using a Zener diode of the BZX84C 5V1 type without using a voltage regulator. With this first configuration we did not manage to run the compressor because the signal sent to the compressor by the board changes its square shape interacting with the diode. We discovered this fact measuring the shape of the wave sent to the

compressor before and after the Zener diode with an oscilloscope. So at the end, we decided to implement the circuit with a voltage regulator that does not influence the shape of the signal.
So finally we put all these electronic circuits on one board that was positioned with the power meter and a 24 V power supply in one single plastic box. The results of all these efforts are shown in Fig. 2.11.

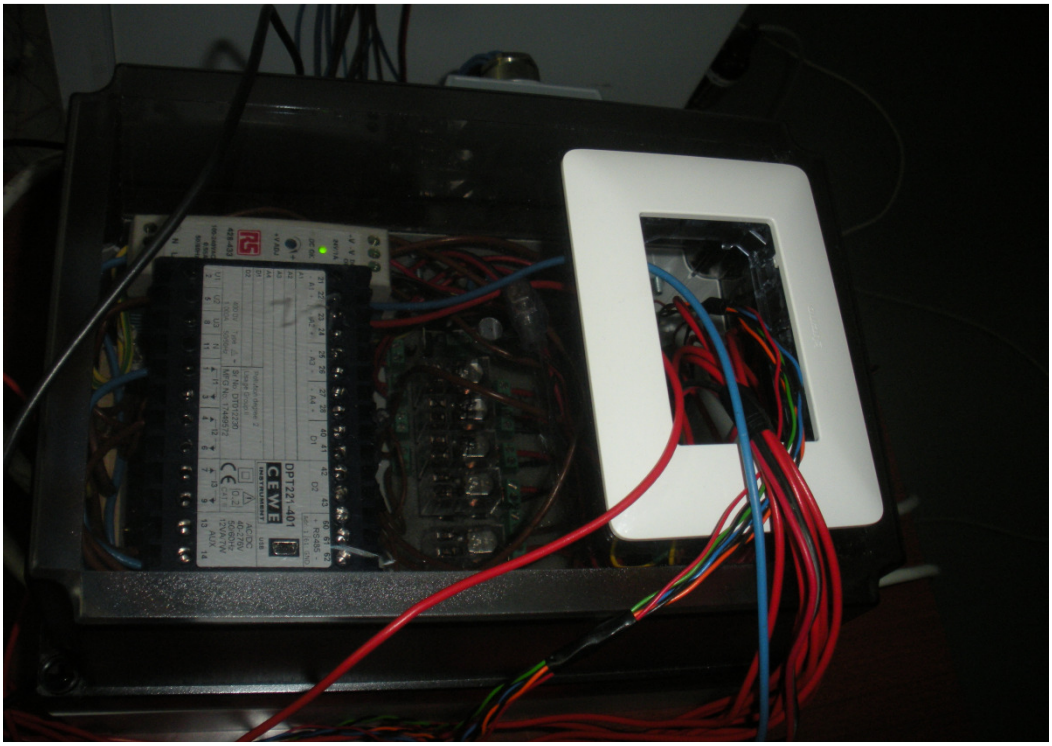

Figure 2.11 Final setup of the control box.

2.6 Control and acquisition software

In order to acquire the experimental measures we use an available LabView program. In particular we modify the part of the program related to the NTC thermistor acquisition according to our experimental setup. As we can induce from Fig. 2.5 we can write the following equation on the circuit of the NTC thermistor.

$$V_{REF} = R_1 * I + V_{NTC} \quad (2.2)$$

Equation (2.2) relates the reference voltage V_{REF} with the voltage drop on the NTC thermistor. Since the voltage regulator imposes a reference voltage equal to 5 V and we know that R_1 is equal to 16 kΩ, we can compute the resistance of

the NTC thermistors. First we calculate the current in the circuit using the following formula.

$$I = \frac{V_{REF}}{R_{NTC} + R_1} \quad (2.3)$$

So we can substitute equation (2.3) in equation (2.2) and we obtain the following equation to compute the resistance of the NTC thermistors (R_{NTC}).

$$R_{NTC} = \frac{R_1 * V_{NTC}}{V_{REF} - V_{NTC}} \quad (2.4)$$

Since we measure the voltage drops on the NTC thermistors through the NI 9205, from equation (2.4) we can obtain their resistances and so, using the Steinhart-Hart's equation, we have the measured temperatures. All these equations were included in the software part for the acquisition of the NTC thermistors.

All the program is based on a case structure where we can find all the different cases of acquisition and control that we use. So for example we have a case to acquire the thermistor, another to acquire thermocouples and another for the start-up of the compressor. Using this structure, the program manages to acquire all the measured parameters every five seconds. This short acquisition time allows us to have a very precise history of the variations of the parameters.

3. Optimizing the PCM freezing temperature

3.1 Introduction

In this section we try to optimize the freezing temperature of the Phase Change Material included in a refrigerator prototype. This optimization will yield to reduce the energy consumption of the refrigerator. To achieve this goal we perform an experimental activity taking advantage of previous PCM appliance prototype described in chapter 2. In particular we focus on the energy consumption in the standard conditions of testing expressed by the EN ISO 15502 standard. We will test different freezing temperatures using mixture of water and NaCl. We perform an experimental activity to optimize the phase change phenomenon since a deep theoretical study is already available[7]. The PCM goes through various cycles made of a charging and a discharging process. During the charging process the PCM freezes because the compressor is switched on. Then during the discharging process the PCM slowly releases the heat keeping the compressor switched off. The adoption of the PCM allows us to reduce the on-time of the compressor and so to lower the related energy consumption. In Fig. 3.1 we show the heat transfer model used to describe this phenomenon.

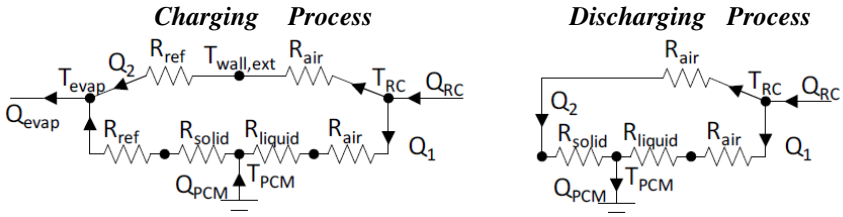

Figure 3.1 Heat transfer model used by M. Visek [7] to describe the PCM behavior.

As we can see in Fig. 3.1 during the charging process the heat of the compartment (Q_{RC}) and the remaining heat of the PCM (Q_{PCM}) are absorbed by the evaporator (Q_{evap}). The model takes into account the refrigerant (R_{ref}) and natural convection-radiation (R_{air}) thermal resistances and two other resistances related to the PCM (R_{solid} and R_{liquid}). The resistances related to the PCM are estimated taking into account the water and the ice properties and the position of the solid-liquid interface. To simplify the problem the author assumes that the thickness of the water and the ice are fixed and both equal to 5 mm. So he decides to neglect the change of thickness of the solid and the liquid phase during the charging and the discharging processes. Using this assumption the author manages to schematize the problem in a stationary way. The author also hypothesizes negligible values for the contact and the plastic bag thermal

resistances. Using this stationary model we are able to understand the benefits related to the adoption of the PCM in the RC cabinet. On the one hand the PCM increases the stability of the cabinet air temperature, on the other hand the adoption of the PCM allows to have a lower heat transfer rate to keep the air temperature within the EN ISO 15502 limits. So a refrigerator equipped with the PCM could use only natural convection in the RC. The saving of the RC fan power is a great opportunity to lower the energy consumption during the standard test. Moreover exchanging heat only through natural convection brings positive effects also on the fresh food preservation.

3.2 Prototype setup

The optimization of the PCM temperature aims at lowering the energy consumption during the standard test conditions. So we went through the EN ISO 15502 to understand the right setup of both the appliance and the thermostatic chamber conditions. According to the standard the ambient should be measured at two points, T_{a1} and T_{a2}, positioned at the horizontal and vertical centreline of the appliance sides. Moreover it is prescribed to locate the measure points at a distance of 350 mm from the refrigerator side. The ambient temperatures should be measured using thermocouples inserted in copper or brass cylinders to avoid instantaneous changes in the temperature reading. These two cylinders should be also shielded from any sources or sinks of radiant heat of the test room. During the energy consumption test T_{a1} and T_{a2} should be always kept equal to the target value of ambient temperature within $\pm$0.5 K. Since we cannot use a real thermostatic chamber to perform the experimental campaign, we manage to stay only in a range $\pm$2.5 K from the target temperature. In fact we just use a room equipped with a simple air conditioner that is normally utilized in the houses. Anyway we always manage to keep the time averaged ambient temperature during the test in a range of $\pm$0.5 K from the target temperature. This accuracy is considered to be acceptable because we perform an optimization based on stationary calculations made on time averaged values during a whole test. So, from our point of view, it is more relevant to keep the time averaged ambient temperature in the standard range than the instantaneous measured ambient temperatures. Moreover the standard prescribes also how to measure the RC storage temperature. This temperature should be acquired using three copper or brass cylinders placed halfway between the rear internal wall of the appliance and the internal wall of the closed door. These three temperature readings should be integrated and averaged using a time step of 60 seconds or less. We decided to acquire the values with a time step of 5 seconds in order to appreciate also the small time variations of the readings. We also measure the temperature of the PCM in four points according to section 2.3. The exact positions of the thermocouples in the RC cabinet are shown in Fig. 3.2.

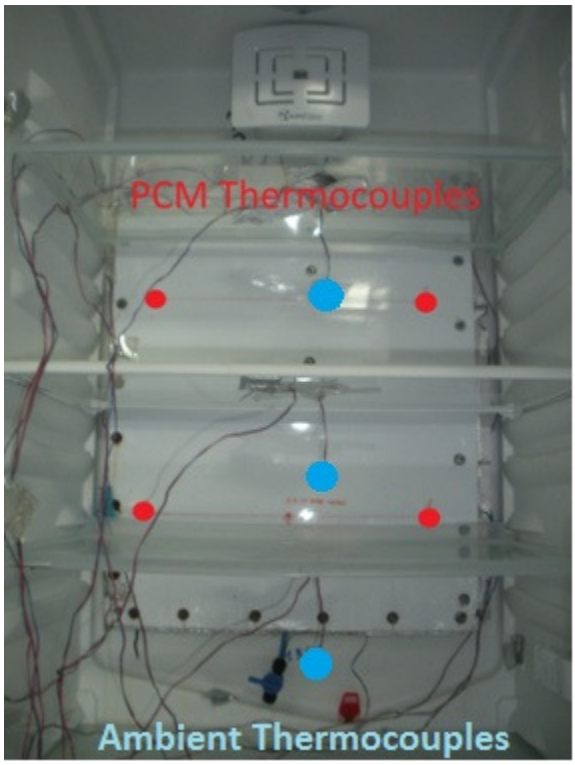

Figure 3.2 Positions of PCM and ambient thermocouples in the RC cabinet.

Moreover the standard prescribes that the watt-hour meter shall be readable to 0.001 kWh with an accuracy within $\pm 1\%$ of the reading. To match these requirements we use the programmable power transducer CEWE DPT221-401 with measurement accuracy 0.2% of reading value.

3.3 Test procedure

At the beginning we set the ambient temperature to 25°C according to the EN ISO 15502 standard. Moreover we programme the Labview acquisition software to match two conditions for the RC storage temperatures given by the EN ISO 15502 standard. During the energy consumption test the standard prescribes that the three measured air temperatures inside the RC should be in the range between 0 - 10°C and that the average air temperature of the RC over the whole testing period (i.e. T_{RC}) has to be less than 5 °C. The first condition is satisfied programming the Labview software to switch on the compressor when the RC highest temperature overcomes an upper bound value (warm point) and to switch off the compressor when the RC lowest temperature is less than a lower bound value (cold point). In order to achieve the second condition, the standard allows performing two tests with two different T_{RC} and then interpolanting the

results to obtain the energy consumption at exactly 5 °C. The difference in T_{RC} between the two tests cannot exceed 4 K. So in order to have comparable results among the tests we perform two tests for every condition and we will interpolate the average consumptions to have the consumption value at 5 °C.
So we run set of tests with steadily cycling refrigeration compartment. In particular we run a set of 6 tests without PCM with steadily cycling RC at three different compressor frequencies: 54 Hz, 75 Hz and 100 Hz. Two tests per frequency (warm and cold point) with following setup of temperature boundaries. Warm point with upper bound set to 9.5 °C and lower bound equal to 2 °C. Cold point with upper bound 8 °C and lower bound equal to 1 °C. We measure the energy consumption at every test and then interpolating the T_{RC} we find energy consumption corresponding to T_{RC} equal to 5 °C. After that, we repeat the same set of 6 tests with water as PCM inside the thermal accumulator pocket selecting different warm and cold points. In particular the warm point with upper bound set to 8 °C and lower bound equal to 1 °C and the cold point with upper bound 6 °C and lower bound equal to 1 °C. To select the best operating frequency we compute the COP according to the equation (3.1) for all the tests.

$$COP = \frac{UA_{polimi}(\overline{T_{amb}} - \overline{T_{RC}})}{Average\ Power\ per\ day} \qquad (3.1)$$

$\overline{T_{amb}}\ and\ \overline{T_{RC}}$ represent the ambient and the RC averaged temperatures that we measured during a test. Every test lasts at least 24 hours. Then we select the frequency that shows the highest COP between all the tests with and without PCM. This criterion allows us to select the optimum frequency to lower the energy consumptions of the refrigerator. Finally using the selected compressor frequency we run some tests with water plus NaCl as PCM to have a different freezing temperatures. First we run two test with PCM temperature equal to -2 °C and air temperature bounds equal to 8/1 °C and 9.5/2 °C. Secondly we also perform two test with PCM temperature equal to -4 °C and air temperature bounds equal to 8/1 °C and 9.5/3 °C. We compute the right quantity of salt to have the required freezing temperature relying on the following equation.

$$NaCl_s \rightarrow Na_w^+ + Cl_w^- \qquad (3.2)$$

This equation states that during the dissociation of the salt in the water the initial mole of NaCl splits in two moles of ions. So we can compute the mass of NaCl (m_{NaCl}) that should be dissolved into a certain amount of water (m_{H2O}) to have the required lowering of the freezing temperature (ΔT_{ft}) according to the following equation.

$$m_{NaCl} = MM_{NaCl} * m_{H2O} * \frac{\Delta T_{ft}}{i * k_{ft}} \qquad (3.3)$$

Since we are considering a dissociation process of a salt into the water we take the index i equal to 2. We also took the value of the cryoscopic constant (k_{ft}) equal to 1.86 °C [8]. The results of this method are shown in Tab. 3.1.

Table 3.1 Required quantities of NaCl that have to be dissolved into the water to obtain different freezing temperatures.

Freezing Temperature	Mass of Water [g]	Mass of NaCl [g]
-2	1750	55
-4	1750	110

3.4 Results

In order to have reliable data we run every test for at least 24 hours till we can observe a stable cycling behavior of the appliance. At the beginning we try to find the right position in the thermostatic chamber of the sensor that measures the ambient temperature. In Fig. 3.3 we show a typical trend of the ambient temperature during the tests.

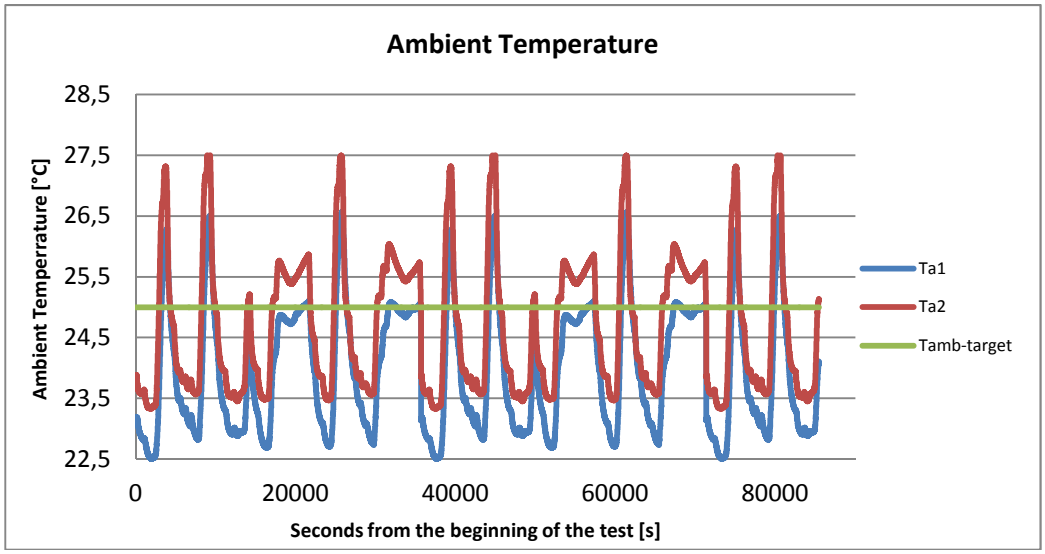

Figure 3.3 Typical trend of the ambient temperatures during the tests.

As we can see in Fig. 3.3 the thermostatic chamber manages only to keep the time average ambient temperature in the range of ±0.5 K from the target temperature, but it does not manage to keep the instantaneous temperatures in the same range. In fact the chamber shows a deadband of ±2.5 K from the target temperature where it is not able to control the temperature. In other words the

measurements show that the system is not enough fast to shift from heating to cooling and the contrary in a short time period that allows the ambient temperature to be in the EN ISO 15502 range.
Moreover we measure the RC air temperatures in order to match the requirements of the energy consumption tests. In Fig. 3.4 we display a typical trend of the RC air temperature.

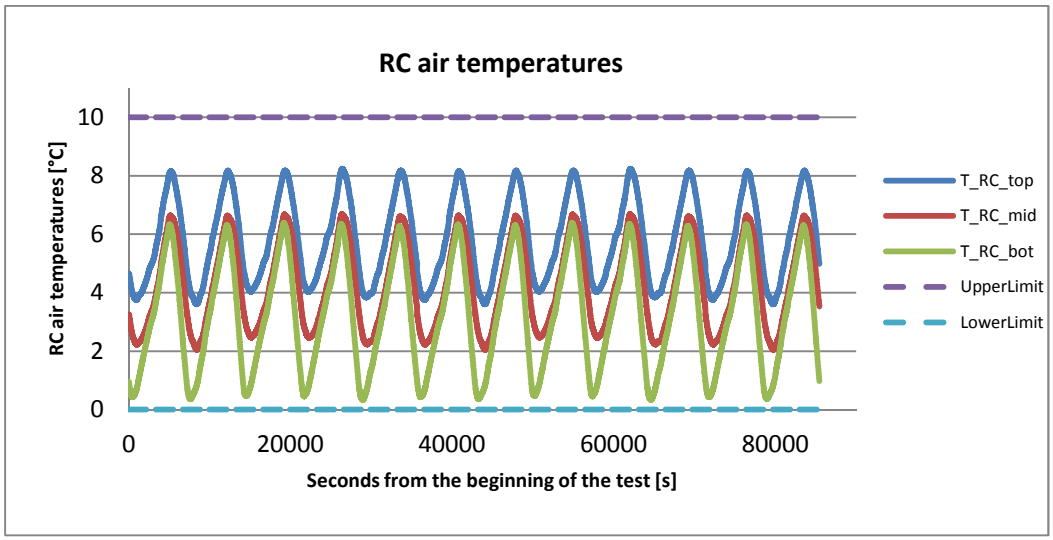

Figure 3.4 Typical trend of RC air temperatures during the tests.

As we can see in Fig. 3.4 the Labview control software manages to keep the RC ambient temperatures in the required range from 0 to 10 °C. In particular we can also notice the typical phenomenon of temperature stratification in the appliance. The stratification should always be monitored to avoid the freezing of the food in the lower part of the RC cabinet. This issue is widely studied every time that a new appliance should be put on the market in order to avoid compliances about food preservation.
Fig. 3.5 shows the typical cycling behavior of the appliance that is recorded for every test without the Phase Change Material.

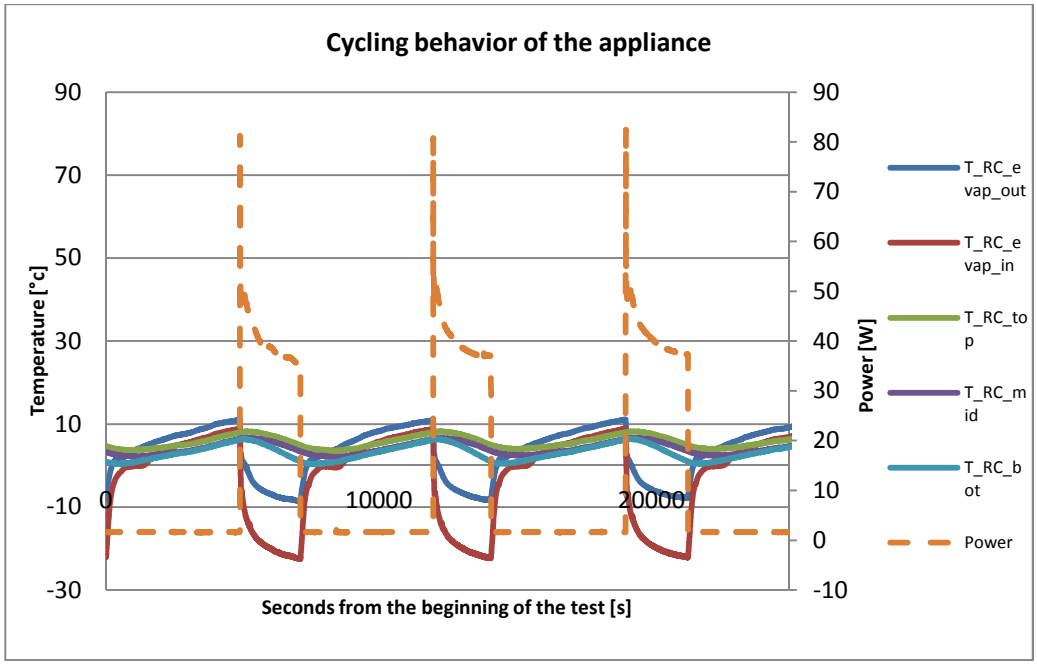

Figure 3.5 Typical cycling behavior of the appliance during the tests.

As we can observe in Fig. 3.5 the single cycle starts when the RC top air temperature overcomes the set upper bound and finishes when the RC bottom air temperature is less than the set lower bound. The compressor requires the highest power in the first seconds of the start-up to win the starting torque and then it slowly needs less power till the switching off. At the same time the evaporator temperatures reduce drastically in the immediate start-up and then they slowly manage to reach the stationary behavior. Anyway during the cycles the appliance does not manage to reach a stationary condition where both the compressor power and evaporator temperatures get stable. So from Fig. 3.5 we can understand the importance of a deep study of the thermodynamic cycle in the refrigerator development in order to move from stationary to dynamic models. The development of dynamic models could be the challenge for the future improvements of this work.

The first step of the tests consists in the identification of the best frequency to run the compressor without the PCM. In Fig. 3.6 we display the typical cycling behavior of the compressor power at the three considered frequencies.

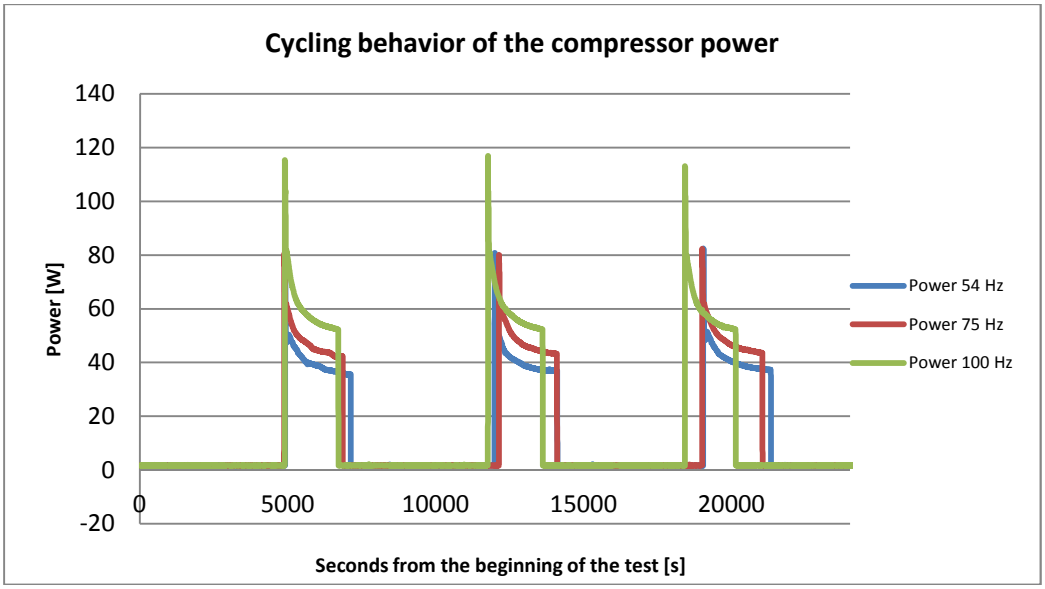

Figure 3.6 Typical cycling behavior of the compressor power varying the frequency.

On the one hand, as we raise the compressor frequency we reduce the compressor on-time, but we also increase the required power during each cycle. In fact if we increase the frequency the compressor will provide more cooling capacity and so it will take less time to cool down the compartment. On the other hand the frequency does not have an impact on the compressor off-time. The compressor off-time represents the time that the cabinet takes to overcome the imposed temperature limits and so it is only related to the insulation of the cabinet and not to the compressor itself.
In Tab. 3.2 we present the measured and computed data for the appliance for the three considered frequencies.

Table 3.2 Calculated and measured data of performance of the appliance at the three considered frequencies without PCM.

Frequency [Hz]	Lower Temperature Limit [°C]	Upper Temperature Limit [°C]	$\overline{T_{RC}}$ [°C]	$\overline{T_{amb}}$ [°C]	Average Consumption [W]	Average Consumption @ T_{ma} = 5 °C [W]	Heat Gain [W]	COP
54	1	8	4.5	24.6	12.3	12.2	23.3	1.90
54	2	9.5	5.7	25.0	12.2			
75	1	8	4.4	24.7	13.5	13.3	23.3	1.76
75	2	9.5	5.7	25.0	13.0			
100	1	8	4.4	25.0	15.6	15.1	23.5	1.55
100	2	9.5	5.6	25.0	14.7			

We measure the compressor consumption in six different tests varying the RC temperature limits. If we increase the integrated time averaged RC air temperature ($\overline{T_{RC}}$) during the test, we will have a lower energy consumption since we will allow larger variations of the RC air. We also interpolate the measured data to obtain the average consumption that the appliance would have

in a test with $\overline{T_{RC}}$ equal to 5 ° C. Finally we compute the COP in this standard condition. As we can see in Tab. 3.2 the compressor without the PCM is designed to work at the lowest frequency.
Moreover we run other six tests with the water as PCM varying the compressor frequency. We expect to see charging and discharging cycles of the PCM that allow the RC air temperature to be more stable than the condition without the PCM. In the cases where we won't observe the PCM cycles we will have higher energy consumptions because the PCM will act only as an additional thermal resistance between the refrigerant and the RC air without lowering the compressor on-time. In Fig. 3.7 we show the typical charge and discharge cycling behavior of the PCM.

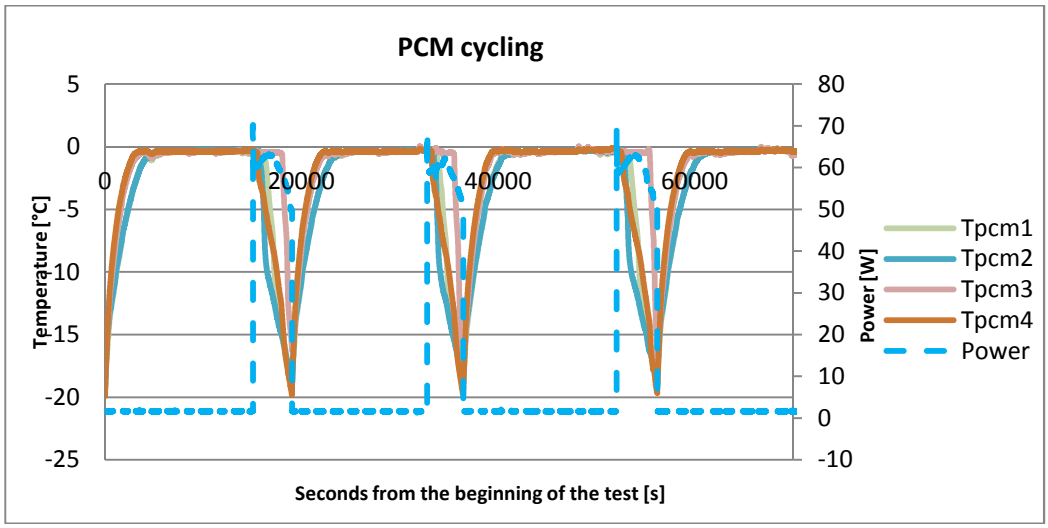

Figure 3.7 Typical charge and discharge process of the PCM.

As we can see in Fig. 3.7 the PCM charges during the compressor on-time and it slowly discharges the heat to the RC during all the compressor off-time. In particular the PCM temperatures start to decrease following the refrigerant flow direction. In fact they decrease from the one nearer the evaporator entrance (T_{pcm2}) to the one nearer the evaporator exit (T_{pcm3}). When the compressor switches off all the PCM temperatures tend to reach the freezing temperature and the RC is cooled by the phase change heat stored in the PCM. Anyway the PCM does not manage to melt completely and so some of the possible benefits are not exploited in this configuration. The best situation would be to see entire cycles of freezing and melting. In fact in this case we will manage to exploit all the storing capacity of the PCM.
As we can induce from Fig. 3.7 the PCM cycling allows the compressor to provide less cooling capacity also during the on-time since the RC cabinet is always cooled by the heat stored in the PCM. In fact we can prove this fact making a comparison between the compressor power shapes in two different

situations where the PCM acts differently. For example, for a fixed frequency, we can compare the compressor power for a test where the PCM actually charges and discharges (RC upper limit equal to 8 °C and RC lower limit equal to 1 °C) and a test where the PCM acts only as an additional thermal resistance (RC upper limit equal to 6 °C and RC lower limit equal to 1 °C). We show this comparison in Fig. 3.8.

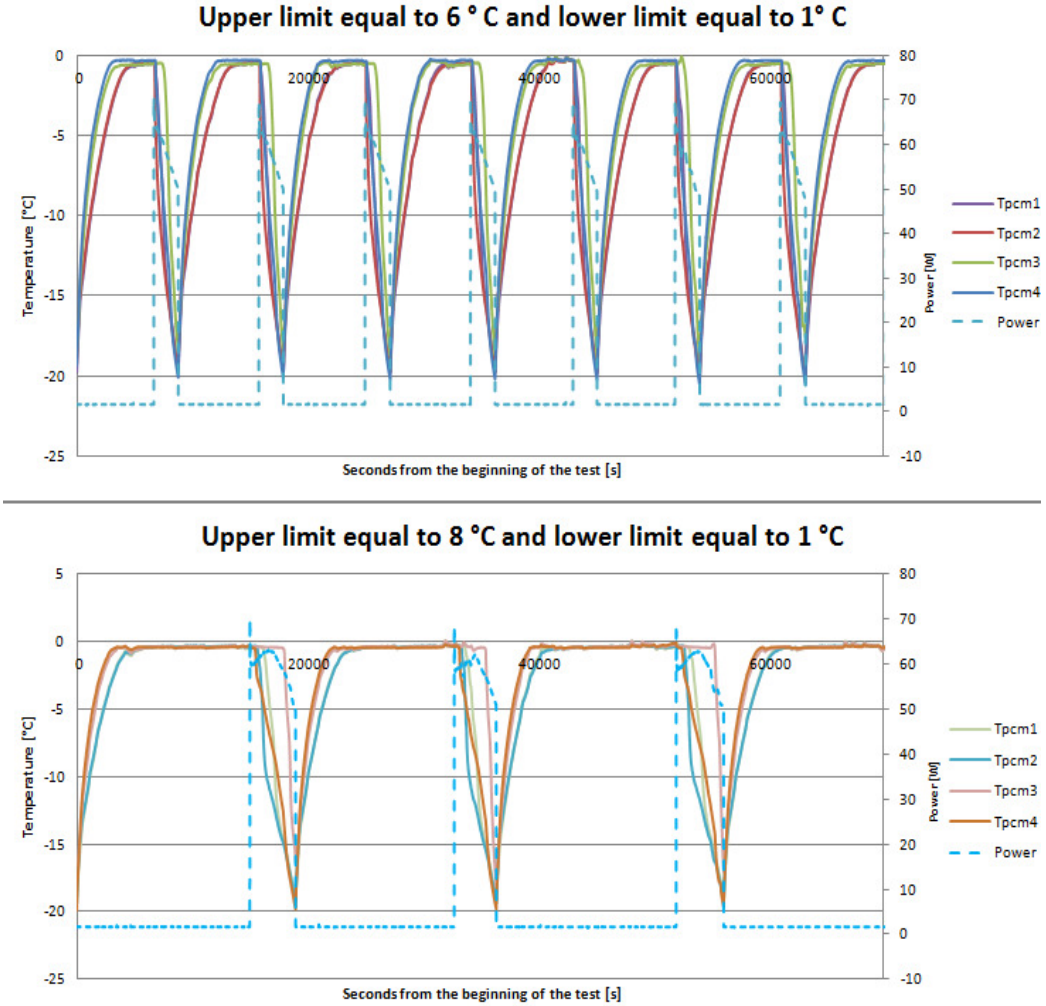

Figure 3.8 Importance of the PCM charge and discharge cycle at 75 Hz.

As we can see in Fig. 3.8 when the PCM charge and discharge process takes place we have a peculiar shape of the power curve that reflects the energy saving related to the utilization of the PCM.
As we already stated the PCM affects also the RC air temperature. In Fig. 3.9 we display the RC average temperature for a fixed condition with and without PCM.

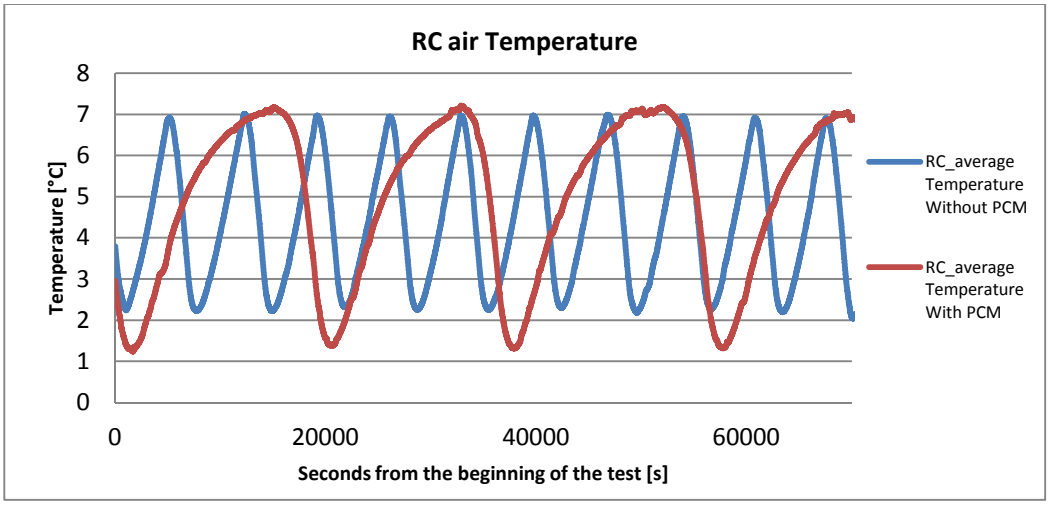

Figure 3.9 Importance of the PCM for the stabilization of the RC air temperature.

As we can see in Fig. 3.9 the PCM lowers the frequency of the oscillations of the RC air temperature during the appliance cycles. In fact while without the PCM we only cool the compartment when the compressor is running, with the PCM we have a continuous cooling of the cabinet thanks to the phase change heat.
We run all the test with water as PCM and we compute the COP in every case to choose the case for the final PCM temperature optimization. The measured and computed data for these tests are shown in Tab. 3.3.

Table 3.3 Calculated and measured data of performance of the appliance at the three considered frequencies with water as PCM.

Frequency [Hz]	Lower Temperature Limit [°C]	Upper Temperature Limit [°C]	$\overline{T_{RC}}$ [°C]	$\overline{T_{amb}}$ [°C]	Average Consumption [W]	Average Consumption @ T_{ma} = 5 °C [W]	Heat Gain [W]	COP
54	1	8	5.2	25.2	10.9	11.1	23.6	2.12
54	1	6	3.2	24.9	12.5			
75	1	8	5.1	25.1	12.0	12.1	23.7	1.96
75	1	6	3.1	25.2	13.2			
100	1	8	5.1	25.1	13.0	13.1	23.7	1.81
100	1	6	2.9	25.2	14.7			

On the one hand using the PCM we have the best performance at the lowest frequency of the compressor like it is without the PCM. On the other hand, if we compute the increase in the COP related to the adoption of the PCM for every frequency we will discover that the best case is not 54 Hz. In fact while at 54 Hz the COP moves from 1.90 to 2.12 with an increase of 11.8 %, at 100 Hz the COP passes from 1.55 to 1.81 with an increase of 16.5 %. So the PCM affects relevantly the COP at all the considered frequencies (at 75 Hz we have 11.5 % of increase related to the adoption of the PCM).

Moreover we choose the frequency with the highest COP (i.e. 54 Hz) and we add NaCl to the water to change the PCM freezing temperature. Lowering the freezing temperature we expect that the PCM manages to melt completely during its cycling. The optimized situation would be to have the PCM that begins to melt when a new cycle begins. In this case the PCM would provide all the phase change heat stored during the on-time of the compressor to the compartment without acting as a thermal resistance also in the liquid phase. Fig. 3.10 shows the PCM temperatures during the cycling with the freezing temperature equal to -2 °C.

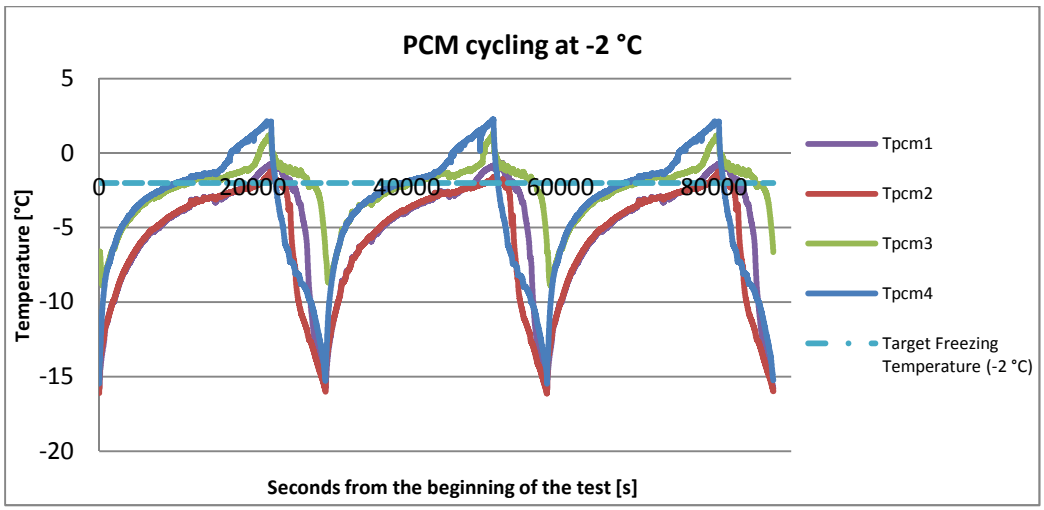

Figure 3.10 PCM cycling with freezing temperature equal to -2 °C.

As we can see in Fig. 3.10 the PCM has a different behavior from what expected. In fact we can see that the PCM freezes and melts completely before the start of the new cycle. It means that the PCM acts both as a thermal resistance during the initial period of the cycle (i.e. ice thermal resistance) and during the last phase of a cycle (i.e. liquid thermal resistance). Using this setup we have higher energy consumptions than in the configuration with only water as PCM. In this case we have only one advantage related to the stability of the RC air temperature. In fact if we lower the freezing temperature, we will have longer cycles that allows the RC air temperature to be more stable. In Fig. 3.11 we compare the RC air temperature trend in three different cases.

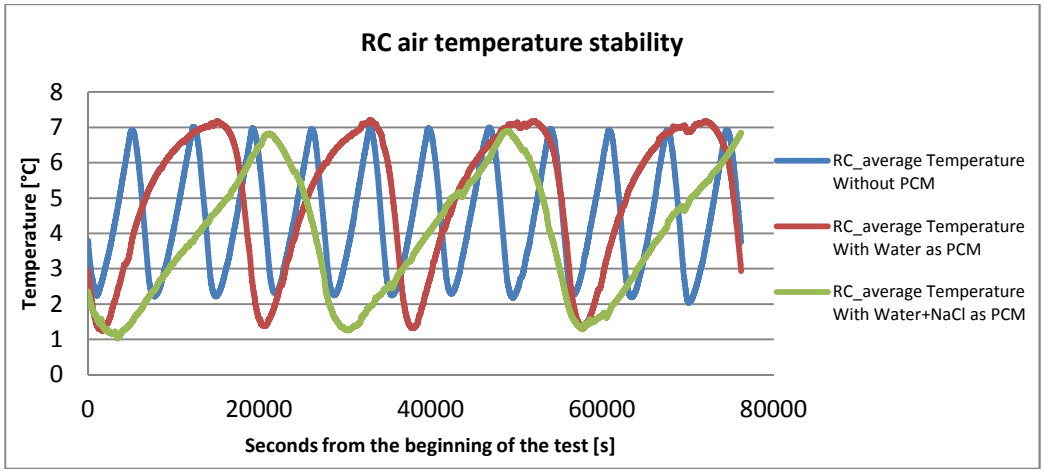

Figure 3.11 RC air temperature stability in three different setups of the appliance.

As we can see in Fig. 3.11 if we have longer dynamics of the system related to lower freezing temperatures we will also obtain a higher constancy of the RC air temperature.
Then we compute the COP for the cases where we use water and NaCl as PCM. The results of this analysis are shown in Table 3.4.

Table 3.4 Calculated and measured data of performance of the appliance at 54 Hz with water plus NaCl as PCM.

Freezing Temperature [°C]	Lower Temperature Limit [°C]	Upper Temperature Limit [°C]	$\overline{T_{RC}}$ [°C]	$\overline{T_{amb}}$ [°C]	Average Consumption [W]	Average Consumption @ T_{ma} = 5 °C [W]	Heat Gain [W]	COP
-2	1	8	4.5	25.2	12.5	12.0	23.8	1.98
-2	2	9.5	5.5	25.3	11.6			
-4	1	8	4.0	25.4	12.7	12.1	23.9	1.97
-4	3	9.5	5.7	25.3	11.6			

In Tab. 3.4 we can observe that if we lower the freezing temperature we will have lower COPs as expected. In fact the reduction of the phase change temperature brings some negative effects in terms of additional thermal resistances between the refrigerant fluid and the air in the RC cabinet. So probably we are already very near to the optimized setup using only water as PCM.
We can also compute the run time of the compressor for the different situations to double check the results that we already obtain calculating the COPs. Our target is to minimize the run time in order to lower the related energy consumptions of the compressor. In Tab. 3.5 we display the computed run times for the different test conditions of the chosen frequency (54 Hz).

Table 3.5 Calculated and measured data of performance of the appliance at 54 Hz with different PCMs.

Freezing Temperature [°C]	Lower Temperature Limit [°C]	Upper Temperature Limit [°C]	$\overline{T_{RC}}$ [°C]	$\overline{T_{amb}}$ [°C]	Run Time [%]	Run Time @ T_{ma} = 5 °C [%]
0	1	8	5.2	25.2	22.45	22.96
0	1	6	3.2	24.9	27.05	
-2	1	8	4.5	25.2	24.14	22.67
-2	2	9.5	5.5	25.3	21.28	
-4	1	8	4.0	25.4	26.66	23.64
-4	3	9.5	5.7	25.3	23.83	

In Tab. 3.5 we interpolate the measured values of run time at different $\overline{T_{RC}}$ to have a comparable value of run time for the different PCMs at $\overline{T_{RC}}$equal to 5 °C. The results show that we have the minimum run time of the compressor with a freezing temperature around -2 °C. If we put together the run time calculations and the COP results we can state that the best freezing temperature for the PCM lies in the range between -2 °C and 0 °C.

3.5 Conclusions

In this section we tried to optimize the freezing temperature of the PCM installed in the RC cabinet of a prototype of built-in refrigerator. We wanted to identify the optimum temperature in the conditions defined in the EN ISO 15502 standard for the energy consumption test. At the beginning we ran several tests to understand the best frequency to run the compressor. This frequency was identified to be 54 Hz. Then we ran six tests using only water as PCM and we computed the increase in the COP. At 54 Hz we reached a COP equal to 2.12 with a 11.8 % augment in the COP related to the adoption of the PCM. Finally we ran four tests using water and NaCl as PCM in order to change the freezing temperature. Lowering the phase change temperature, we observed a negative behavior of the appliance. In fact in this case the PCM acted as an additional thermal resistance having a unconstructive impact on the COP. Moreover we also computed the run time of the compressor and we understood that this parameter reached a minimum around -2 °C. Aggregating the information about COP and compressor run time, we individuated that the optimum freezing temperature for the PCM was in the range between -2 °C and 0 °C. Finally we proposed a PCM freezing temperature equal to -1 °C.

4. Enhancing air heat transfer

4.1 Introduction

In this section we want to obtain the air side heat transfer coefficient of the back wall of the cabinet using different configurations to improve the heat exchange between the foamed-in evaporator and the RC internal air. These data will be used in the last chapter of the thesis as input for the cycle simulation code.
Normally the bottom-mount refrigerator-freezer built-in appliances have a fan in the refrigerator compartment that is used for food preservation. This fan is not used to increase the heat transfer coefficient through forced convection.
In this section there are two different purposes. The first target was to make an experimental study of the air distribution on the back wall of the refrigerator with the standard types of fan already placed into the market products. The second goal was to propose a design strategy to increase the heat transfer using both different fans and multiflows. Another refrigerator was made with an embedded multiflow on the back wall of the RC. Again the multiflow was designed for food preservation issues, i.e. uniform distribution of the air in the cabinet, and not to increase the heat transfer.
All the tests were done on a bottom-mount built-in appliance with a foamed-in evaporator. This appliance has very similar characteristics of the prototype where we take the measurements reported in chapter 3. The only difference is that we measure the air velocities in a refrigerator that does not have a PCM installed in the RC cavity. Once the PCM will be included in a production prototype we will have exactly the same geometrical characteristics as we have on this prototype for the measures of the air speed. In this case the evaporator is not visible and so the back wall appears like a white flat vertical surface. All the measurements were taken with anemometers suitable for the different ranges of speed. In Tab. 4.1 we show the main characteristics of the three types of hotwire anemometers.

Table 4.1 Main characteristics of the utilized hotwire anemometers.

Sensor Model	Measurement Range	Measurement Accuracy
UAS1100PC	0.1 m/s to 1 m/s	+/- 0.051 m/s
UAS1200 PC	0.5 m/s to 5 m/s	+/- 0.051 m/s
UAS1300PC	4.5 m/s to 20 m/s	+/- 0.025 m/s

During all the experimental campaign we run the tests with appliance switched off and the front door closed. The three internal shelves were positioned in the standard positions. The fans were activated from the external room plugging them to electrical supply. The fans were always started with the front plastic mask. The mask creates additional pressure losses that the fan should win in

blowing the air. Anyway we cannot remove the mask because its presence is fundamental for issues regarding customer acceptability. We decided to take 30 or more samples for each measure point. Then we computed the standard deviation of the experimental values and we always obtained very low values of this parameter. So we decided to take the average of the measured values as the representative value of the air speed in the considered measure point.

4.2 Definition of the baseline

In order to measure the increase in the heat transfer caused by fans and multiflows we should first define the baseline case. Our baseline corresponds to the situation where we have only natural convection and radiative heat transfer phenomena. In particular we assume a standard operating condition to compare the different cases. We choose this condition looking at different measurements taken on similar appliances. Table 4.2 summarizes the main parameters that describe the standard condition.

Table 4.2 Peculiar characteristics of the standard operating conditions.

Surface temperature of the back wall	-23 °C
Side walls and front wall temperature	6.9 °C
Air temperature inside the cabinet	5 °C
Back wall evaporator surface	38 cm x 65 cm
Characteristics of the surface	Vertical flat white surface

First we estimate the heat transfer coefficient for natural convection through the following formula.

$$\overline{Nu}_L = \frac{\bar{h} * L}{k} = \frac{4}{3} * \left(\frac{Gr_L}{4}\right)^{1/4} * g(\mathrm{Pr}) \quad (4.1)$$

$$with$$

$$g(\mathrm{Pr}) = \frac{0.75 * \mathrm{Pr}^{\frac{1}{2}}}{\left(0.609 + 1.221 * \mathrm{Pr}^{\frac{1}{2}}. + 1.238 * \mathrm{Pr}\right)^{1/4}} \quad (4.2)$$

The Grashof number is calculated through the following definition.

$$Gr_L = \frac{g * \beta * (T_s - T_\infty) * L^3}{\nu^2} \quad (4.3)$$

So we take equation (4.1) to compute the share of heat caused by natural convection in every different case.
In order to compute the radiative share in the heat transfer we try to follow two different approaches.
First we assume that our refrigerator cabinet is made only of two vertical infinite surfaces (i.e. back wall and front wall). Fig 4.1 represents the schematization of the radiative heat transfer problem.

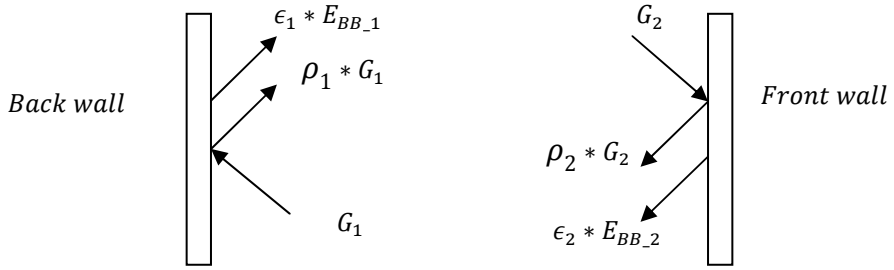

Figure 4.1 Sketch of the radiative heat transfer problem.

Making an energy balance on one of the two surfaces we can write the following expression that correlates the radiosity (J) with irradiation (G) and the black body emissive power (E_{BB}).

$$J = \epsilon * E_{BB} + \rho * G \quad (4.4)$$

We assume that the two surfaces are opaque and that they could be schematized as gray bodies. Using these assumptions we can write the following formula.

$$\rho + \alpha = \rho + \epsilon = 1 \quad (4.5)$$

Substituting equation (4.5) in equation (4.4) we obtain the subsequent equation.

$$J = \epsilon * E_{BB} + (1 - \epsilon) * G \quad (4.6)$$

We can write the net radiative flux from the back wall (i.e. surface number 1) to the front wall (i.e. surface number 2) in the following manner.

$$\Phi_{net1} = A_1 \epsilon_1 * (E_{BB1} - G_1) \quad (4.7)$$

From equation (4.6) we can get the irradiation and we can substitute it in equation (4.7) obtaining the subsequent formula.

$$\Phi_{net1} = \frac{A_1 \epsilon_1}{1 - \epsilon_1} * (E_{BB1} - J_1) \quad (4.8)$$

The same operation could be performed to obtain the net radiative flux from the front wall. Moreover we can also apply an energy balance to an imaginary surface between the back and the front walls obtaining this expression.

$$\Phi_{net1} = \sum_{i=1}^{2} A_i * F_{ij} * (J_i - J_j) \quad with\ j = 1\ ;\ 2 \quad (4.9)$$

In Fig. 4.2 we schematize this approach with an equivalent resistance network that was firstly introduced by Oppheneimer.

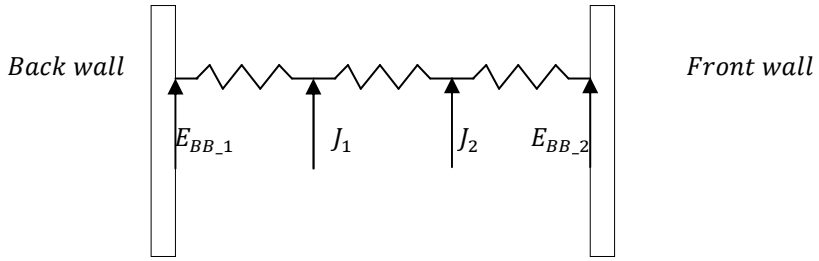

Figure 4.2 Sketch of the equivalent resistance network for the radiative problem.

We now make the assumption that every surface can only see the other one and so the view factors are equal to 1. Moreover we also consider only one value of emissivity for both the front and the back wall. Using these hypothesis we can write the net radiative flux in the following manner.

$$\Phi_{net1} = \frac{A_{wall} * (E_{BB1} - E_{BB2})}{\frac{2}{\epsilon} - 1} \quad (4.10)$$

We finally set the value of emissivity equal to 0.9 that is a reasonable value for a flat plastic surface.
In the second approach that we adopt to compute the radiative heat transfer, we schematize our cabinet as a parallelepiped made of four infinite surfaces. In this particular case we can approximate the view factors in the following manner.

$$F_{ij} = \frac{A_j}{A_{tot-i}} \quad where\ A_{tot-i} = \sum_{j=1}^{3} A_j\ with\ j \neq i \quad (4.11)$$

So for example we can compute the view factor from surface number 1 to surface number 2 just dividing the area of the second surface by the sum of the area of all the other surfaces except the surface number 1. In table 4.3 we show the calculation of the heat flux for every internal wall of the cabinet.

Table 4.3 Synthesis of the second approach to compute the radiative flux of the back wall.

Surface	Couple of surfaces	$T_i\ [K]$	$A_i[m^2]$	ϵ_i	F_{ij}	Φ_{netij} [W]
Back wall – Surface number 1	1--2	250,15	0.247	0,9	0,3114	8,78
	1--3	250,15	0.247	0,9	0,3442	9,70
	1--4	250,15	0.247	0,9	0,3442	9,70
Front wall – Surface number 2	2--1	280,05	0.247	0,9	0,3114	7,80
	2--3	280,05	0.247	0,9	0,3442	0
	2--4	280,05	0.247	0,9	0,3442	0
Right side wall - Surface number 3	3--1	280,05	0.273	0,9	0,3220	8,91
	3--2	280,05	0.273	0,9	0,3220	0
	3--4	280,05	0.273	0,9	0,3559	0
Left side wall - Surface number 4	4--1	280,05	0.273	0,9	0,3220	8,91
	4--2	280,05	0.273	0,9	0,3220	0
	4--3	280,05	0.273	0,9	0,3559	0

From table 4.3 we can see the different share of heat flux that the back wall exchange with the other surfaces. So we can obtain an average heat transfer coefficient in the following manner.

$$h_{rad-average} = \frac{\Phi_{net1-2} + \Phi_{net1-3} + \Phi_{net1-4}}{\left(T_{back-wall} - T_{other-surfaces}\right)} \quad (4.12)$$

Since the results of both the approaches give comparable results, we finally choose to adopt the approach that mostly reflects the geometrical characteristics of our problem. So we compute the radiative heat transfer coefficient using the second approach. Finally we can compute the baseline heat exchange in the standard conditions. In Tab.4.4 we show the total heat flux and the radiative and convective shares in the standard conditions.

Table 4.4 Baseline heat transfer from the back wall of the cabinet.

	Heat Transfer Coefficient $[W/m^2\,K]$	Heat Flux [W]
Natural convection	2.93	20
Radiative	4.07	28
Total	7.00	48

4.3 Experimental testing of the standard configurations

There are three different simple configurations available in the existing bottom-mount market appliances.
The first case is shown in Fig. 4.3 and it corresponds to an appliance with a big propeller fan (white) fixed on the top of the back wall. In the second case shown in Fig 4.4 we have a small propeller fan (black) mounted on the top of the back wall.

Figure 4.3 Big propeller fan.

Figure 4.4 Small propeller fan.

Both these fans have a very limited volume flow rate and so they are useless for the heat exchange. This last statement is also based on the experimental campaign that we perform. In particular we measure the air speed in different points of the back wall as shown in Fig 4.5.

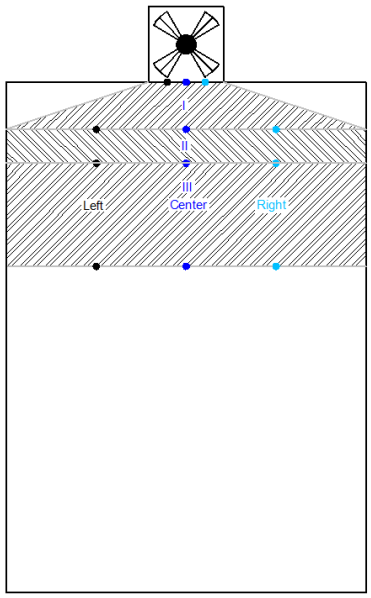

Figure 4.5 Sketch of the positions of the anemometers and of the sectors of the back wall of the cabinet.

As we can see in Fig. 4.5 in this case we decide to measure the air speed at four different distances from the exit of the fan (0 cm, 7 cm, 10 cm and 21 cm). In primis we measure the speed at the exit point of the fans in order to compute the volume flow rate. The exit of the fan has an area equal to 0.0012 m^2 (1.5 cm x 8 cm). So the volume flow rate of the big propeller fan results equal to 8.4 m^3/h, while the one of the small propeller fan is equal to 4.7 m^3/h. In Fig. 4.6 and 4.7 we show the results of the measurements of the air speed for both the small and the big fan.

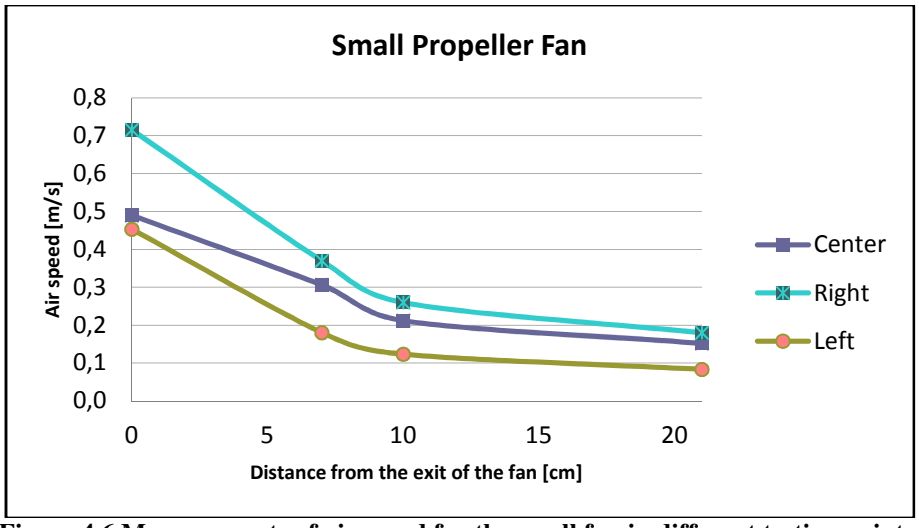

Figure 4.6 Measurements of air speed for the small fan in different testing points.

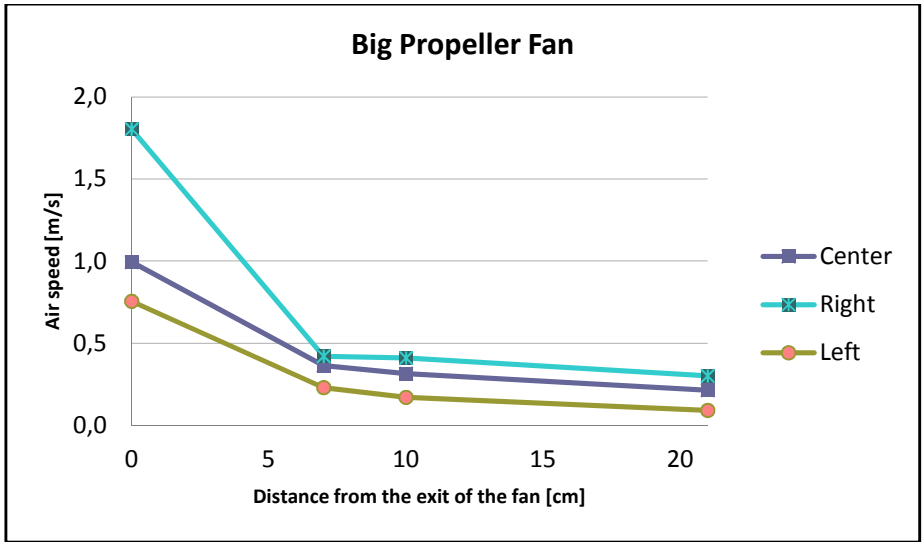

Figure 4.7 Measurements of air speed for the big fan in different testing points.

As we can see from Fig. 4.6 and Fig 4.7 both these fans creates just little movements of the air inside the cabinet. Moreover the air is basically blocked under the second shelf and so we would probably have a problem of temperature gradient caused by the air stratification in the most part of the refrigerator. We also try to compute the increase in the heat transfer for the two configurations. We used the following correlations to compute the forced convection heat transfer coefficient [9].

$$Only\ Laminar: \overline{Nu_x} = 0.664 * Re_x^{\frac{1}{2}} * Pr^{\frac{1}{3}} \quad (4.13)$$

$$Only\ Turbulent: \overline{Nu_x} = 0.037 * Re_x^{\frac{4}{5}} * Pr^{\frac{1}{3}} \quad (4.14)$$

$$Laminar\ and\ Turbulent: \overline{Nu_x} = \left(0.037 * Re_x^{\frac{4}{5}} - A\right) * Pr^{\frac{1}{3}}\ with\ A$$
$$= 0.037 * Re_{x,c}^{\frac{4}{5}} - 0.664 * Re_{x,c}^{\frac{1}{2}}\ and\ Re_{x,c} = 2500 \quad (4.15)$$

In particular we made an average of the measured speeds on every line so that we have a single value of speed for every of the three selected sectors. Since the air velocities are very low (less than the accuracy of the anemometers, i.e. 0.15 m/s) under the fourth measure line, we neglect the forced convection in the white sector of Fig. 4.8. The results of the calculations are displayed in Fig. 4.8.

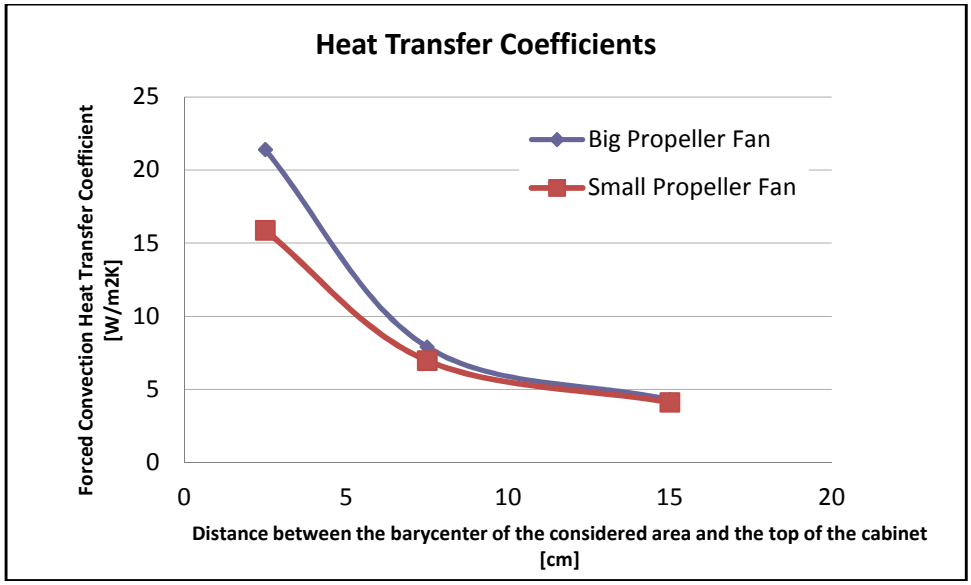

Figure 4.8 Calculated heat transfer coefficients for every area shown in Fig. 4.5 for the big and the small propeller fans.

To obtain the increase of the heat transfer from the baseline case we put together the effects of natural and forced convection. In particular we are in the peculiar situation of combined free and forced convection. In fact in our application we have $Gr_L/Re_L^2 \approx 1$. The forced convection is influenced by the effects of buoyancy. The impact phenomena varies according to the mutual directions of the buoyancy forces and the forced flow. Since in our case the fans are placed on the top of the back wall, we have a so called "assisting flow". In fact both the buoyancy forces and the forced flow have the same direction. We correlated the effects of natural and forced convection through the following expression [9].

$$Nu^3_{tot-convection} = Nu^3_{forced-convection} + Nu^3_{natural-convection} \quad (4.16)$$

As we can see in equation (4.16) we have a plus sign between the Nusselt's number to take into account that we are in the situation of assisting flow. So we finally combined the forced and the natural convection Nusselt's numbers for our case and we made a weighted average of these values on the corresponding surfaces obtaining the increase of the heat transfer from the baseline case. We realize that the big propeller fan increases the heat exchange of 13.2% from the baseline and that the small propeller fan increases the heat exchange of 5.15 %.
Since the small propeller fan turns out to have a little impact on the heat exchange we decide to consider only the big propeller fan in the other configurations.
The third configuration that is already available on market appliances consists in combining a fan of the second configuration with a multiflow. The multiflow is

a plastic channel with a cross section of 12.5 cm x 1.5 cm. In Fig. 4.9 we show the typical multiflow used on the appliances.

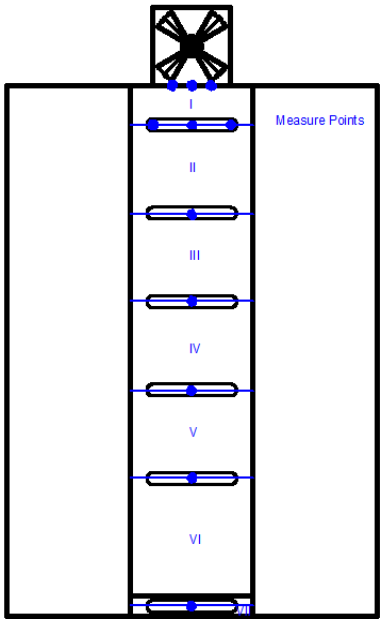

Figure 4.9 Sketch of the standard multiflow with the measure positions.

From Fig. 4.9 we can see that the multiflow has frontal holes to make the air circulating on the shelves into the cabinet. It also has some small lateral holes for the same reason. From an heat exchange point of view all the air that exits from the multiflow through the holes is useless. In fact once the flow leaves the back wall, it becomes irrelevant to increase the heat exchange on the back wall.
We measure the air speed of the flow on the back wall at the altitude of every frontal hole. Then we divide the surface of the multiflow in seven small surfaces where we compute the heat transfer. We use equation (4.13), (4.14) and (4.15) to compute the heat transfer also in this case. Since we have only one cold surface (i.e. the back surface) that is exchanging heat with the air, we do not utilize correlations for a rectangular channel that are valid only in the case that all the surfaces of the channel are isothermal or isoflux. In this way we are sure that we won't overestimate the heat transfer coefficient in the multi-flow channels. In particular in every little surface we calculated a velocity equal to the average between the two values of the nearest front holes and then we used this value of speed in the correlations. The measured and the calculated results are shown in Fig. 4.10 and fig. 4.11.

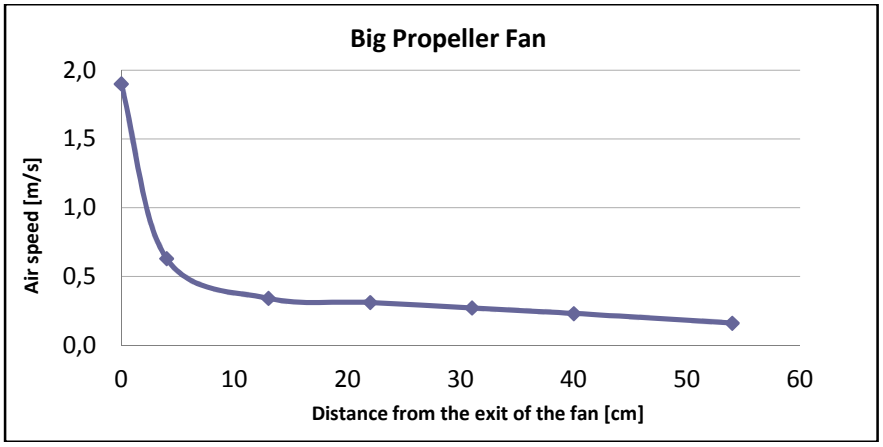

Figure 4.10 Measured air velocity produced by big propeller coupled with multi-flow.

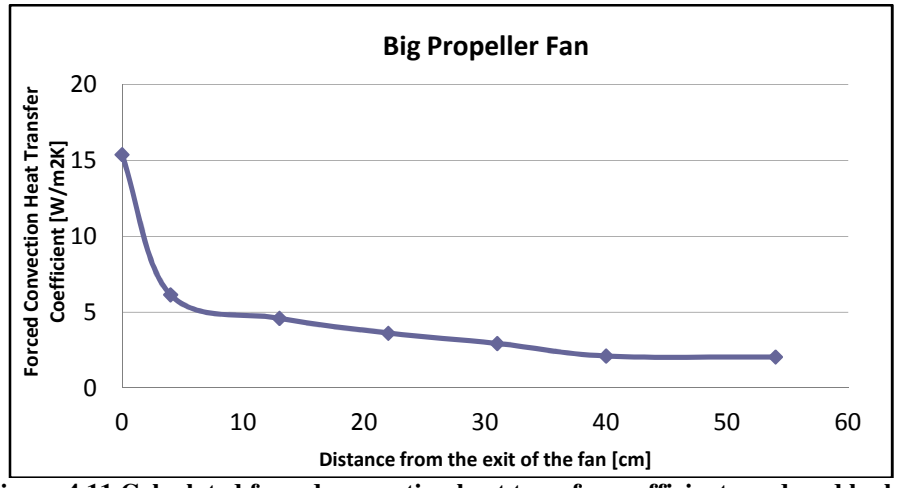

Figure 4.11 Calculated forced convection heat transfer coefficient produced by big propeller and multi-flow.

In this case we have an increment of the heat transfer from the baseline case equal to 15.22 % . In fact the exiting air flow from the fan is no more diverted by the shelves, but it is very well preserved close to the wall by the multi-flow channels.

4.4 Experimental testing of the new configurations

4.4.1 Centrifugal fan and multiflows

In this section we explain the results of the measures taken on the appliance using a new fan. In particular we installed a centrifugal fan made by Delta Electronics. The datasheet declares a range of operation voltage from 4 V to 13.8 V. At the maximum speed (i.e. 3200 rpm) the fan requires a power of 6.84 W. The declared maximum air flow rate at zero static pressure is equal to 38.4 m^3/h. Finally in the worst conditions the fan produces 49 dBa of acoustical noise

at the distance of 1 meter from the fan. Since there is a relevant issue regarding the acoustic of the fan he most part of the measures were taken at low voltages. In particular we limit our analysis to 1.5 V, 3 V and 4.5 V. Moreover the selection of the voltages is also performed to have a similar power to the one of the normal big fan already available in the appliance. So we choose only the voltages that give a required power of less than 3 W. This power has a non-negligible effect on the performances of the refrigerator. In fact on the one hand the power of the fan is an additional contribution that should be computed during the energy consumption test, on the other hand the heat released by the fan forces the compressor to give a higher cooling capacity to maintain the internal temperature of the cabinet at the set point. So the power of the fan is considered twice during the energy consumption test and for this reason it is common to switch off the fan during the test. To adapt the voltage at the desired values we use a selector directly positioned on the plug to the electrical supply. Even if two out of the three chosen voltages are out of the operation voltage range declared by the manufacturer, the fan always works in a proper way without having any kind of problems also for long on periods (i.e. 24 hours).
Moreover we run the fan at different voltages from 1.5 V to 12 V measuring the speed in the exit section and computing the volume flow rate. In particular we identify five measure points dividing the exit section of the fan (5.4 cm x 2.9 cm) in six little areas a. Fig 4.12 shows the exact position of the measure points.

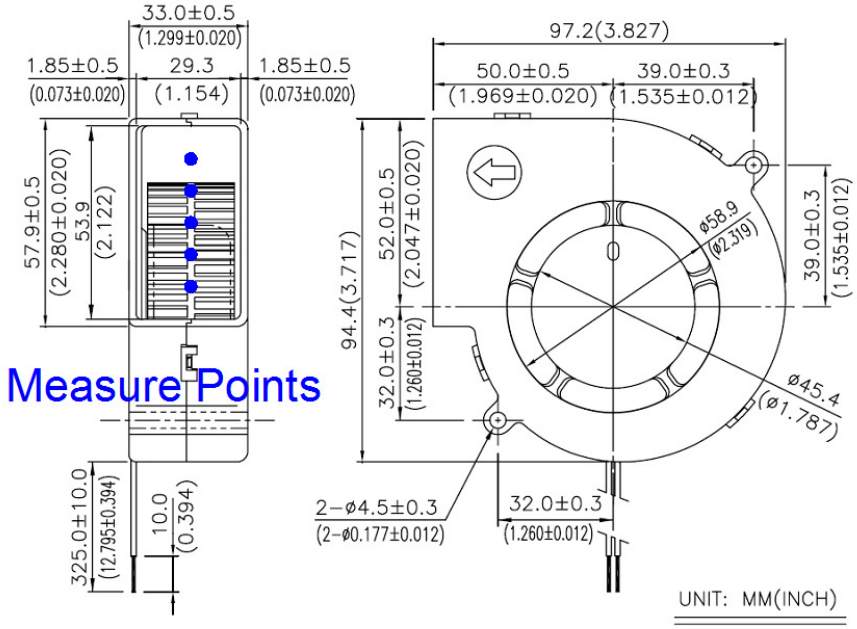

Figure 4.12 Position of the measure points in the exit section of the fan.

Using the experimental data we compute the volume flow rate making an average of the measured speeds and multiplying it for the exit section area.

Surprisingly the measured volume flow rate at the maximum speed comes to be more than the value of the datasheet. We display the results of our analysis in Fig 4.13.

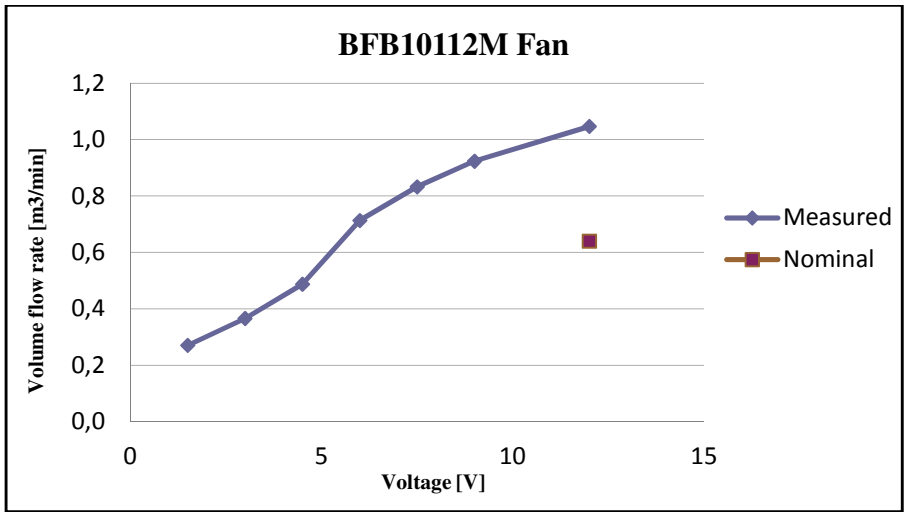

Figure 4.13 Volume flow rate of the BFB10112M fan at different voltages.

As we can see in Fig 4.13, on the one hand we have the classical linear trend between the volume flow rate and the voltage, on the other hand we have a volume flow rate equal to 62.4 m^3/h at 12 V. So our fan manages to provide 62 % air flow rate more than what declared in the datasheet.
Then we also study the speed profile at the exit of the fan. Since we are analyzing a centrifugal fan we do not expect to have an uniform speed profile in the outlet section. In particular we foresee higher velocities going from the center to the outside of the cochlea. In Fig. 4.14 for example we show the measured velocities at 12 V.

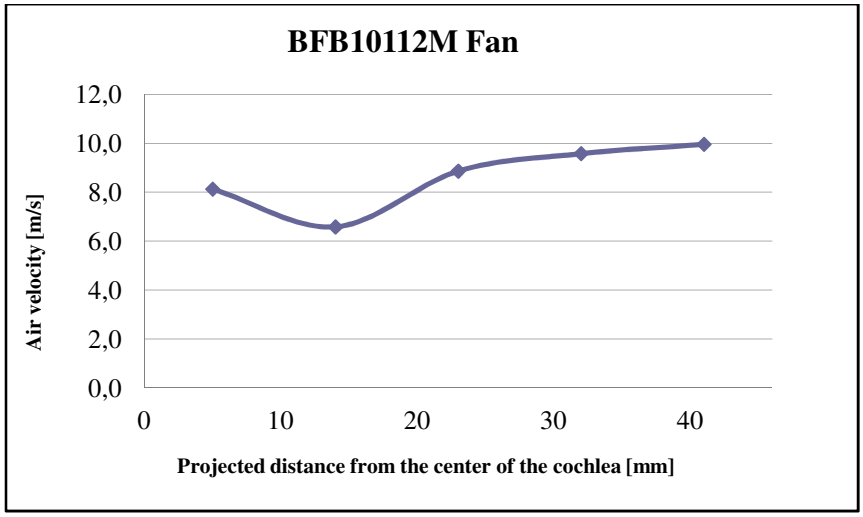

Figure 4.14 Air speed in the exit section of the BFB10112M fan.

As we can see in Fig 4.14 our prediction are in agreement with the experimental results. The more the distance from the center of the cochlea increases, the more the air velocity gets higher. In the first millimeters the trend is not in agreement with the experimental measurements because of some block effects. In particular these effects are cause by a small plastic fin inserted inside the cochlea.
Then we create the first new configuration coupling the new fan with the existing multiflow. In particular the BFB10112M fan was installed in the same position of the usual one, but it was rotated of 15 degrees in order to match the velocity profile at the exit of the fan with the shape of the multiflow. In fact we observe that if we install the fan without any rotation we will lose lots of air through the first two lateral holes on the right side of the multiflow. Furthermore we measure the speed of the air in the multiflow keeping the same measure points as in section 4.3. Fig. 4.15 and Fig. 4.16 illustrate the experimental values of air speed and the calculated values of forced convection heat transfer coefficient for the three considered voltages of the fan.

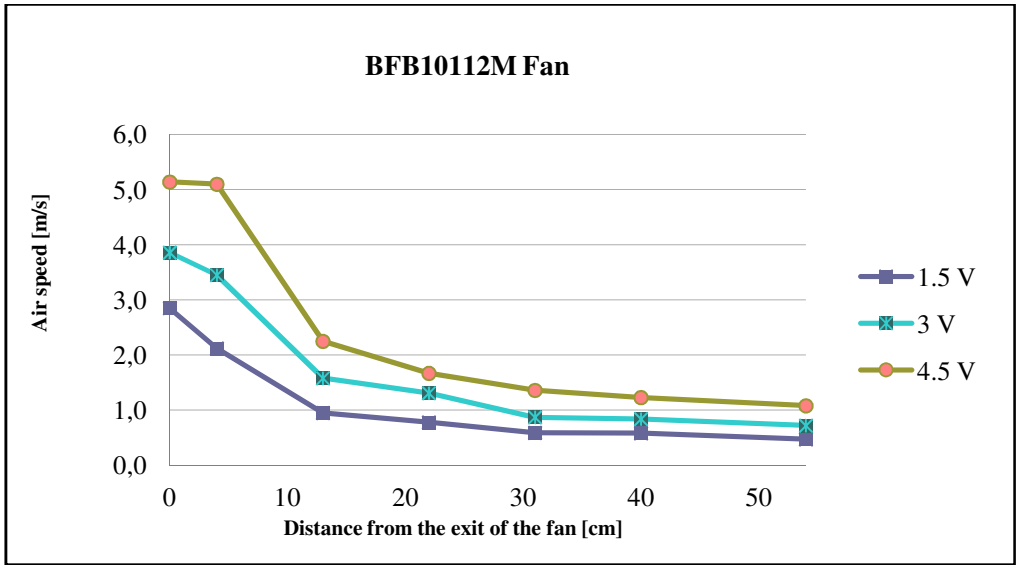

Figure 4.15 Air speed in the configuration with the multiflow and the BFB10112M fan.

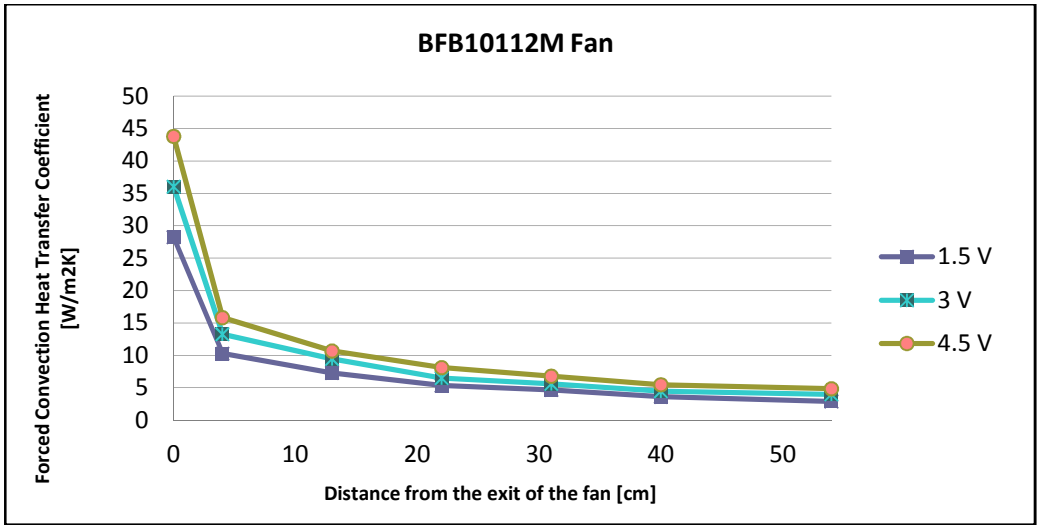

Figure 4.16 Calculated forced convection heat transfer coefficient produced by BFB10112M fan and multi-flow.

As we can see from Fig. 4.15 in this new configuration we always have relevant velocities into the multiflow. Keeping more or less the same required electrical power, the new fan is much more efficient in moving the air than the normal big one. Anyway the final increase on the heat transfer is still not so relevant as expected. In fact, for the best case of 4.5 V we have an increase of 17.1 % from the baseline. The reason for this result is that still lot of the air volume flow rate that is lost through the holes of the multiflow.

Starting from the last consideration we decide to design a new multiflow (1st multiflow) that can distribute the air on the back wall in a better way. As a first try we create a rectangular multiflow of the same size of the back wall (38 cm x 65 cm) with a thickness equal to 1 cm. We measure the speed in nine points at the bottom of the multiflow. To be conservative, we compute the heat transfer coefficient dividing the back wall into the ten ideal areas that are shown in Fig.4.17. Eight of them have velocities equal to the measured ones at the bottom. The other two of them are in the upper part of the multiflow where there less movement of air. In these two sections we measure the air speed in 18 different points spread in both the areas and we make two averages to obtain the value of speed for every area. A sketch of the new multiflow and of the measure points is shown in Fig. 4.17.

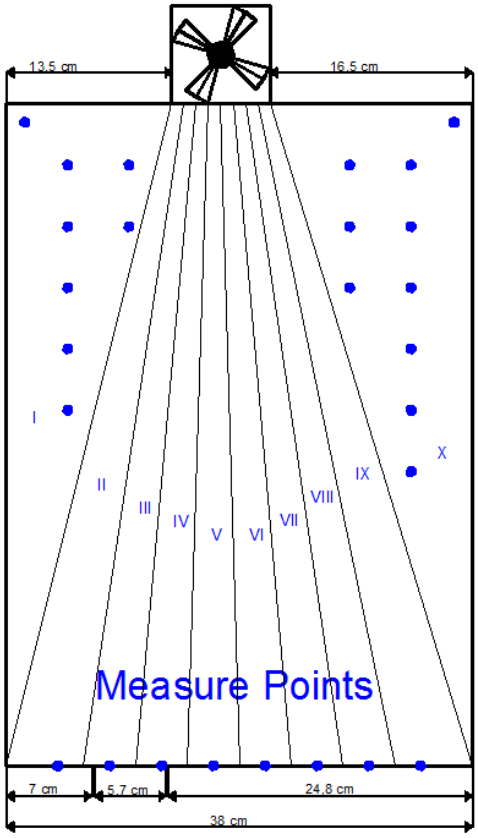

Figure 4.17 Sketch of the 1st designed multiflow with measure points.

Moreover to maximize the heat transfer we aim at having a more uniform speed profile. To accomplish this target we design another multiflow (2nd multiflow) similar to the previous one. The new multiflow keep the same external structure of the old one, but three internal plastic fins are inserted to create three separate channels for the air. The heat enhancement from the baseline is computed using the same area technique already adopted in the calculation of the 1st designed multiflow. Since we know the profile of the speed at the exit of the fan, we design a multiflow with larger channels in the sections where the speed is higher and on the opposite smaller channels where we have lower air speeds. The structure and the measure points of the 2nd designed multiflow are displayed in Fig 4.18.

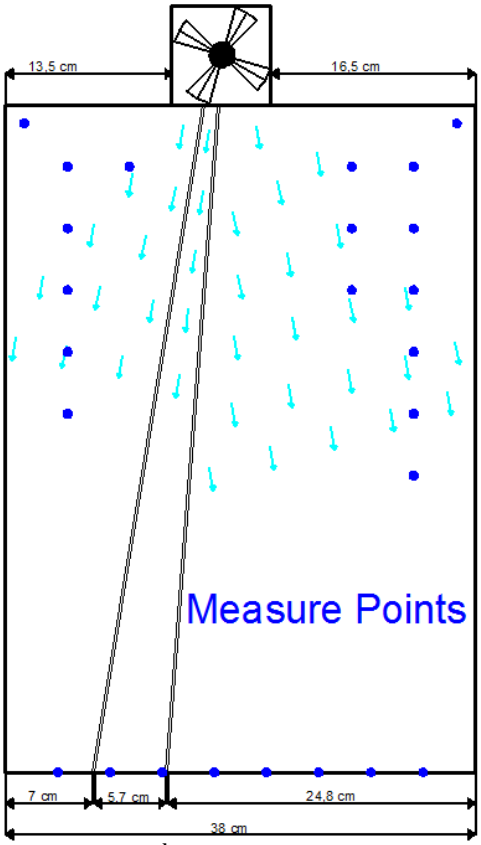

Figure 4.18 Sketch of the 2nd designed multiflow with measure points.

So lastly we measure the air speeds at the bottom points of the multiflow and we compare the speed profiles. Fig 4.19 shows the comparison between the velocity profiles of the two designed multiflows.

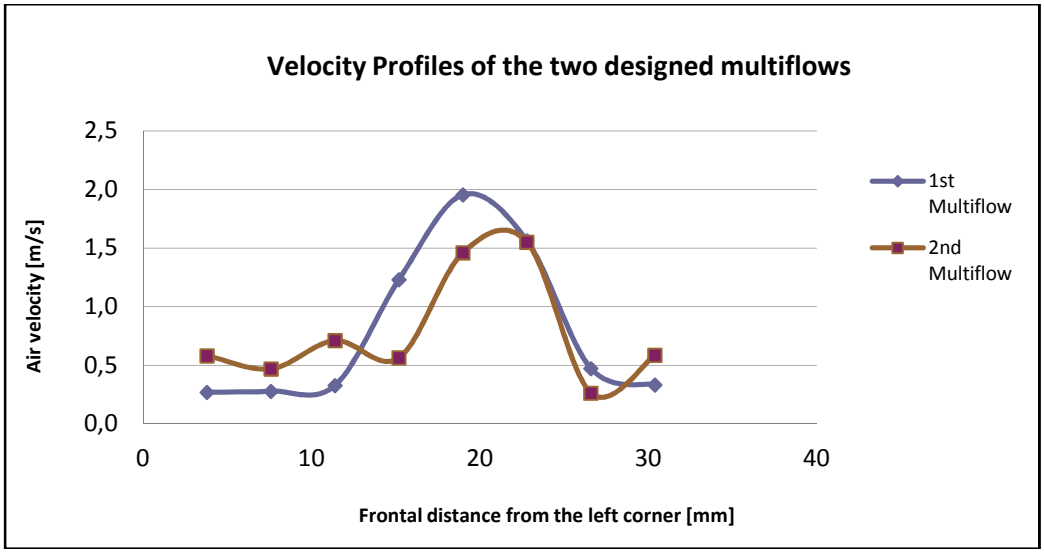

Figure 4.19 Air speed profiles at the bottom of the multiflows for the two designed multiflows.

As we can see in Fig. 4.19 the added plastic fins in the second multiflow have a relevant impact on the uniformity of the velocity profile inside the channels. In fact the 2nd multi-flow shows slightly more uniform velocity profile of the exiting air, even though there is still a significant velocity maximum in the center of the multi-flow. While with the 1st designed multiflow we have an absolute average deviation from the mean velocity of 0.57 m/s (maximum absolute deviation equal to 1.22 m/s) , in the second case we reduce this value to 0.34 m/s (maximum absolute deviation equal to 0.82 m/s). Since in the second case we have a more uniform velocity on the back wall we also expect to have a larger increase in the heat exchange from the baseline case. In Tab. 4.5 we summarize the positive effects of the designed multiflows in terms of heat exchange.

Table 4.5 Outputs of the experimental campaign on the new designed multiflows.

	1st Multiflow	2nd Multiflow	1st Multiflow	2nd Multiflow
Fan Voltage [V]	3	3	4.5	4.5
Heat exchanged in the examined conditions [W]	62	63	66	67
Heat exchange increase from the baseline [%]	27	29	37	39

As we can see in Tab. 4.5 using this kind of multiflows we have a relevant increase in the heat exchange. The basic difference from the standard multiflows is that we do not have any frontal openings that waste the air flow rate.
Adopting these new multiflows, on the one hand, we have big advantages on the heat exchange side, on the other hand we can have some problems related to food preservation. In fact the new configurations try to force the air to move only into the multiflow and not into all the cabinet. This assumption means that in the cabinet we have more temperature stratification that can damage the food. So finally we try to design a model of multiflow that can solve at the same time both the issues. Fig. 4.20 shows a sketch of the third model of multiflow that takes care of heat exchange and food preservation aspects.

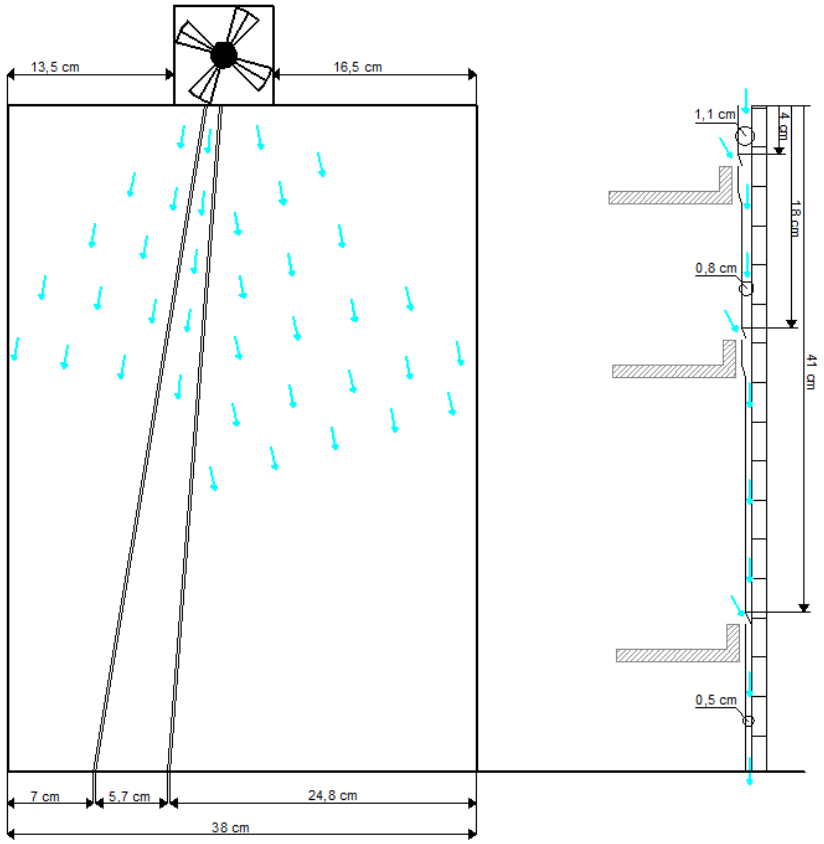

Figure 4.20 Internal sketch of the profile of the third designed multiflow.

This multiflow aims at maximizing the heat transfer performances that a centrifugal fan can provide. As we can see in Fig. 4.20 the new multiflow is divided into three channels with the same geometry of the ones of the 2nd designed multiflow. It also has frontal fissures that allow the movement of the air inside the cabinet. However these holes plays a very different roles from the ones of the standard multiflow. The volume flow rate blown by the fan is not

wasted through these openings. The air inside the multiflows moves the air in the cabinet dragging it through the three frontal holes. Moreover the section of the multiflow decreases going from the top to the bottom in order to maintain always a minimum velocity to catch the air inside the cabinet. Using this multiflow we expect to have the same increase in the heat exchange as for the 2nd designed multiflow, but we avoid the problems related to the air movement and to the temperature stratification into the cabinet. To obtain further improvements in the heat exchange in the future, we suggest to build and test this multiflow.

4.4.2 Tangential fan and multiflows

Since we want to maximize the heat transfer coefficient, we would like to have a uniform profile of air speed on the back wall of the cabinet. So we decide to order and to test a tangential fan. Tangential fans are composed by an impeller with forward curved blades and a housing to throw the air in the required direction. In this case the air flow moves in one direction across the impeller. We select the fan to match both the requirements about the flow rate and the ones regarding the temperatures. In Fig. 4.21 we display the result of the selection.

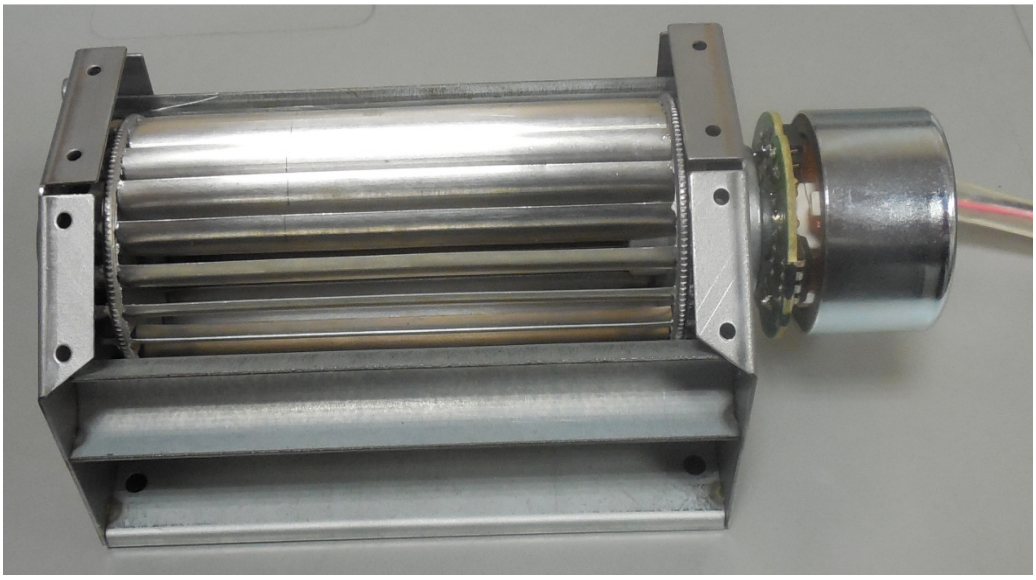

Figure 4.21 The selected tangential fan.

This fan provides a maximum flow rate of 68 m^3/h. The air flow follows a 90 ° path entering from the top of the device and exiting in the front part. The fan has an operating voltage r from 9 V to 24 V. We decide to run and to test the fan only for voltages that imply required powers that are less than the power of the standard fans installed on the appliances (i.e. 2.8 W). At the beginning we run the fan at 9 V, 10 V, 12.5 V and 15 V to measure the provided air flow rates. We

divide the frontal opening in five equal areas and we measure the speed in four points. We make an average of the measured speeds to obtain the averaged speed on the exiting area of the fan. Then we compute the flow rates measuring the geometrical parameters of the frontal opening. At the same time we also measure the required power for every conditions. In Tab. 4.6 we show the results of this operation.

Table 4.6 Measured values for the tangential fan at four different voltages.

Voltage [V]	Averaged speed [m/s]	Flow rate [m^3/h]	Power [W]
9	3.6	34	0.81
10	4.1	39	1.05
12.5	4.6	44	1.75
15	5.2	49	2.7

From Tab. 4.6 we can induce that the fan is more efficient at low voltages. For example if we want to double the flow rate that we have at 9 V (i.e. 33.7 m^3/h) it is more efficient to use two equal fans than to increase the voltage of the single fan. We can also observe that the tangential fan has an higher efficiency than all the other considered fans. For example if we make a comparison of the provided flow rates of all the fans at 2.7 W, we will discover that the tangential fan gives 67 % more flow rate than the most efficient fan (i.e. the centrifugal) of the old ones. In Fig. 4.22 we plot the speed profile at the exit of the fan for the four considered voltages.

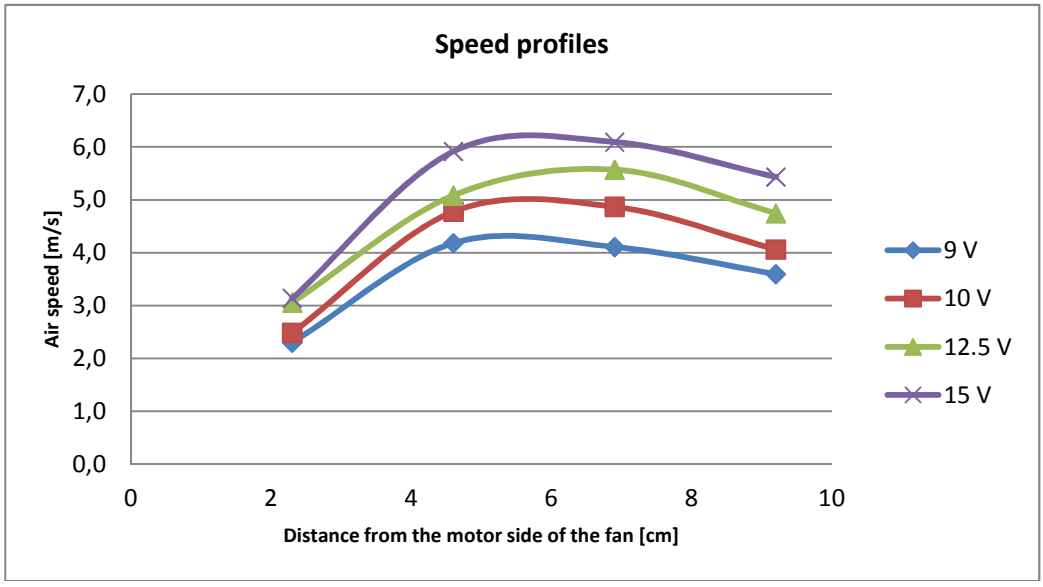

Figure 4.22 Speed profile at the exit section of the tangential fan.

From Fig. 4.22 we can induce that the speed profile is much more uniform than for the other fans. We can notice that in the first section near the motor we have lower speeds and then they tend to increase and to assume a stable value. So probably if we find a longer fan, we will have a more uniform profile.

Moreover we measure the speed in different points of the back wall to estimate the heat transfer improvement. In Fig. 4.23 we show the measure points (i.e. the blue points) and the areas to compute the heat transfer improvement in this configuration.

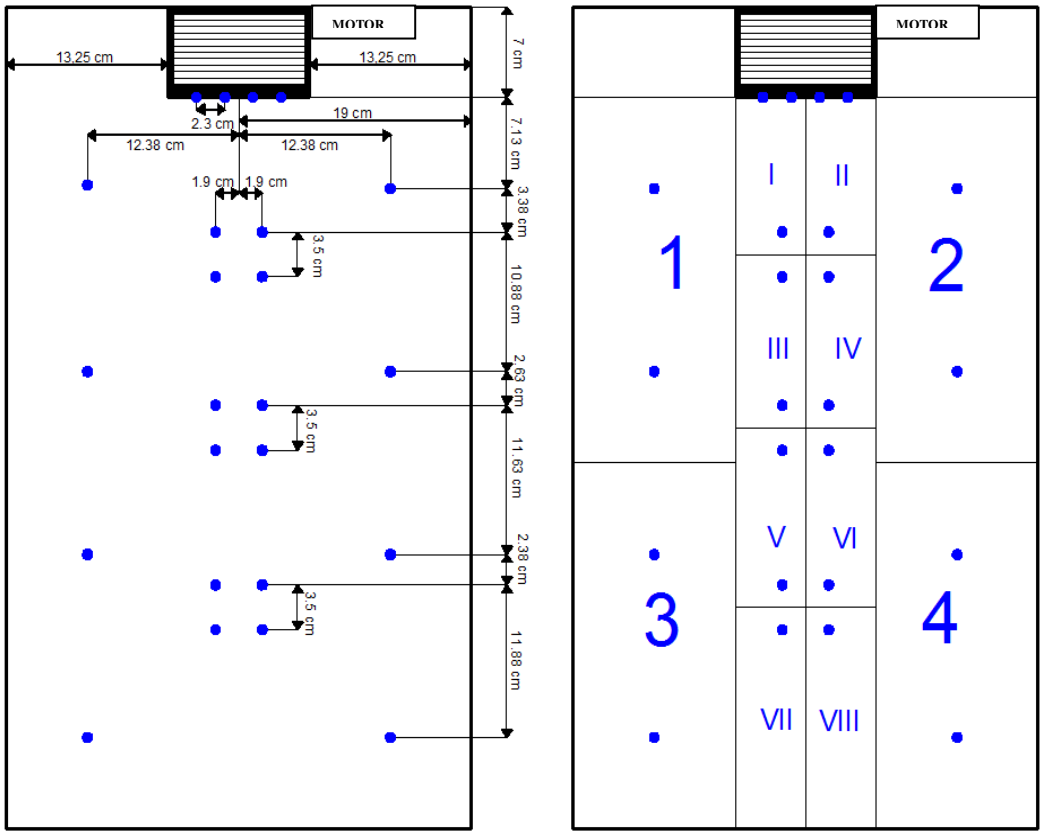

Figure 4.23 Measure points of the air speed using the tangential fan.

As we can see in Fig. 4.23 we divide the back wall in twelve different areas. In this areas we compute the forced convection heat transfer coefficients. In every area we apply the thermal correlations considering the averaged speed among the included measure points. In Fig. 4.24 we show the measured air speeds in the different point with the supply voltage equal to 9 V.

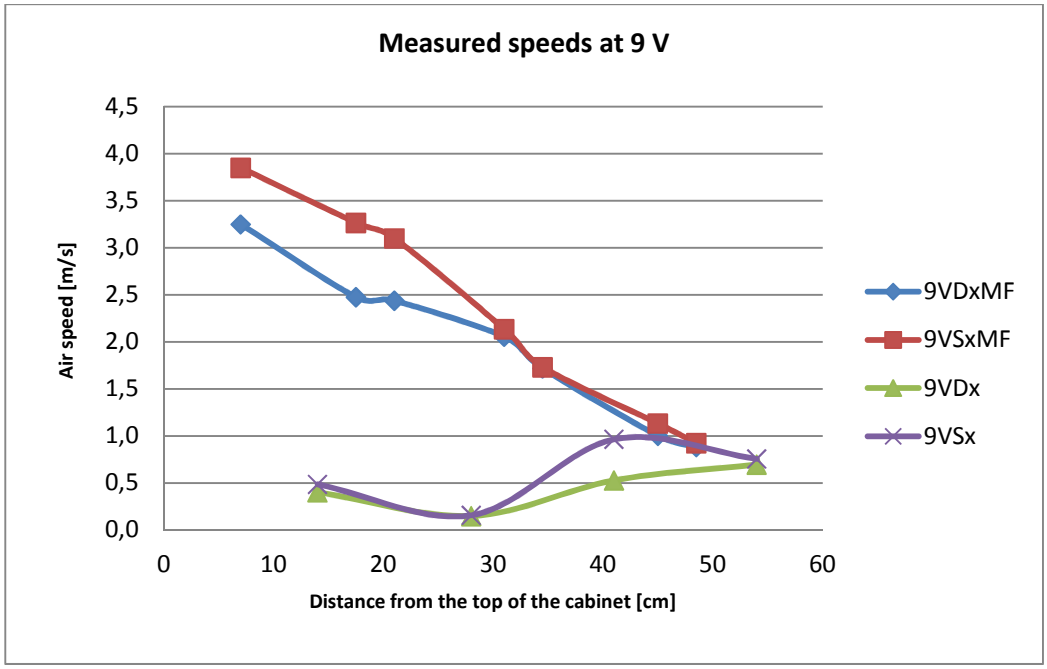

Figure 4.24 Measured air speeds in the different testing points at 9 V for the tangential fan.

In Fig. 4.24 we can see the typical trends of the air speed in and out of the main flow (MF). As we can expect from the measures of the speed at the exit section of the fan, in the upper part of the back wall the air speeds enlarge increasing the distance from the fan motor. In the lower part of the back wall the air speeds in the main flow tend to assume the same values. In fact in Fig. 4.24 we can see that the air speeds that are included in the areas I, III, V and VII (i.e. 9VSxMF trend) initially assume higher values than the air speeds that are measured in the areas II, IV, VI, VIII (i.e. 9VDxMF trend). Moreover we can observe that the speeds of the areas 1 and 3 (i.e. 9VSx trend) and the speeds of the areas 2 and 4 (i.e. 9VDx trend) have a similar tendency. On the one hand, we probably have turbulence in the upper part of area 1 and 2 that increases the air velocity. On the other hand, the main flow starts to spread on all the back wall after the bottom part of area 1 and 2 where in fact we notice minimums in the measured speeds. Moreover in Fig. 4.25 we show the computed heat transfer coefficient for every area identified in Fig. 4.23.

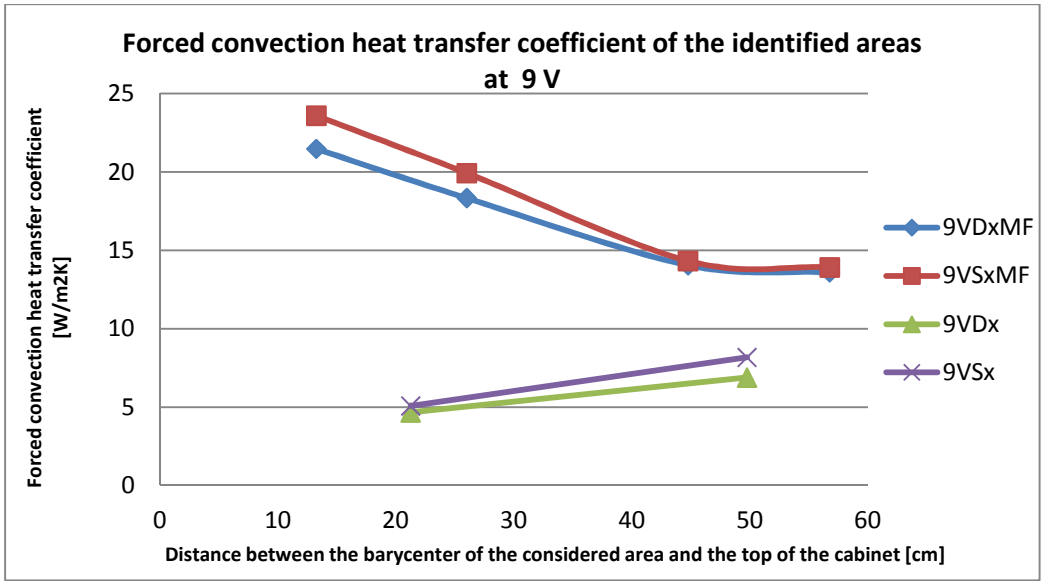

Figure 4.25 Computed heat transfer coefficient for the areas identified in Fig. 4.23.

As we can see in Fig. 4.25 the heat transfer coefficient follows the air speed trend. So, for example, we have the highest the heat transfer coefficient in the first area of the main flow near the exit of the fan. We can also notice the heat transfer coefficients in the areas that are not placed in the main flow assume non negligible values. While in the upper zones the heat transfer coefficient is only slightly more than the one related to the natural convection, in the lower areas the coefficient increases reaching the double or the triple of the natural convection one.

Finally we compute the heat transfer improvements in the same manner of section 4.4.1. We show the results in Tab. 4.7.

Table 4.7 Computed heat transfer results for the tangential fan at four different voltages.

Fan Voltage [V]	Heat exchanged in the examined conditions [W]	Heat exchange increase from the baseline [%]
9	68	40
10	71	48
12.5	75	55
15	79	62

While the centrifugal fan needs 2.565 W and a properly designed multiflow to increase the heat transfer of 39 %, the tangential fan can easily reach an increment of 40 % of the heat transfer running at the lowest voltage with only 0.81 W of power consumption. Once again, the computed results prove the validity of this typology of fan for our application.

Moreover we try to design a multiflow to increase the heat transfer performances given by the tangential fan. In Fig. 4.26 we display the results of this effort marking in blue the measure points and the areas to compute the heat transfer improvement in this configuration.

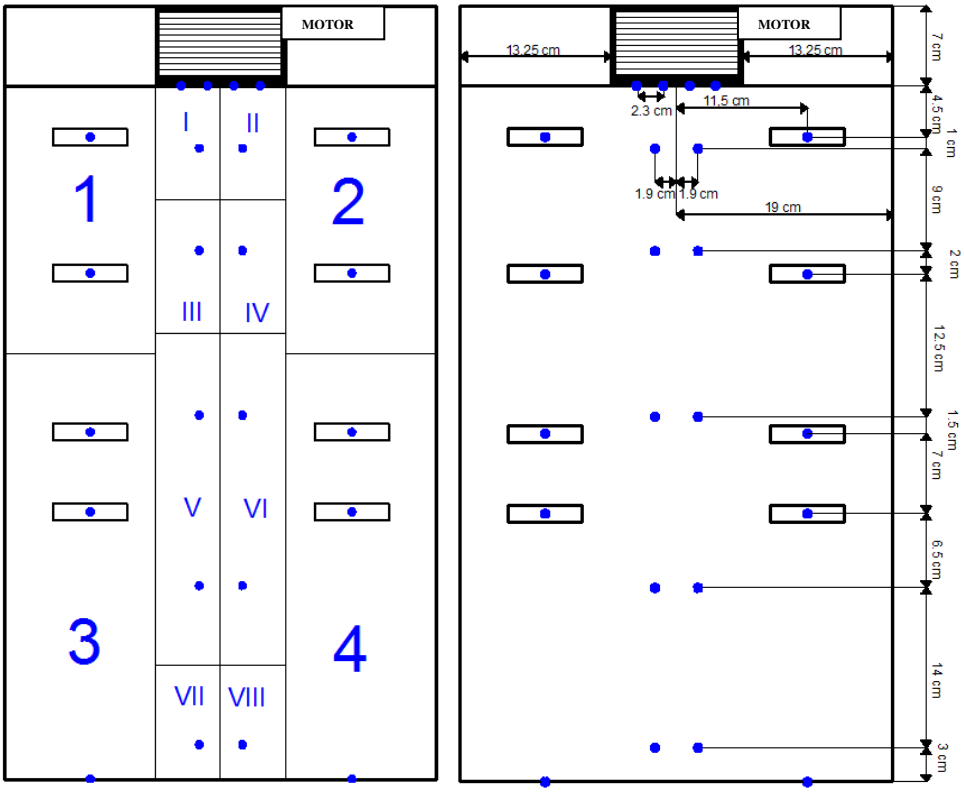

Figure 4.26 Measure points of the air speed using the tangential fan and the designed multiflow.

The multiflow has a thickness of 1 cm. As we can see in Fig. 4.26 we decide to create some frontal openings in the areas that are not directly influenced by the main flow produced by the fan. This multiflow relies on the same principles of the designed one for the centrifugal fan shown in Fig. 4.20. We believe that the frontal openings could let the external air in the cabinet to be dragged from the internal air in the multiflow. In this case we would have an higher increase in the heat transfer than the normal configuration with only the tangential fan without the multiflow. For example, in Fig. 4.27 we display the measured air speeds for the different points with a supply voltage equal to 9 V.

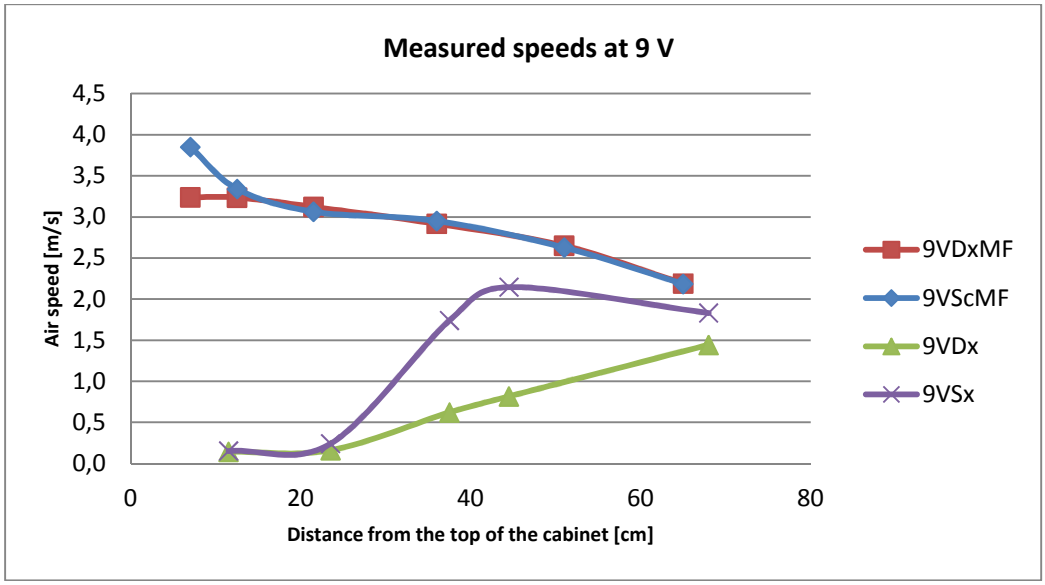

Figure 4.27 Measured air speeds in the different selected points at 9 V for the tangential fan with the designed multiflow.

The nomenclature of the speed trends is the same of Fig. 4.24. From the picture we can conclude that all the speed trends assume higher values than the ones of the configuration with only the tangential fan. On the one hand the internal air manages to drag some external air through the frontal openings in areas 3 and 4. On the other hand the adoption of the multiflow allows us to use all the flow rate given by the blower to increase the heat transfer. In fact we canalize all the blown air inside the multiflow without spreading it on the shelves. In Fig. 4.28 we show the computed heat transfer coefficient for every area identified in Fig. 4.26.

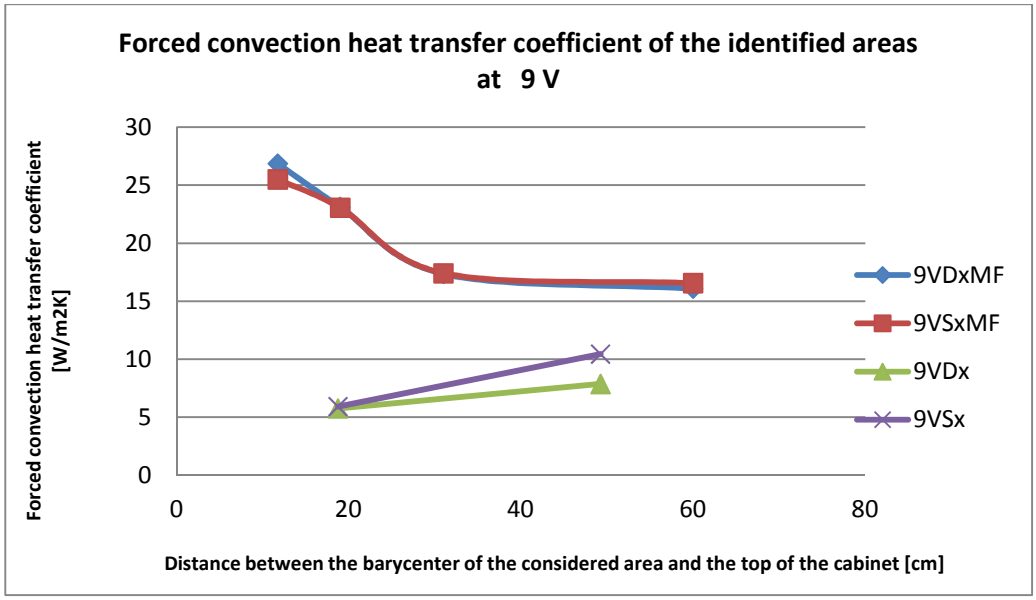

Figure 4.28 Computed heat transfer coefficient for the areas identified in Fig. 4.26.

In Fig. 4.28 we can see that the multiflow allows us use the whole air flow blown by the fan and so we can reach higher values of heat transfer coefficients. In fact if we compare Fig. 4.28 and Fig. 4.25 we can notice that in every considered area we have higher values of the forced convection heat transfer coefficient. In particular we manage to raise this parameter also in the zones that are not directly influenced by the main flow. Furthermore we calculate the heat transfer improvements in this configuration. In Tab. 4.8 we show the results of the computations.

Table 4.8 Computed heat transfer results for the tangential fan coupled with the designed multiflow at four different voltages.

Fan Voltage [V]	Heat exchanged in the examined conditions [W]	Heat exchange increase from the baseline [%]
9	73	51
10	77	59
12.5	81	68
15	85	76

As we can see comparing Tab. 4.7 and Tab. 4.8 the adoption of the multiflow has a strong impact on the heat exchange. In fact in this configuration we have an increase of the heat exchange from 10 % to 13% for the four voltages.

4.5 Conclusions

In this chapter we tried to estimate and to increase the heat transfer between the back wall of the cabinet and the internal air. At the beginning we tested the different existing configurations of fans and multiflows. From these measures we designed and tested some new setups using a centrifugal fan that showed a bigger increase in the heat transfer than the standard ones. The results of all these activities are summarized in Tab. 4.9.

Table 4.9 Summary table of various standard and centrifugal fan setups: forced convection heat transfer coefficients calculated from measured air velocity, heat transfer coefficient improvements versus natural convection, air flow rates and fan powers.

	Big propeller	Small propeller	Big + multiflow	BFB10112M 3V+ multiflow	BFB10112M 4.5V+ multiflow	BFB10112M 3V +1st multiflow	BFB10112M 4.5V + 1st multiflow	BFB10112M 3V +2nd multiflow	BFB10112M 4.5V + 2nd multiflow
Forced convection heat transfer coefficient [W/m^2K]	3.17	2.17	3.37	3.50	3.55	4.43	5.18	4.60	5.38
Improvement vs. baseline [%] (h_{nat} = 2.93 W/m^2K; h_{rad} = 4.07 W/m^2K)	13.2	5.15	15.22	16.6	17.1	27.1	36.5	29.2	39
Air flow rate [m^3/h]	8.4	4.6	8.4	22.0	29.2	22.0	29.2	22.0	29.2
Power [W]	2.9	2.8	2.9	1.71	2.565	1.71	2.565	1.71	2.565

As we can see in Tab. 4.9 the adoption of a centrifugal fan and a properly designed multiflow allowed us to reach a maximum improvement of 39 % of the exchanged heat. Since we wanted to have a uniform air flow on the back wall in order to maximize the heat transfer, we decided to test also a tangential fan. The results of this activities are displayed in Tab. 4.10.

Table 4.10 Summary table of various tangential fan setups: forced convection heat transfer coefficients calculated from measured air velocity, heat transfer coefficient improvements versus natural convection, air flow rates and fan powers.

	Tangential Fan 9 V	Tangential Fan 10 V	Tangential Fan 12.5 V	Tangential Fan 15 V	Tangential Fan 9 V + multiflow	Tangential Fan 10 V + multiflow	Tangential Fan 12.5 V + multiflow	Tangential Fan 15 V + multiflow
Forced convection heat transfer coefficient [W/m^2K]	5.9	6.5	7.1	7.6	6.8	7.4	8.0	8.6
Improvement vs. baseline [%] (h_{nat} = 2.93 W/m^2K; h_{rad} = 4.07 W/m^2K)	40	48	55	62	51	59	68	76
Air flow rate [m^3/h]	33.6	38.4	43.8	49.2	33.6	38.4	43.8	49.2
Power [W]	0.81	1.05	1.75	2.7	0.81	1.05	1.75	2.7

As we can see in Tab. 4.10 the tangential fan showed the best performance among the analyzed fans. Using this fan we managed to enhance the heat transfer with very low consumptions. In this case the multiflow played a crucial

role because it allowed all the blown air by the fan to be used for the heat exchange.
In order to facilitate the implementation of the experimental results in the simulation tool we plotted the heat transfer coefficient improvement as a function of fan power and fan volume flow rate. Then we created fits to estimate improvements at different fan speeds which we don't measure. In particular, we noticed that the averaged forced convection heat transfer coefficient ($\overline{h_{\dot{V}_x}}$) is linked with good approximation to the measured flow rate of the fan ($\dot{V}_x$) through the following equation.

$$\overline{h_{\dot{V}_2}} \approx \overline{h_{\dot{V}_1}} * \left(\frac{\dot{V}_2}{\dot{V}_1}\right)^{3/5} \quad (4.17)$$

Basically the averaged forced convection heat transfer coefficient showed a similar trend to the behavior of the local forced convection coefficient for turbulent flow of equation (4.14). Since in equation (4.17) we included also the natural convection using equation (4.16), equation (4.14) and (4.17) showed slightly different exponents. For the standard fans we assumed a linear behavior between the measured points and the origin of the axis. The resulting trend are shown in Fig. 4.29 and 4.30.

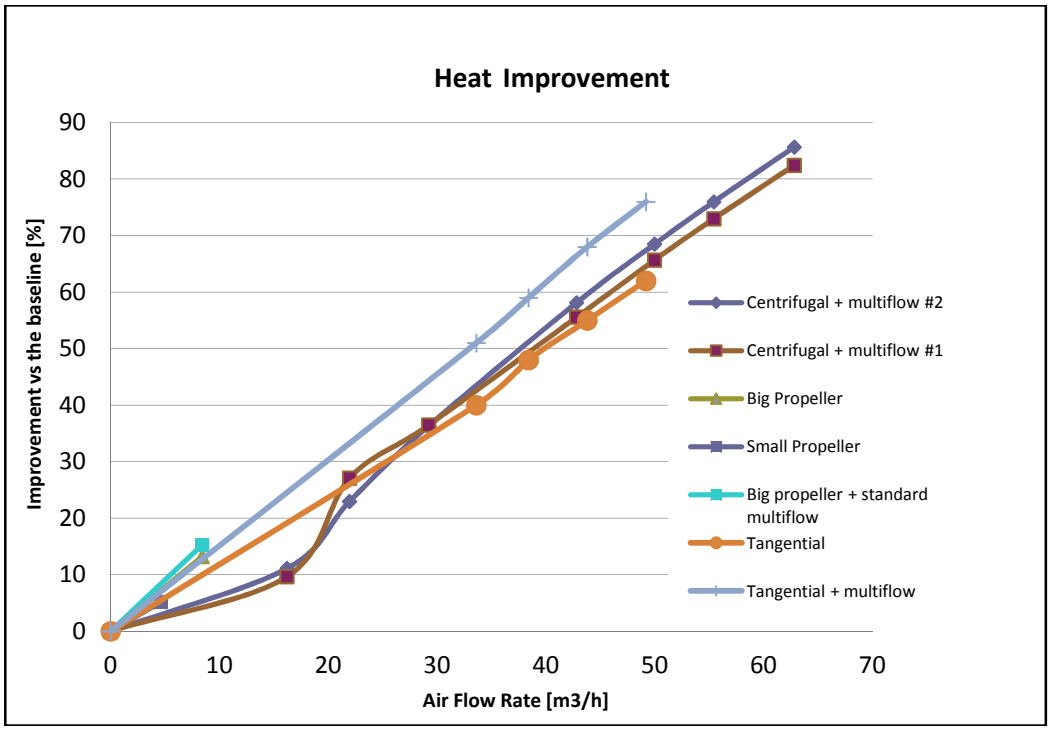

Figure 4.29 Measured and estimated impact of the fan air flow rate on the back wall heat transfer coefficient.

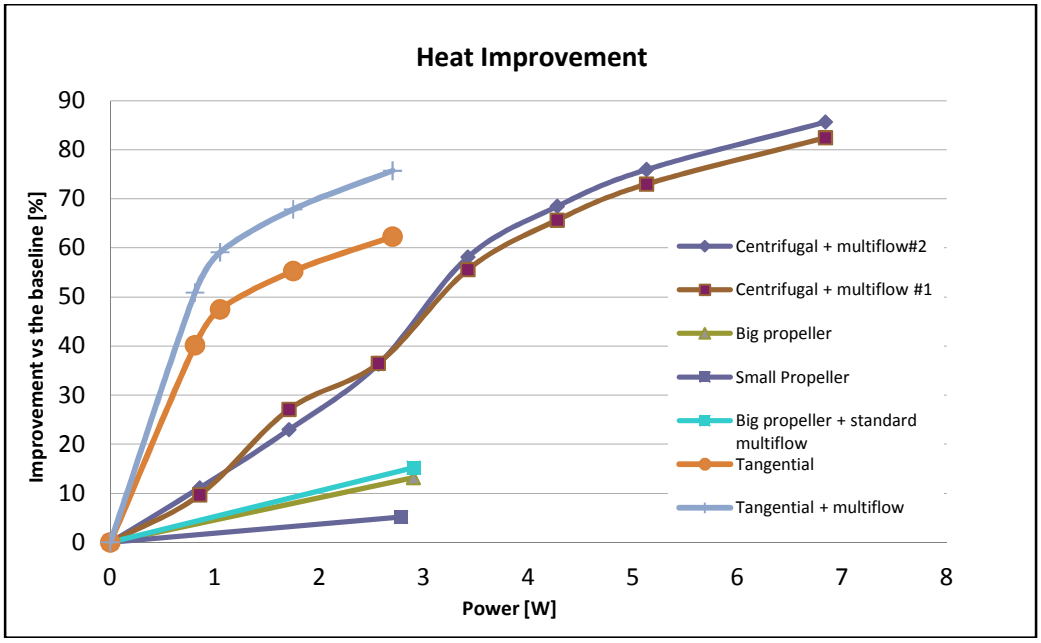

Figure 4.30 Measured and estimated impact of RC fan power on the back wall heat transfer coefficient.

From Fig. 4.29 and Fig. 4.30 we can evince that probably the tangential fan is more efficient at low powers (i.e. low supply voltages). On the one hand, if we install two tangential fans coupled with the multiflow and we run them at the lowest voltage (9 V), we will have a double flow rate (1.120 m^3/min) doubling also the required power (1.62 W). On the other hand, if we want to have the same flow rate using one fan coupled with the multiflow at high voltage, we will probably have a higher required power. In fact from Tab. 4.10, we can see that when the fan blows at the maximum power (2.7 W / 15V, i.e. more than 3 times the power at the lowest voltage) it does not manage to provide neither the double of the flow rate given at the lowest voltage. Since all the blown air is canalized in the multiflow and exploited for the heat exchange, doubling the flow rate we will probably double also the improvement from the baseline in heat exchange. On the one hand, we increase the air speeds on the back wall, on the other hand we enlarge the surfaces where the main flows of the fan directly get in contact with the back wall. The coupling of more than one tangential fan could be a challenge for future improvements. Moreover the experimental activity demonstrated us that air flow in multi-flow structures is a complex phenomenon that should be studied deeply. In particular it is crucial to design an efficient multi-flow structure with uniform air flow distribution. In the future this should be done both with some other experimental campaigns and some strong modeling that involves CFD.

5. Compressor modeling

In order to develop a simple model of a hermetic reciprocating compressor the literature regarding this topic was studied. Different approaches were proposed in the last years to solve the problem. Many review papers have been published to trace the evolution of compressor models during the years. In particular Rasmussen and Jakobsen[10] proposed a method to categorize different compressor models. They divided the available literature on the topic according to the knowledge of the compression process required to run the models. In Fig. 5.1 we can see the categorization made by the authors.

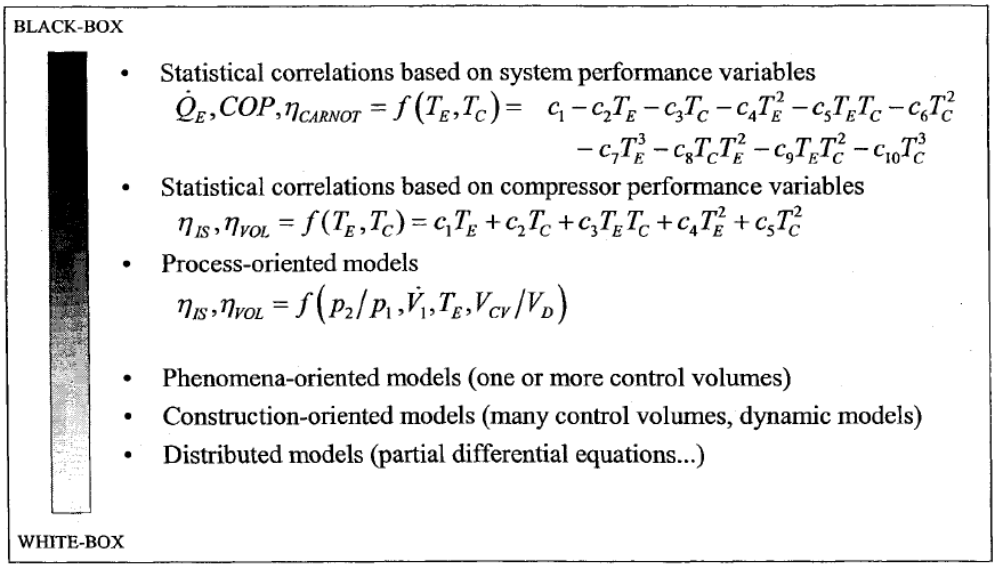

Figure 5.1 Categorization of compressor models according to Rasmussen and Jakobsen [10].

Models that necessitate the lowest level of knowledge are called black-box models and models that need the highest level of knowledge are called white-box models. All the other models are called gray-box models.
The first two categories of the classification of Rasmussen and Jakobsen rely on statistical correlations existing among some basic parameters of the compressor (like the isentropic efficiency) and the evaporation and condensation temperatures. These correlations are polynomial expression with various coefficients that should be determined through an experimental campaign. These models are frequently adopted by the standards (for example the EN12900 standard) to compute the outputs in the test conditions defined by the same norms. These correlations are the basis of the programs for the selection of the right compressor made by the manufacturer.

The third category represents models that schematize the compressor with few geometric parameters like the displacement and the clearance volume ratio. These approaches manage to sum up all the compressor complexity with few basic inputs.
The fourth category gathers all the models that divide the compressor parts according to the different phenomena that happen inside. These approaches split the compressor in different control volumes were both steady state and dynamic models can be implemented. The main phenomena are the compression and the heat exchange to the external ambient. Usually the compression is divided into three parts that represent the pre-compression, the real compression and the post-compression phenomena.
The fifth category adopts a similar approach to the fourth category splitting the compressor in different control volumes. The main difference between the two groups is the criterion for the selection of control volumes. While the fourth category is centered around the different phenomena, the fifth category identifies different control volumes according to the real geometry of the compressor structure. In the models of the fifth category every volume represents a specific component of the compressor.
The last category collects all the models that adopt partial differential equations to predict the behavior of the fluid in every part of the compressor. According to different authors a real white-box model for the whole compressor may never be implemented because of the high complexity of the embedded processes.
In this work two different models were developed.
First we choose to adopt a process oriented model. The main reason for this choice is that this approach is both simple and physically based. We prefer to focus on a process oriented model than on a construction oriented model because in this way we can have a more firm relation between model and physical processes. Moreover process oriented model are usually simpler than construction oriented model, but they have similar accuracy on the predicted result [10]. This model allows us to have first approximated values of three parameters of the compressor: the compressor power, the heat released by the compressor and the temperature of the compressor body. The results of this model do not fit accurately the experimental data (section 6.5.).
So we decided to develop another model in order to have a higher correspondence between model predicted values and experimental data. We choose to implement a model of the sixth category. This model relies on the differential equation of the energy and the mass balance in the compressor chamber. The computational complexity of this second model was rewarded with high accuracy results. Since we didn't know lots of important geometrical parameters of the compressor, we made a sensitivity analysis on these parameters and we took different assumptions to apply the new model. The model has four outputs: the compressor power, the flow rate, the heat released by the compressor and the temperature of the compressor body. All the

predicted values fit with the experimental data in a very accurate way (section 7.4.).

6. Polytrophic model

6.1 Literature on the subject

A survey of the process oriented model was performed and in particular three important papers about the subject were selected.
The first paper of Brok, Touber and Van Der Meer [11] tries to develop a simple model of the compressor based on a simple representation of the compressor in terms of a heat exchanger and a polytrophic compression process. So they divide their work in analyzing these two subsections. On the one hand the authors adopt the correlation of Adair, Qvale and Pearson [12] in a modified form to simulate the heat exchange in the cylinder. On the other hand the scientists try to individuate the right exponent of the polytrophic transformation to describe the compression process.
The conclusions of the paper are very different for the two subsections.
Authors are very doubtful that the introduction of heat transfer equations in compressor models can have a strong impact on improving the performance of compressors. The uncertainty about the cylinder heat transfer coefficient is very high. For this reason the results about heat transfer coefficient cannot be considered valid.
Regarding the polytrophic schematization of the compression experimental results are very different. Authors manage to have significant outputs that verify the model. Through calculations for different fluids they compute exponent of the polytrophic process to obtain the work of the compression process. These results should be confirmed with experimental measures.
Another important study of compressor model was made by Cavallini et al. [13] in 1996. The authors divide the compressor in six different parts (suction muffler, suction chamber, compression cylinder, discharge chamber, discharge line, compressor shell). We show the compressor schematization made by the authors in Fig. 6.1.

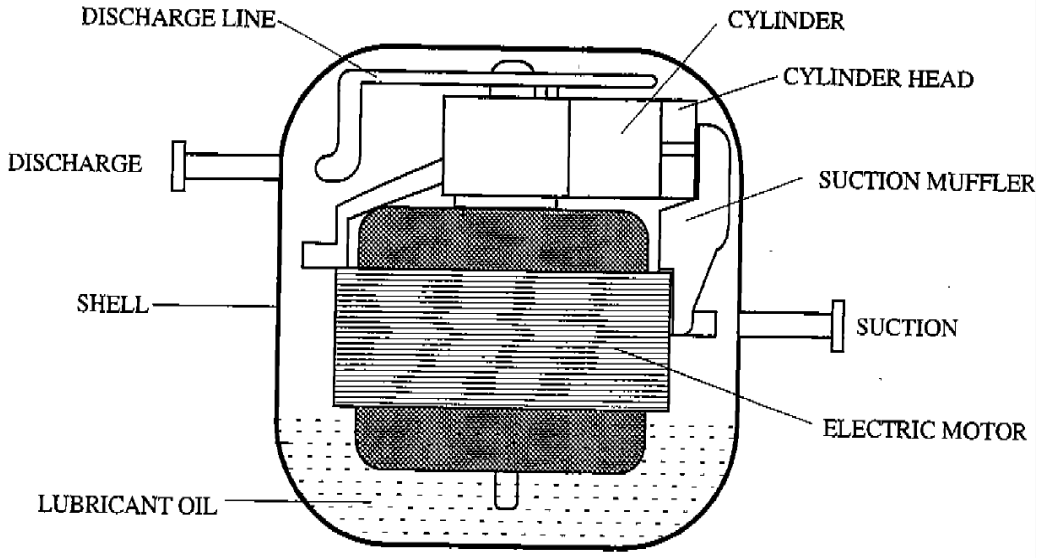

Figure 6.1 Compressor schematization according to Cavallini et al.[13]

For every part they apply a stationary energy balance to compute the thermodynamic properties. They schematize the heat transfer in every part using different correlations for convective and radiative heat exchange. They develop a simulation code with an iterative structure. They provide the input values in terms of thermodynamic properties that describe boundary conditions and geometric parameters of the compressor to obtain the thermodynamic properties in every section of the compressor. In particular three inputs should be provided to the model: the volumetric efficiency of the compressor, the polytrophic index of the compression and the fresh gas fraction in every cycle. These inputs require several parameters to be calculated. The outputs of the simulation are in agreement with experimental measurements. This model predict in an accurate manner both the electric power input and the refrigerant mass flow rate through the compressor. On the one hand the model manages to forecast important parameters of the compressor, on the other hand it needs lots of inputs that are not often available.

The third important paper about the topic was made by Cavallini et al.[14] in 1998. In this study the polytrophic approach of the compression is substituted by an unsteady state analysis of the compressor cycle. Authors apply the general form of the energy balance to study the compression process. The heat transfer in the cylinder is calculated with a correlation proposed by Todescat [15] that relies on a previous analysis of Annand[16]. The simulation code has the same inputs of the previous stationary study by the same authors, but it gives some additional outputs. In fact this model provides also the behaviors of characteristic parameters (such as work, flow rate and flow rate leakage) during

the compressor cycle. The results of the model are in fair agreement with experimental measures. On the one hand this model allows to have the dynamic trend of the predicted outputs that we cannot have with the stationary approach, on the other hand the model is less precise than the stationary one in predicting some important parameters such as the electric power input and the refrigerant mass flow rate through the compressor. Since we want to develop a model of the compressor that is useful to predict improvement in reducing power input, we should adopt a steady state approach in our analysis in order to compute the power input with an higher precision.

6.2 Theoretical model

In order to develop a model of the compressor we divide the analysis in two sections: compression and heat transfer. We adopt a polytrophic model for the compression and a natural convection model for the heat transfer. Fig. 6.2 schematize our compressor model.

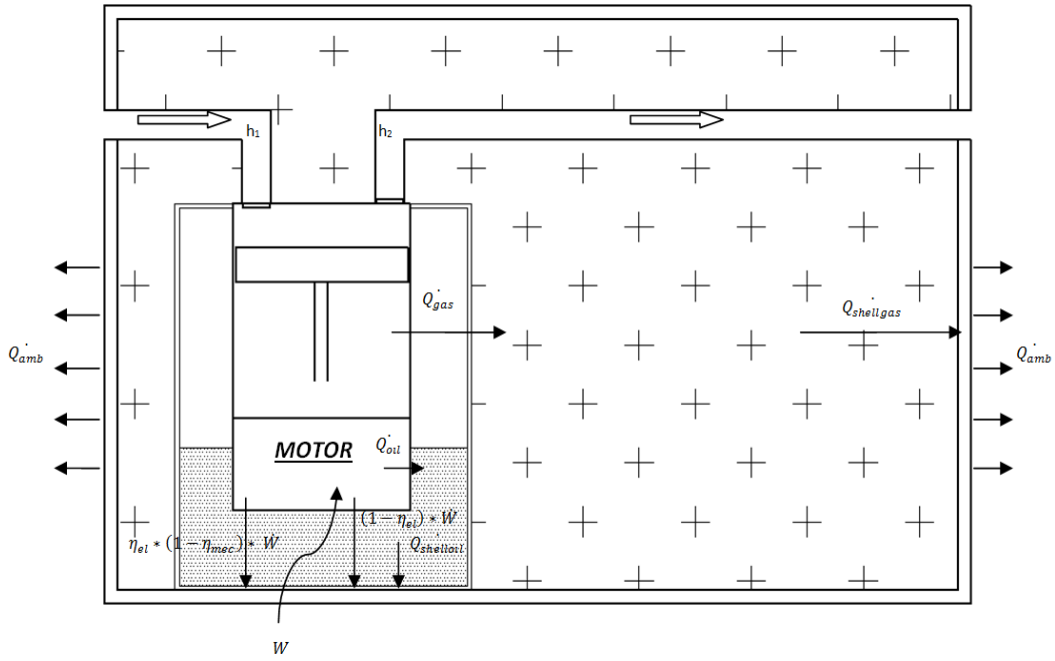

Figure 6.2 Representation of the polytrophic compressor model.

6.2.1 Compressor power

The objective in the first section is the calculation of the power required by the compression process. In the first part we will follow the approach developed by Brok, Touber and Van der Meer[11].

For this model we make the hypothesis that the gas during the compression process behaves as an ideal gas.
First we apply a steady state energy balance to the compressor.

$$w = h_2 - h_1 + q \quad (6.1)$$

with

$$w = c_P * (T_2 - T_1) \quad (6.2)$$

In particular in the adiabatic case we do not have any exchange of heat ($q = 0$). In this case pressures and temperatures during the compression process obey the following law:

$$p^{(1-\gamma)} * T^{\gamma} = constant \quad (6.3)$$

where

$$\gamma = \frac{c_P}{c_V} \quad (6.4)$$

Using the relation between temperature and pressure for an adiabatic process we can compute the specific work as follows:

$$T_2 = T_1 * \left(\frac{p_2}{p_1}\right)^{\frac{\gamma-1}{\gamma}} \quad (6.5)$$

$$w_{adiab} = c_P * T_1 \left[\left(\frac{p_2}{p_1}\right)^{\frac{\gamma-1}{\gamma}} - 1\right] = c_P * T_1[\beta^K - 1] \quad (6.6)$$

where

$$\beta = \left(\frac{p_2}{p_1}\right) and\ K = \frac{\gamma - 1}{\gamma} \quad (6.7)$$

The adiabatic work represents the theoretical limit that we can reach with an ideal polytrophic process. In fact in this case we do not have any irreversible losses represented by the heat exchange that takes place in the real compression process.
In order to schematize the compression process we adopt a general expression of a polytrophic transformation.

$$p * v^n = constant \quad (6.8)$$

The exponent n should be determined with experimental measurements. It varies from 1 (isothermal operation) to γ (adiabatic operation).
We can now compute the real specific work of the polytrophic process with the following formula:

$$w_{pol} = \int_1^2 \left(\frac{1}{\rho}\right) dp = \int_1^2 v_1 * \left(\frac{p_2}{p_1}\right)^{\frac{1}{n}} dp =$$
$$= R * T_1 * \left(\frac{n}{n-1}\right) * \left[\left(\frac{p_2}{p_1}\right)^{\frac{n-1}{n}} - 1\right] \quad (6.9)$$

We can make the hypothesis of perfect gas behavior and we can write the Mayer's relation.

$$R = c_P - c_V = c_P * \frac{\gamma - 1}{\gamma} \quad (6.10)$$

In order to verify this last hypothesis we compute the ideal gas constant using the real values taken from the dedicated software REFPROP 8 of c_P and c_V through eq. (6.10) in different operating conditions of our compressor. Then we compare these values with the ideal value of R* for isobutene considering the molar mass of isobutene equal to 58.12 g/mol. In particular we display the averaged values of c_P and c_V between the saturated vapor point at the evaporation temperature and the relative final point of an isentropic compression at the condensation pressure. The results are shown in the Fig. 6.3.

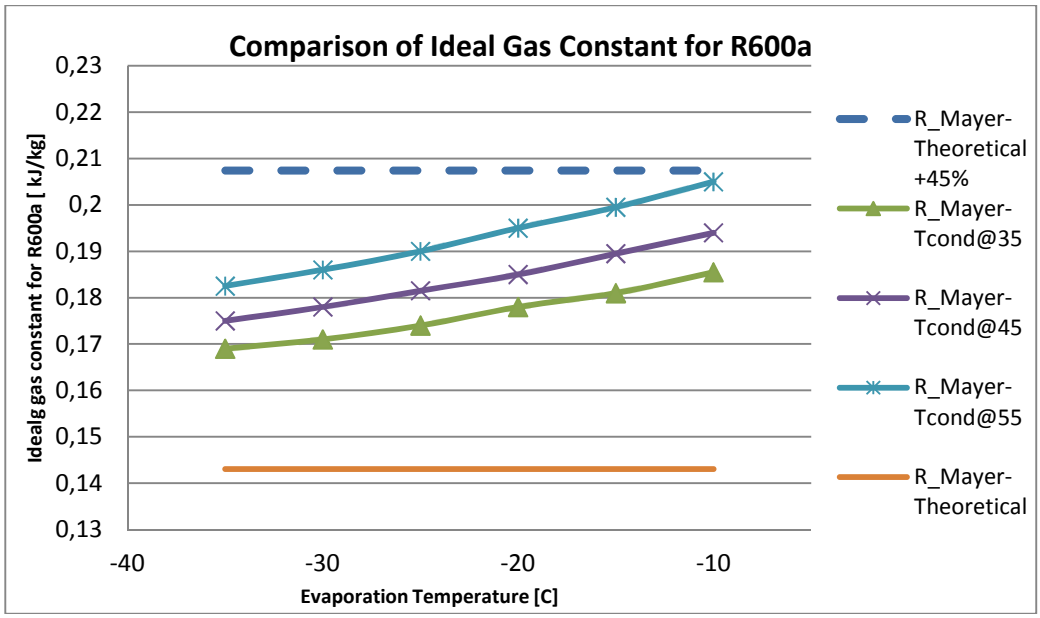

Figure 6.3 Comparison of ideal gas constant for isobutene using Mayer's equation.

As we can see from Fig 6.3 the ideal gas approximation is not so accurate in the range of temperature and pressure where our compressor works. Anyway, as others scholars already did, we will consider the averaged values of c_P and

c_V between the initial and the final point of the isentropic compression as the representative values of these parameters during the real compression process. We can now introduce the new parameter N and with some substitutions we obtain a clearer expression of the polytrophic specific work.

$$N = \frac{n-1}{n} \quad (6.11)$$

$$w_{pol} = c_P * \frac{K}{N} * T_1 * (\beta^N - 1) \quad (6.12)$$

Using the polytrophic equation and combining it with the First Law of Thermodynamic we can express the temperature at the end of the polytrophic process.

$$T_1 = T_2 * \left(\frac{p_2}{p_1}\right)^{\frac{-(n-1)}{n}} = T_2 * \beta^{-N} \quad (6.13)$$

$$c_P * \frac{K}{N} * T_2 * \beta^{-N} * (\beta^N - 1) = c_P * (T_2 - T_1) \quad (6.14)$$

$$T_2 = T_1 * \beta^N * \left[\beta^N - \frac{K}{N} * (\beta^N - 1)\right]^{-1} \quad (6.15)$$

We can now define the difference between the compressor ideal and real work related to the heat transfer occurring in the real polytrophic compression process in the following manner:

$$\eta_{adiab} = \frac{w_{adiab}}{w_{pol}} = \frac{\beta^K - 1}{\beta^N - 1} * \frac{N}{K} * \left[\beta^N - \frac{K}{N} * (\beta^N - 1)\right] \quad (6.16)$$

This indicator gives us information about the goodness of the compression process. High values of this parameter represent that our real process is very similar to the ideal case of the adiabatic process. The more the indicator decreases the more heat is released during the compression. We can compute the heat released during the compression in the cylinder using applying a stationary energy balance through the following formula:

$$\dot{m} * c_P * (T_2 - T_1) = -\dot{Q_{cyl}} + \dot{W} \quad (6.17)$$

If we substitute equation (6.9) and (6.10) and we use the polytrophic relation between temperature and pressure we obtain the following expression of the heat released by the cylinder during the polytrophic process:

$$\dot{Q_{cyl}} = \dot{m} * \left[\frac{n}{n-1} - \frac{\gamma}{\gamma-1}\right] * R * T_1 * [\beta^N - 1] \quad (6.18)$$

Finally in order to calculate the power input required by the compressor we should also take into account the mechanical and electrical losses. So the power input ($\dot{W}$) can be written according to the following expression:

$$\dot{W} = \dot{m} * c_P * \frac{K}{N} * T_1 * (\beta^N - 1) / (\eta_{el} * \eta_{mec}) \quad (6.19)$$

η_{el} and η_{mec} are the electrical and mechanical efficiencies that account for electric energy transmission losses and friction losses. These two values are usually determined by experimental measures.

6.2.2 Rejected heat and shell temperature

In the second section we want to schematize the heat transfer from the cylinder to the external ambient. In particular $\dot{Q_{cyl}}$ is removed from the cylinder through the compressor body. The compressor body also absorbs the heat released by the motor. The compressor body rejects heat to the lubricant oil, to the recirculated refrigerant gas and directly to the compressor shell. So we simply conclude that the sum of the heat removed from the cylinder ($\dot{Q_{cyl}}$) and the heat generated by the mechanical ($\eta_{el} * (1 - \eta_{mec}) * \dot{W}$) and electrical losses ($(1 - \eta_{el}) * \dot{W}$) is transported to the oil ($\dot{Q_{oil}}$) and to the refrigerant gas inside the compressor shell ($\dot{Q_{gas}}$) . The following formula displays the First law applied to the oil:

$$\dot{Q_{cyl}} + (1 - \eta_{el}) * \dot{W} + \eta_{el} * (1 - \eta_{mec}) * \dot{W} = \dot{Q_{oil}} + \dot{Q_{gas}} \quad (6.20)$$

Then we impose the first principle equations also to the oil. The oil is placed at the bottom side of the compressor and it is moved from the bottom to the cylinder to lubricate it. After the lubrication process the oil is splashed on the internal part of the compressor shield and it falls again in the bottom part of the compressor. Considering the physical characteristics of the oil we decide to write a stationary energy balance of the oil without considering the thermal capacity as Cavallini et al.[13] did. So the absorbed heat of the cylinder ($\dot{Q_{oil}}$) is directly released to the compressor shell ($\dot{Q_{shelloil}}$).

$$\dot{Q_{oil}} = \dot{Q_{shelloil}} \quad (6.21)$$

In this simple model we assumed that the heat of the gas inside the compressor shell is directly dissipated through the compressor wall to the ambient. We neglect the fact that the recirculated gas inside the compressor shell on the one hand is heated by the compressor body ($\dot{Q_{gas}}$), on the other hand it is cooled

both by the injection of fresh refrigerant and both by the release of heat to the compressor shell ($\dot{Q}_{shellgas}$) . So we can simply write the energy balance according to the following expression:

$$\dot{Q}_{gas} = \dot{Q}_{shellgas} \quad (6.22)$$

Finally we can state the energy balance for the compressor shell. The compressor shell absorbs the heat from the oil ($\dot{Q}_{shelloil}$) and the heat from the recirculated gas ($\dot{Q}_{shellgas}$). On the other hand the compressor shell exchanges power with the ambient through convection ($\dot{Q}_{ambconv}$) and radiation ($\dot{Q}_{ambrad}$).

$$\dot{Q}_{shelloil} + \dot{Q}_{shellgas} = \dot{Q}_{ambconv} + (\dot{Q}_{ambrad} \quad (6.23)$$

Moreover we study the heat transfer from the compressor shell to the ambient. The starting point is the First Law of Thermodynamic applied to the external surface of the compressor. We can write the following equations.

$$\dot{Q}_{ambconv} = h_{conv} * A * (T_s - T_\infty) \quad (6.24)$$
$$\dot{Q}_{ambrad} = h_{rad} * A * (T_s - T_\infty) \quad (6.25)$$

T_s is the temperature of the external surface of the compressor and T_∞ is the temperature of the ambient air. In order to compute the heat transfer coefficients h_{conv} e h_{rad} we try to schematize the heat transfer phenomenon.
In primis, we consider the heat exchange by convection. We make the hypothesis that the heat exchange is mostly driven by natural convection. The correlations that describe this phenomenon rely on four dimensionless numbers such as Grashof (Gr), Prandtl (Pr), Rayleigh (Ra) and Nusselt (Nu). These numbers find their physical basis in the dimensionless form of the general equation written for natural convection cases. We have to evaluate these numbers for every evaluation of the heat transfer coefficient. For our application Grashof is computed through the following formula:

$$Gr = \frac{g * \beta * (T_s - T_\infty) * Dim^3}{\nu^2} \quad (6.26)$$

Where Dim is the equivalent diameter of the sphere that has the same external surface of the compressor shield and β is the coefficient of thermal expansion of the fluid. If we hypothesize (i.e. Boussinesque's hypothesis) that our fluid can be considered an ideal gas with $\rho = \frac{p}{R*T}$, we can compute the coefficient of thermal expansion according to the following expression:

$$\beta = -\frac{1}{\rho} * \left(\frac{\partial \rho}{\partial T}\right)_P \approx \frac{1}{\rho} * \frac{p}{R * T^2} = \frac{1}{T} \quad (6.27)$$

In our application we make the hypothesis of having only natural convection neglecting all the phenomena of forced convection.
For our application we can calculate Rayleigh number by the following formula:

$$Ra = Gr * \mathrm{Pr} = \frac{g * \beta * (T_s - T_\infty) * Dim^3}{\upsilon * \alpha} \quad (6.30)$$

The calculation of Nusselt allows us to compute the heat transfer coefficient.

$$Nu = \frac{h * Dim}{k} \quad (6.31)$$

In the natural convection Nu is generally a function of Ra and Pr. We adopt three different approaches to compute the heat transfer coefficient of the compressor shell. For all the approaches the properties of the air are evaluated at the film temperature. The film temperature is computed through the following expression:

$$T_{film} = \frac{(T_s + T_\infty)}{2} \quad (6.32)$$

In the first approach the shape of our compressor is schematized with a sphere with the same area of the compressor shield. Churchill [9] developed a correlation to compute the averaged heat transfer coefficient on a sphere in case of natural convection.

$$\overline{Nu}_D = 2 + \frac{0.589 * Ra_D^{1/4}}{\left[1 + \left(\frac{0.469}{Pr}\right)^{\frac{9}{16}}\right]^{\frac{4}{9}}} \quad (6.33)$$

In this case the Rayleigh number is evaluated according to the following equation:

$$Ra_D = \frac{g * \beta * (T_s - T_\infty) * D^3}{\upsilon * \alpha} \quad (6.34)$$

The following correlation is recommended for spheres in fluids with $\Pr \geq 0.7$ and $Ra_D \leq 10^{11}$.
When we do not have any convective phenomena ($Ra \rightarrow 0$) the equation gives us the same result of pure conduction ($\overline{Nu} = 2$) between a spherical surface and a stationary infinite medium.
In the second approach we schematize the shape of our compressor as a box made by four vertical equal plates. We assume that the area of the four plates is equal to the external area of the compressor body.
In the case of natural convection on an isothermal vertical surface in a fluid a correlation to compute the average heat transfer coefficient can be obtained solving the boundary layer equations. The final correlation can be written according to the following equation [9]:

$$\overline{Nu}_L = \frac{\bar{h} * L}{k} = \frac{4}{3} * \left(\frac{Gr_L}{4}\right)^{1/4} * g(\Pr) \quad (6.35)$$

with

$$g(\Pr) = \frac{0.75 * \Pr^{\frac{1}{2}}}{\left(0.609 + 1.221 * \Pr^{\frac{1}{2}} + 1.238 * \Pr\right)^{1/4}} \quad (6.36)$$

The Grashof number is computed according to the following expression:

$$Gr_L = \frac{g * \beta * (T_s - T_\infty) * L^3}{\nu^2} \quad (6.37)$$

Churchill and Chu [9] also proposed the following correlation that can be applied in the entire range of Ra_L to compute the heat transfer coefficient of an immersed vertical plate.

$$\overline{Nu}_L = \left\{ 0.825 + \frac{0.387 * Ra_L^{\frac{1}{6}}}{\left[1 + \left(\frac{0.492}{Pr}\right)^{\frac{9}{16}}\right]^{\frac{8}{27}}} \right\}^2 \quad (6.38)$$

If we want to calculate in a more accurate manner the heat transfer coefficient in the case of laminar flow ($Ra_L < 10^9$) we can also adopt the following correlation:

$$\overline{Nu}_L = 0.68 + \frac{0.670 * Ra_L^{\frac{1}{4}}}{\left[1 + \left(\frac{0.492}{Pr}\right)^{\frac{9}{16}}\right]^{\frac{4}{9}}} \quad (6.39)$$

In the third approach we schematize the shape of our compressor with a cylinder with the same area of the compressor shield. Churchill and Chu [9] developed a correlation to compute the average heat transfer coefficient of the cylinder surface. So we use the following correlation that is valid for $Ra_D < 10^{12}$.

$$\overline{Nu}_D = \left\{0.60 + \frac{0.387 * Ra_D^{\frac{1}{6}}}{\left[1 + \left(\frac{0.559}{Pr}\right)^{\frac{9}{16}}\right]^{\frac{8}{27}}}\right\}^2 \quad (6.40)$$

We also compare the result of Churchill and Chu formula with the outputs of Morgan's correlation [9] for isothermal cylinder. In fact Morgan developed a correlation that is valid $10^2 < Ra_D < 10^4$ for following correlation to calculate the heat transfer coefficient.

$$\overline{Nu}_D = 0.85 * Ra_D^{0.188} \quad (6.41)$$

Finally we also take into account the radiative heat transfer coefficient related to the emission by the surfaces that we use to schematize the compressor shield. We simply calculate the radiative heat transfer coefficient of each surface with the following equation:

$$h_{rad} = \varepsilon * \sigma * (T_s + T_\infty) * (T_s^2 + T_\infty^2) \quad (6.42)$$

In eq. (6.42) we assume a value of 0.9 for the emissivity ε.

6.3 Data processing

In this section we have two different objectives. Firstly we want to gather the required input values to apply our model, secondly from the datasheet we can extrapolate some experimental results to test the predictions of the model.
In particular we want to apply our model to VEMC9C Embraco compressor. This compressor is the one installed on the available prototype. In Fig. 6.4 we can see a sketch of the VEMC9C Embraco compressor with some relevant geometrical parameters.

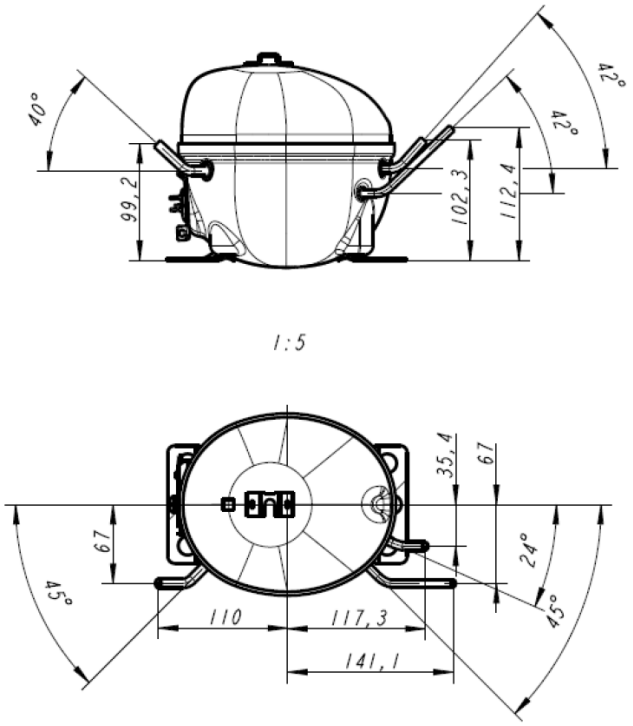

Figure 6.4 Sketch of the VEMC9C Embraco hermetic reciprocal compressor (dimensions are expressed in mm).

Furthermore in the datasheet we have some others geometrical characteristics of the compressor and the results of performance tests. These tests are made following the EN 12900 standard for refrigerant compressor. This standard defines a standard set of conditions to check the performance of refrigeration compressors. The specific testing conditions, usually called the Low Back Pressure conditions (LBP), are the following:
Ambient temperature (T_{amb} = 32.2 °C)
Refrigerant evaporation temperature (T_{evap}= -35, -30, 35, -23.3, -20, -15 and -10 °C)
Refrigerant condensation temperature (T_{cond} = 35, 45, 55 and 65 °C)
Refrigerant temperature at compressor inlet ($T_{supeheating}$ = 32.2°C)
Refrigerant temperature at condenser outlet ($T_{subcooling}$ = 32.2°C)

Installing the compressor in the standard LBP cycle, the compressor manufacturer shows performance results in terms of Cooling Capacity (CAP), input power and efficiency (COP). This last indicator corresponds to the ratio between cooling capacity and input power. Embraco displays values of these three parameters for different compressor conditions. Conditions can vary

according to three parameters: compressor speed (rpm), evaporation temperature and condensation temperature.
Embraco VEMC9C is a variable speed compressor. Speed varies according to an external frequency modulator in the range from 1200 RPM to 4500 RPM.
From the datasheet we can obtain three important parameters for the compressor: volumetric efficiency, isentropic efficiency and exergetic efficiency. The first one is an input value required by our model and the other ones can be considered experimental results to test our model forecasts.
In primis, we can obtain the volumetric efficiency from the cooling capacity in the datasheet. Volumetric efficiency is defined as the ratio of the volume of gas drawn into the piston to the swept volume of the cylinder. Normally in the definition it is assumed that the refrigerant gas enters the cylinder at the compressor suction temperature. In other words it is neglected the heat exchanges that takes place in the suction chamber. Volumetric efficiency is a very important parameter of the compressor that the manufacturer allows us to compute using the datasheet.
We can write cooling capacity as the multiplication of refrigerant mass flow by enthalpy difference of exiting and entering refrigerant flow to the evaporator. So we express CAP according to the following formula:

$$\dot{Q} = \dot{m} * \left(h_{suction} - h_{inevap}\right) \quad (6.43)$$

Since our machine is an hermetic reciprocating compressor, we can express the refrigerant mass flow through the following formula:

$$\dot{m} = \rho_{suction} * V_{cyl} * N_{cyl} * \vartheta_{vol} * \frac{rpm}{60} \quad (6.44)$$

Our compressor is a single cylinder compressor with a displacement of 9.05 cm^3. Moreover we tried to understand which parameter of equation (6.44) has a relevant impact on the flow rate. In Fig. 6.5 we plot the flow rate for different conditions of suction pressure and temperature.

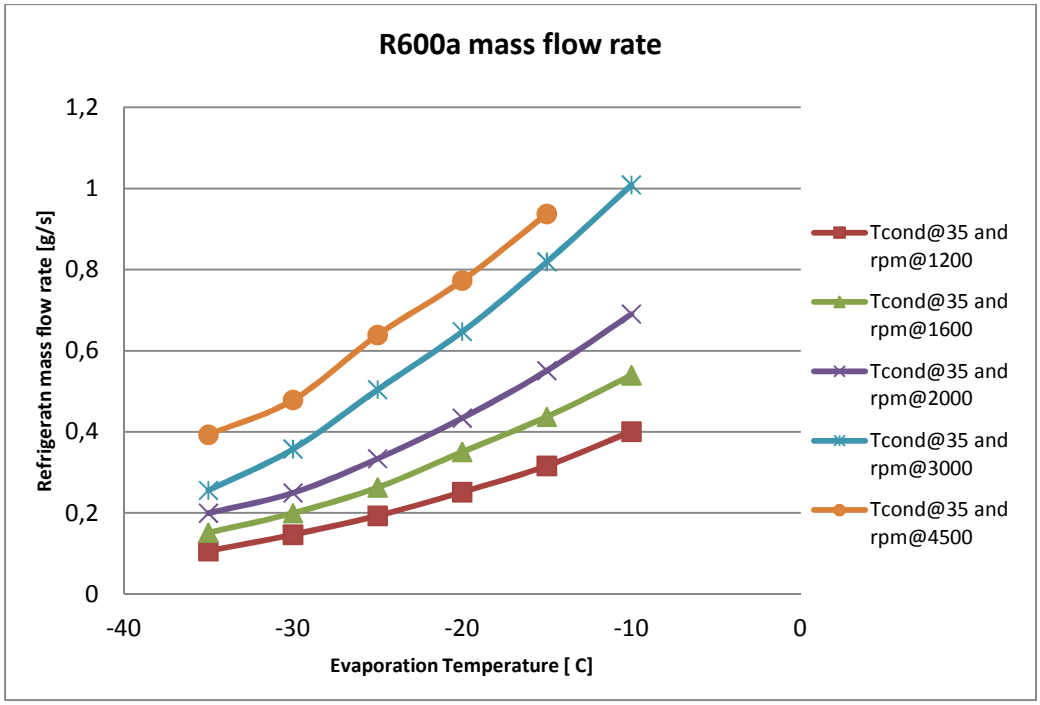

Figure 6.5 Refrigerant mass flow rate as a function of evaporation temperature and compressor speed.

From Fig. 6.5 we can see that the refrigerant mass flow shows a strong dependence on suction pressure (determined by evaporation temperature) and a weak dependence on suction temperature. The more the evaporation temperature is higher, the more refrigerant mass flow the compressor elaborates. To understand the reasons behind this behavior we analyze the two variable parameters in equations (6.44): suction density and volumetric efficiency.
As for all the others thermo physical properties of the fluid, we determine the suction density using the dedicated software REFPROP 8. In Fig. 6.6 we display suction density for different evaporation temperatures, i.e. suction pressures, and suction temperature.

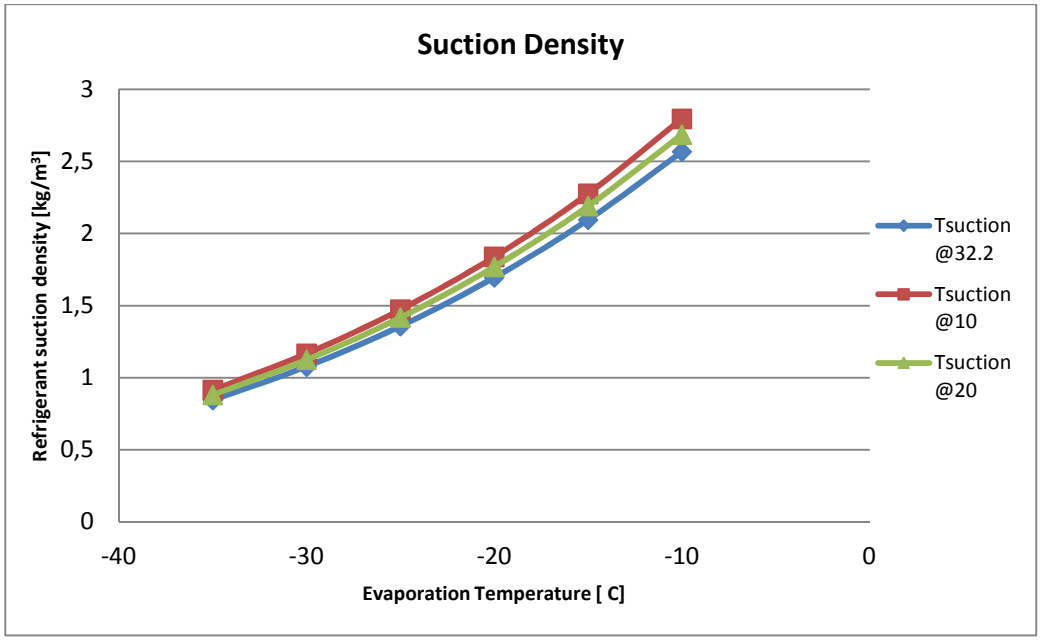

Figure 6.6 R600a suction density as a function of evaporation and suction temperatures.

We can see that for R600a only the evaporation temperature has a strong influence on the behavior of the density. In fact the suction temperature does not affect relevantly the density. When the evaporation temperature rises, the suction density increases too.
In Fig. 6.7 we show the trend extrapolated from the experimental values of the datasheet of the volumetric efficiency varying evaporation temperature.

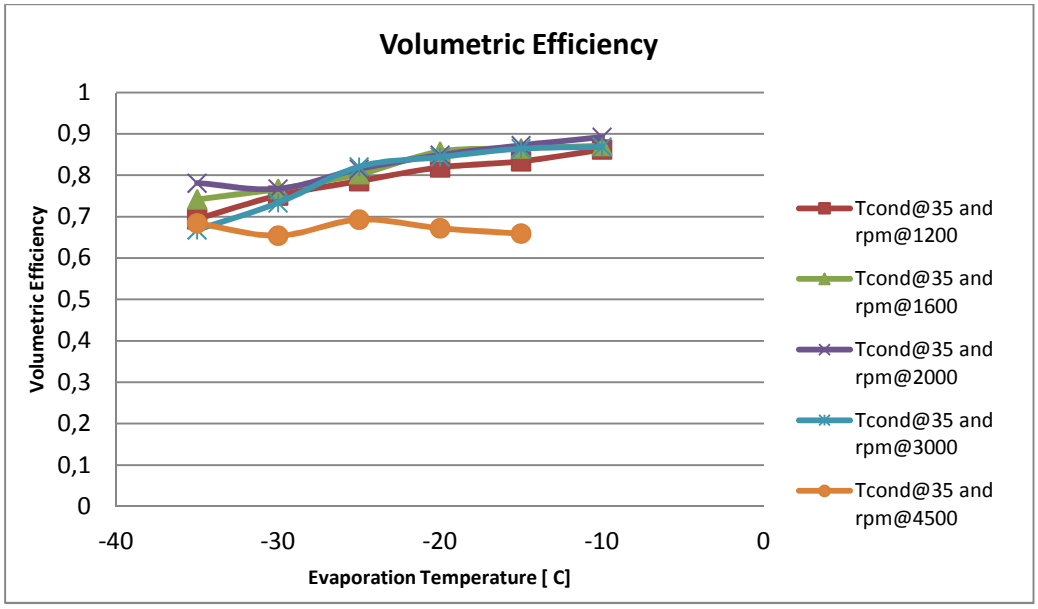

Figure 6.7 Volumetric efficiency as a function of evaporation temperature and compressor speed.

For every compressor speed we have an improvement of the volumetric efficiency when evaporation temperature rises.
Comparing the trends of the suction density and the volumetric efficiency we can state that the main driver of growth of the refrigerant mass flow can be individuated in the increase of the density.
Considering equations (6.43) and (6.44) we can finally obtain the volumetric efficiency. Knowing the trends of this parameter is the first step to estimate the energy performances of the compressor.
Secondly, we can compute the isentropic efficiency according to the following formula:

$$\eta_{iso} = \frac{\left(h_{outcompISO} - h_{suction}\right)}{\left(h_{outcomp} - h_{suction}\right)} \qquad (6.45)$$

This parameter represents the energy efficiency of the compressor. The more the parameter increases, the less irreversibility processes take place in the compression. These losses usually happen because of internal frictions, valving system of the compressor, heat exchanges and other peculiar phenomena of the compression. Fig. 6.8 shows the trends of isentropic efficiency for different condensations temperatures versus pressure ratio.

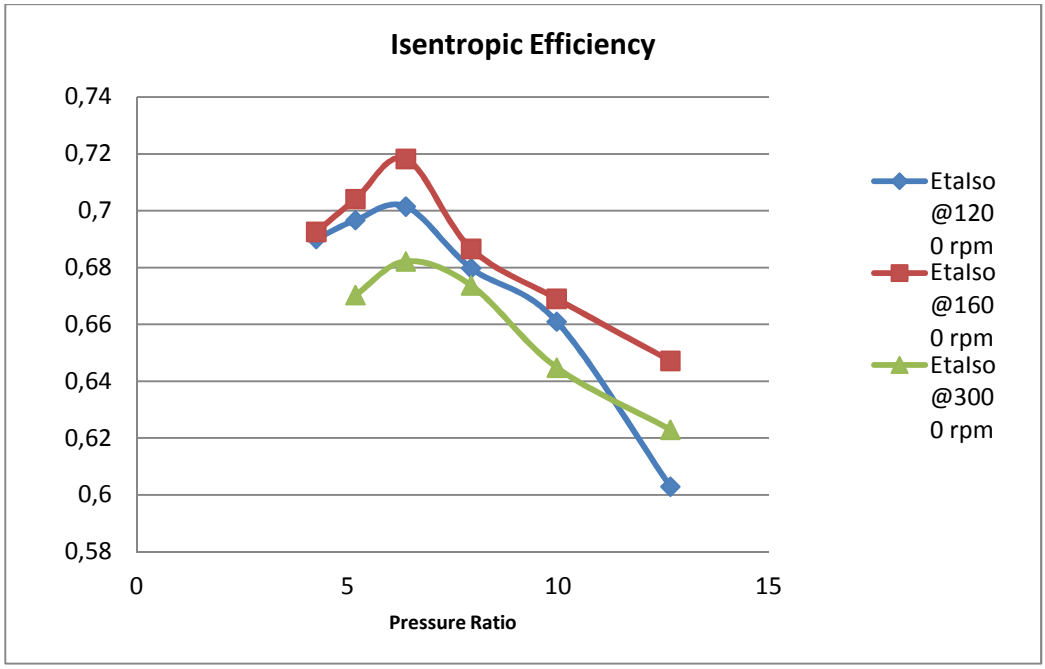

Figure 6.8 Isentropic efficiency as a function of the pressure ratio and the compressor speed.

As we can see in Fig. 6.8, we can identify a pressure ratio where the compressor has the best performances. The refrigeration cycle should be designed to have a similar pressure ratio. Usually we have fixed evaporation and condensation temperatures (and so also a fixed pressure ratio) and we select the compressor that demonstrates the best isentropic efficiency for that pressure ratio.
Moreover from the value of the isentropic efficiency we can also compute the COP of the cycle according to the following equation:

$$COP = \eta_{iso} * \frac{h_{suction} - h_{inevap}}{(h_{outcompISO} - h_{suction})} \qquad (6.46)$$

COP is the parameter that we should maximize choosing the right compressor and the appropriate refrigeration cycle. For example, in sequential dual evaporator system we use only one compressor for both refrigerator and freezer. Since we have two different evaporation temperatures for the two compartments, we should select a compressor that is a good compromise for the performances at the two different pressure ratios. So in order to select the right compressor we will focus our attention on the maximization of the COP.
Lastly we can compute the exergetic efficiency according to the following formula reported by Galliani and Pedrocchi [17]:

$$\eta_{ex} = \frac{(ex_{outcomp} - ex_{suction})}{W} = \frac{[h_{outcomp} - h_{suction} - T_{amb} * (s_{outcomp} - s_{suction})]}{W} \quad (6.47)$$

This parameter expresses the potential of improvement of the compressor in the given working conditions. In fact the exergetic efficiency represents the performances of the compressor linked with the ambient conditions in which it works. This parameter is a fair parameter to compare technologies that work in different ambient conditions.

6.4 Computational scheme

Using Microsoft Excel we simulated the behavior of the compressor with R600a. Input values are related to boundary conditions of the compression and to the peculiar parameters of the compressor. Boundary condition inputs are the following: ambient temperature, suction temperature, suction pressure and discharge pressure. The peculiar parameters of the compressor that are utilized as inputs are the following: volumetric efficiency, mechanical efficiency, electrical efficiency, compressor speed, geometrical data and polytrophic exponent. We assumed that the values of the electrical and the mechanical efficiency are both equal to 0.9.
We found the polytrophic exponent of the compression process minimizing the Average Absolute Deviation between the model predicted values of the compressor power and the experimental values calculated using the datasheet of the compressor.
The value of the polytropic index should be included between 1 (i.e. isothermal compression) and the isentropic compression value ($\gamma = c_P/c_V$). Performing the minimization we obtain a value of the polytropic exponent equal to 1,066054 that lies in the predicted range. After this minimization we obtain a Root Mean Square between the predicted and the experimental values equal to 1.53 %.
Once we know the required inputs, we can compute the compressor power, the rejected heat and the temperature of the compressor body using the formulas reported in section 6.2.

6.5 Results

Since our model predicts only the specific power of the compressor, in order to compare the results of the simulation with the experimental ones we use the values of mass flow rates given by the datasheet to compute the power. Fig 6.9 shows the power simulated by the model compared to the experimental one.

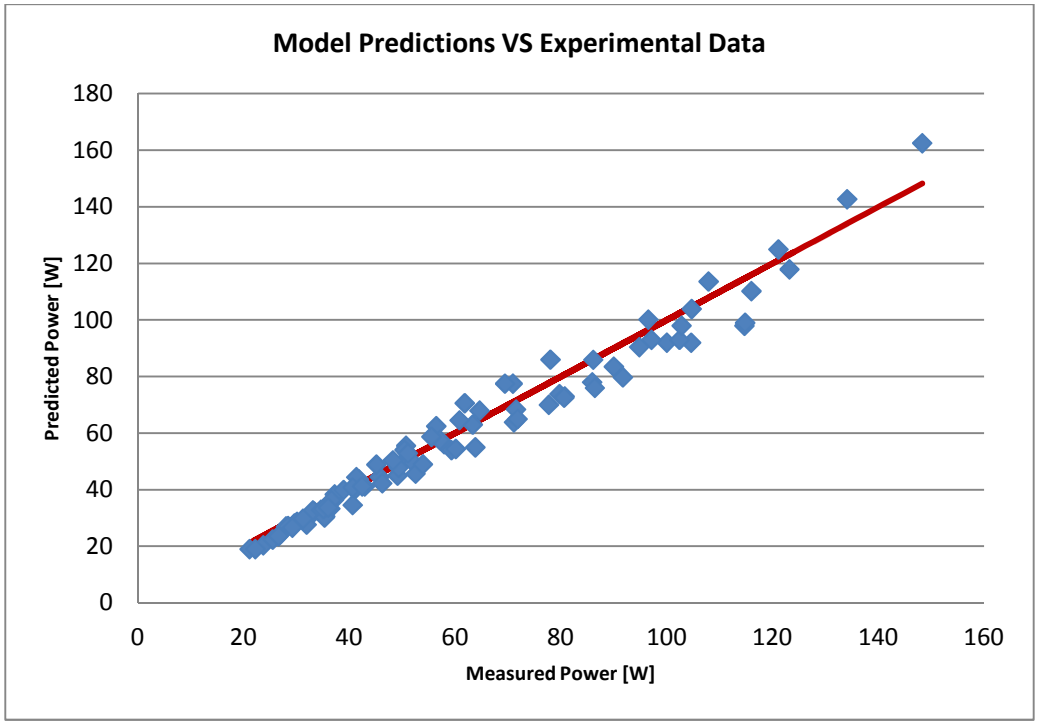

Figure 6.9 Comparison between predicted and experimental values of compressor power.

We can see that the relative error varies between -15% and +14% with an Average Absolute Deviation equal to 7 %. In particular we can notice that the model fits better when we have low values of power. These points correspond to the low values of pressure ratio and in particular to the points with the lowest condensing temperature. This behavior of the model is probably the direct consequence of the ideal gas assumption. In fact, as already shown in Fig. 6.3, the ideal gas approximation fits better for the 35 °C condensing temperature at lower pressure ratios.

Then we also compute the temperature of the compressor body using different correlations. For example, in Fig. 6.10, we show a comparison of the predicted temperatures of the compressor body by the different correlations at maximum rpm with condensing temperature equal to 55 °C and ambient temperature equal to 25 °C.

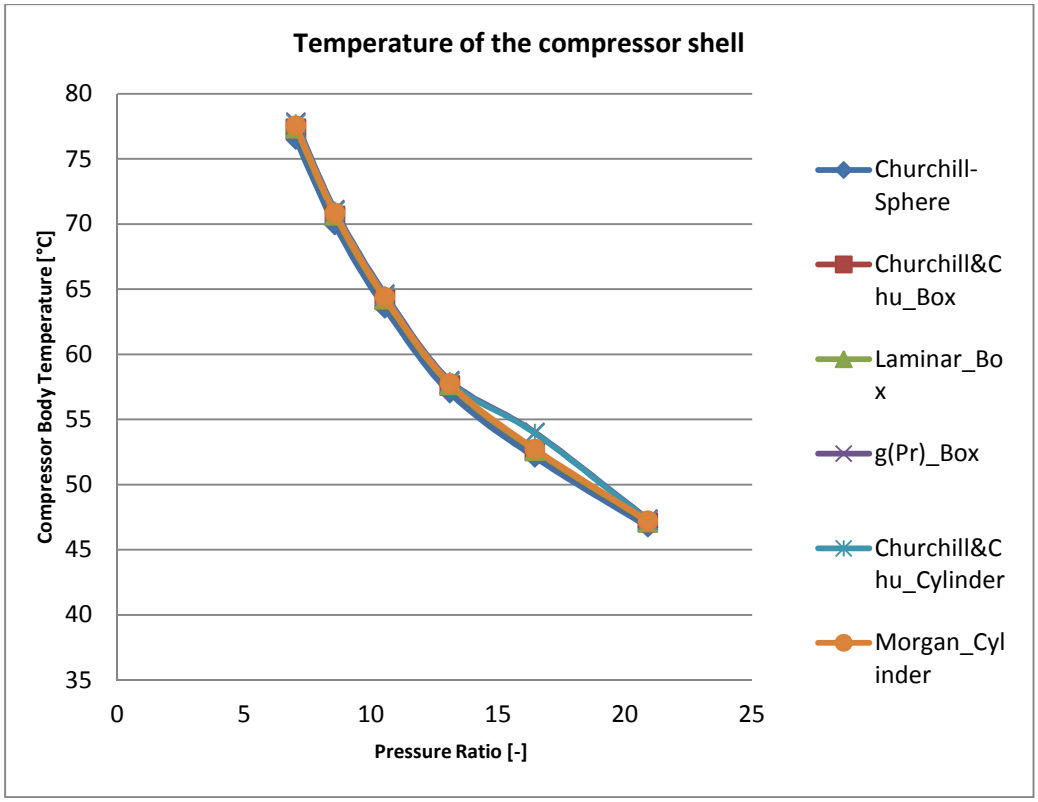

Figure 6.10 Comparison between the predicted temperatures of the compressor shell using different heat transfer correlations at the maximum revolution speed.

From the graph we see that the different approaches predict very similar temperatures of the compressor body. So all the different approaches could be considered as valid for our problem. Moreover if we compare the radiative and the convective fluxes we will discover that the major part of the total heat flux corresponds to the radiative share. For example, in Fig. 6.11, we display the radiative and the convective flux for the case of natural convection on a cylinder using the Morgan correlation.

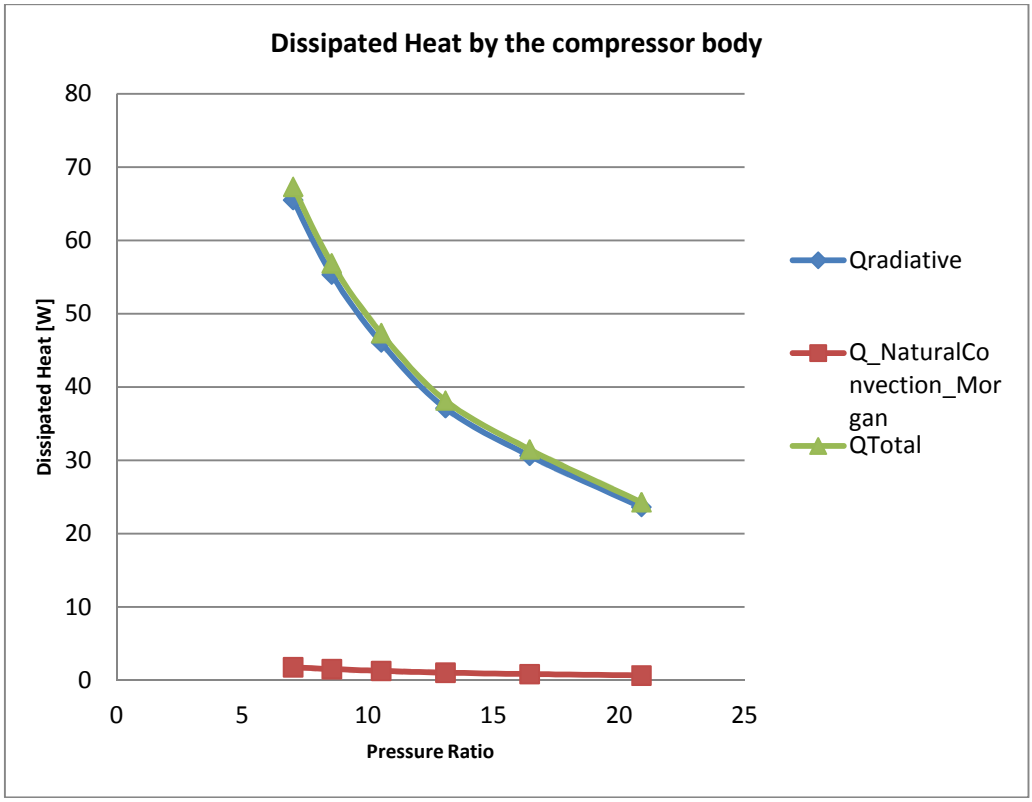

Figure 6.11 Radiative and convective shares in the compressor heat exchange to the external ambient varying the pressure ratio at the maximum revolution speed.

Using the Morgan's approach to estimate the natural convection on the outside of the compressor we obtain that the convective flux correspond to 5-6% of the total heat flux. So it is evident that the radiative phenomena is the most important in the heat dissipation process of the compressor body.

6.6 Conclusions

We developed a polytrophic model to compute the compressor power and the temperature of the compressor shell. This model showed a sufficient agreement with the experimental data for simple calculations in steady state conditions. The model relied on the assumption of considering the isobutene an ideal gas. The isobutene showed a behavior similar to an ideal gas only for small pressure ratios. Since we wanted to predict the compressor power and also the mass flow rate in a more precise and dynamic way, we kept the validity of the polytrophic model only for preliminary calculations and we decided to implement another model of the compressor.

7. Differential model

In order to predict very precisely the compressor power and to compute the mass flow rate, we developed the second model for the VEMC9C compressor. This model relies on the principle of mass and energy conservations. Using some hypothesis, we compute the mass and the energy balance in every instant inside the compressor chamber for an ideal compression and then we move these results to the real ones using some coefficients that represents some physical phenomena that we neglect to solve the differential equations.

7.1 Literature on the subject

We made a survey of the models of the sixth category[10] and we select three crucial papers about the topic.
The first paper of Todescat et al. [15] corresponds to one of the first attempt of solving the differential equation of the energy balance in the reciprocating compressor case. This model represents the archetype of the model of the sixth category. The authors developed different energy balances for every physical part of the compressor and they also performed an overall energy balance on the whole compressor. They adopted stationary energy balances for every part of the compressor except for the compressor chamber. The authors solved the differential equation of the energy balance to compute the temperature of the gas in the cylinder. In every instant the model solved the steady state energy balances to have the required boundary condition values to run the differential model in the compressor cylinder. They considered heat transfer in the balances using both available correlations and experimental measurements. Finally they compared experimental results with values obtained solving the model having a good agreement. So they concluded this kind of models can be really used for design purposes.
Another important contribution to the hermetic compressor modeling was made by Hermes and Melo [18]. They developed a semi empirical model for hermetic reciprocating compressor based on solving the energy balance inside the compressor chamber. Their theoretical model relied on the differential equations of mass and energy balances in the cylinder that was considered a lumped control volume. In particular they solved the equations neglecting both the heat transfer of the cylinder wall, i.e. they considered an adiabatic compression process, and the valve dynamics, i.e. they modeled the valves as two-position components (open or closed). This semi-empirical model took into account the refrigerant leakages and the mechanical losses applying correction coefficients to the predicted values of flow rate and power predicted by the theoretical model. These coefficients were chosen minimizing the absolute relative error

between the model values and the experimental measurements. They also minimized two other coefficients related to the suction and the discharge through the valves to fit better the measured data. They managed to have an agreement within +-10% between the predicted and the real values of both flow rate and compressor power.
The last important study that should be quoted about compressor modeling is a paper made by Winandy et al. [19]. On the one hand the authors performed an experimental campaign to measure different parameters of a reciprocating compressor, on the other hand they created a model to simulate the behavior of the device. They represented all the transformations of the fluid inside the compressor through five separated processes: pressure drop at the entrance, heating up in the suction tube, isentropic compression in the cylinder, cooling down in the discharge tube and pressure drop at the outlet. They schematized the heat exchange processes through the use of the $\epsilon - NTU$ method considering the compressor as an exchanging body with infinite thermal capacity. Moreover they also provided some correction coefficients to take into account the mechanical losses in the compression. In particular they divided these losses in two different terms: one proportional to the isentropic work and the other one related to the revolution speed. At first, they took initial guess values for different parameters of the compressor and they run the model. Then, minimizing the error between predicted values and experimental data, they found the values of the parameters that fitted better their application. The model showed good results both in terms of estimated flow rate and in terms of predicted power. On the one hand, they manage to fit the measurements of flow rate with a relative error of -6% to +6%, on the other hand they forecasted the compressor shaft power with a relative error that varied between -7% and 3%.

7.2 Theoretical model

Let's start from the energy balance in the global form.

$$\frac{dE}{dt} = \sum_{i}^{N} \Phi_{\mathrm{i}}^{\mathrm{ADV(E)}} + \Phi_T + W_{fs} + W_{fm} \qquad (7.1)$$

In Fig. 7.1 we show a schematization of the general configuration of the continuum that we are analyzing.

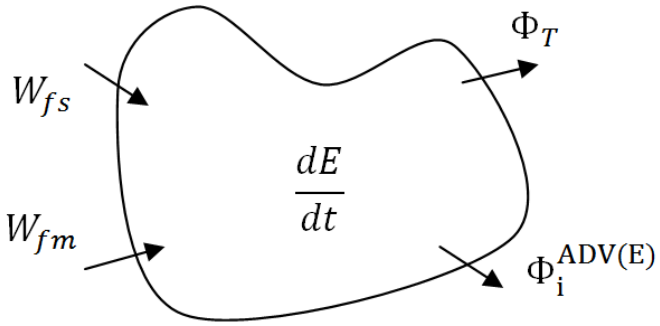

Figure 7.1 Sketch of the general configuration of the continuum.

We can also write the same balance in the differential form as following:

$$\frac{\partial \rho e}{\partial t} + \ div\big((\rho e)\vec{v}\big) + \ div(\overrightarrow{\varphi_T}) - div\big(\bar{\bar{T}}\vec{v}\big) - \rho * \overrightarrow{f_m}\vec{v} = 0 \quad (7.2)$$

We can obtain the equation of balance of mechanical energy multiplying the equation of the conservation of the momentum with $\vec{v}$.

$$\frac{\partial \rho v^2/2}{\partial t} + \ div\big((\rho v^2/2)\vec{v}\big) - \vec{v} div\big(\bar{\bar{T}}\big) - \rho * \overrightarrow{f_m}\vec{v} = 0 \quad (7.3)$$

If we subtract (7.3) to (7.2) we obtain the balance of internal energy.

$$\frac{\partial \rho u}{\partial t} + \ div\big((\rho u)\vec{v}\big) + \ div(\overrightarrow{\varphi_T}) + p div(\vec{v}) - tr(\bar{\bar{D}}\vec{\nabla}\vec{v}) = 0 \quad (7.4)$$

We can also write this balance in the global form as follows:

$$\frac{dU}{dt} = \sum_{i}^{N} \Phi_{\mathrm{i}}^{\mathrm{ADV(U)}} + \Phi_T + W_{revC/E} + \Phi_D \quad (7.5)$$

We now make the hypothesis of neglecting the heat fluxes and the dissipation function inside of the cylinder. Moreover we can now consider the term of the internal energy balance related to the advective flows.

$$\sum_{i}^{N} \Phi_{\mathrm{i}}^{\mathrm{ADV(U)}} = \int_{V_c}^{i} div\big((\rho u)\vec{v}\big) dV = \int_{S_{V_c}}^{i} \rho u \vec{v}\vec{n} dS = < \rho u v_n >_{S_{V_c}} * S_{V_c} \quad (7.6)$$

We now make the hypothesis that the variations of ρu and v_n are not directly related through the following formula:

$$< \rho u v_n >_{S_{V_c}} = < u >_{S_{V_c}} * < \rho v_n >_{S_{V_c}} + \ cov(\rho u \ ; \ v_n)$$
$$\cong < u >_{S_{V_c}} * < \rho v_n >_{S_{V_c}} \quad (7.7)$$

Using the equation of mass conservation we can define the mass flow rate through the following equation:

$$\frac{dM}{dt} = \sum_{i}^{N} \Phi_{\mathrm{i}}^{\mathrm{ADV(M)}} = \int_{S_{V_c}}^{i} \rho \vec{v} \vec{n} dS = \sum_{i}^{N} < \rho v_n >_{S_{V_i}} * S_{V_i} = \sum_{i}^{N} w_i \quad (7.8)$$

We can apply the previous hypothesis to write the advective term of the internal energy conservation equation as follows:

$$\Phi_{\mathrm{i}}^{\mathrm{ADV(U)}} = < \rho u v_n >_{S_{V_c}} * S_{V_c} = < u >_{S_{V_c}} * < \rho v_n >_{S_{V_c}} * S_{V_c} = w * < u >_{S_{V_c}}$$
$$\cong w_i * u_i \quad (7.9)$$

From the classical theory of continuo's kinematics we can have the following equation:

$$div(\vec{v}) = \frac{1}{dv} * \frac{dv}{dt} \quad (7.10)$$

So we can write the term related to the reversible work $pdiv(\vec{v})$of equation (7.4) in the following manner:

$$pdiv(\vec{v}) = \ p \frac{dv}{dt} \frac{1}{dv} \quad (7.11)$$

The last statement expresses the work of compression and expansion in terms of volume variation. This is very useful for our application where, as shown in Fig. 7.2, we have a continuous variation of the volume.

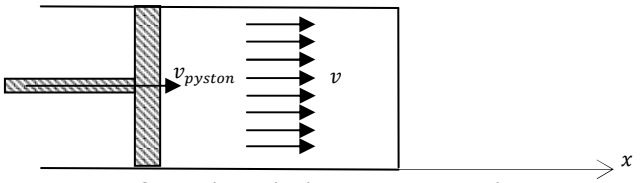

Figure 7.2 Sketch of the movement of the piston inside the compression chamber.

So we can write (7.5) for our application for a mono-dimensional space in the following way:

$$u * \frac{dM}{dt} + M * \frac{du}{dt} = \sum_{i}^{N} w_i * u_i - p * \frac{dV}{dt} \qquad (7.12)$$

We know that the specific enthalpy can be expressed according to the following formula:

$$h = u + p * v \qquad (7.13)$$

We now use this equation in the internal energy balance.

$$u * \frac{dM}{dt} + M * \frac{du}{dt} = \sum_{i}^{N} w_i * (h_i - p_i * v_i) - p * \frac{dV}{dt} \qquad (7.14)$$

We can now express the specific internal energy as follows:

$$du = T * ds - p * dv \qquad (7.15)$$

We can also write the specific entropy in the following manner:

$$ds(T, v) = \left(\frac{\partial s}{\partial T}\right)_v * dT + \left(\frac{\partial s}{\partial v}\right)_T * dv \qquad (7.16)$$

From the thermodynamic relations we can write the following equation:

$$\left(\frac{\partial s}{\partial v}\right)_T = \left(\frac{\partial p}{\partial T}\right)_v \qquad (7.17)$$

Using the definition of specific heat at constant volume we can state write the following expression:

$$\left(\frac{\partial s}{\partial T}\right)_v = \frac{c_V}{T} \qquad (7.18)$$

We can now substitute (7.17),(7.16) and (7.18) in (7.15) obtaining the following formula:

$$du = c_V * dT + \left(T * \left(\frac{\partial p}{\partial T}\right)_v - p\right) * dv \qquad (7.19)$$

We can differentiate the volume definition as follows:

$$V = M * v \qquad (7.20)$$

$$dV = dM * v + M * dv \qquad (7.21)$$

We can now obtain the time variation of the specific volume dividing (7.21) by *dt*.

$$M * \frac{dv}{dt} = \frac{dV}{dt} - v * \frac{dM}{dt} \qquad (7.22)$$

So we can write the first term of equation (7.14) in the following manner:

$$u * \frac{dM}{dt} + M * \frac{du}{dt} = u * \frac{dM}{dt} + c_V * \frac{dT}{dt} + \left(T * \left(\frac{\partial p}{\partial T}\right)_v - p\right) * \left(\frac{dV}{dt} - v * \frac{dM}{dt}\right) \qquad (7.23)$$

Furthermore we can write the energy balance in the following way:

$$u * \frac{dM}{dt} + M * c_V * \frac{dT}{dt} + \left(T * \left(\frac{\partial p}{\partial T}\right)_v\right) * \left(\frac{dV}{dt} - v * \frac{dM}{dt}\right) = \sum_i^N w_i * (h_i - p_i * v_i) - p * v * \frac{dM}{dt} \qquad (7.24)$$

We now define three different cases: compression and expansion, suction and discharge. Fig. 7.3 represents the different cases in terms of crank angle and associated internal pressure in the cylinder.

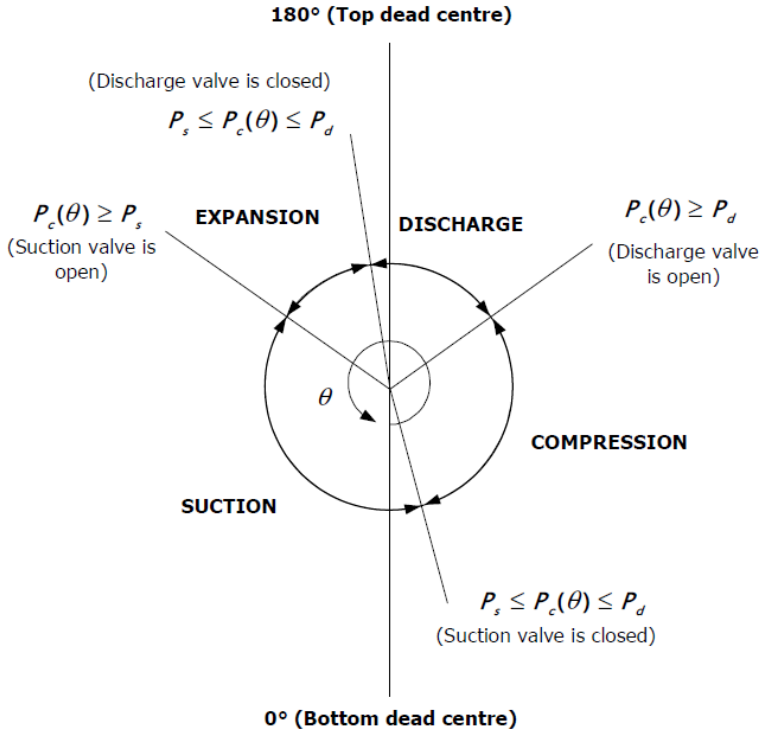

Figure 7.3 Schematization of the phases in a compressor cycle [18].

We are in the suction case when the internal pressure in the cylinder is lower than the suction pressure, i.e. the evaporation pressure. On the contrary we have discharge when the internal pressure in the chamber is higher than the discharge pressure, i.e. the condensation pressure. In all the other cases we have compression and expansion.
We can write the mass balance for every case in the following way:

$$Compression\ and\ Expansion: \quad \frac{dM}{dt} = 0\ with\ w_i = 0 \qquad (7.25)$$

$$Suction: \quad \frac{dM}{dt} = w_{suction} \qquad (7.26)$$

$$Discharge: \quad \frac{dM}{dt} = -w_{discharge} \qquad (7.27)$$

During the suction and the expansion we neglect the valve dynamics and we assume that our fluid could be considered incompressible. So, if we make the hypothesis of stationary conditions, we can apply the Bernoulli's equation through the following expression:

$$p + \rho * \frac{v^2}{2} + \rho * g * h = constant \quad (7.28)$$

We also make two other hypothesis. In primis, we hypothesize that the fluid inside the compression chamber does not have a significant speed during the suction and discharge process. Secondly, we neglect the term related to the difference of altitude in Bernoulli's equation. Using these hypothesis we can write the Bernoulli's equation during the suction and discharge process in following manner:

$$Suction:$$
$$p_{evap} + \rho_{suction} * \frac{v_{suction}^2}{2} = p \quad (7.29)$$

$$Discharge:$$
$$p = p_{cond} + \rho_{discharge} * \frac{v_{discharge}^2}{2} \quad (7.30)$$

From these two equations we can easily obtain the following expression for the flow rates.

$$Suction:$$
$$w_{suction} = A_{suction} * \sqrt{2 * (p_{evap} - p)/v_{suction}} \quad (7.31)$$

$$Discharge:$$
$$w_{discharge} = -A_{discharge} * \sqrt{2 * (p - p_{cond})/v} \quad (7.32)$$

Since we do not have exact information about the suction and the discharge area of the valves of the compression chamber, but we only know the suction and discharge tube diameters, we apply two correction coefficients to the Bernoulli's equation. So the mass flow rate can be expressed through the following equations:

$$Suction:$$
$$w_{suction} = A_{suction\_tube} * C_{suction} * \sqrt{2 * (p_{evap} - p)/v_{suction}} \quad (7.33)$$

$$Discharge:$$
$$w_{discharge} = -A_{discharge\_tube} * C_{discharge} * \sqrt{2 * (p - p_{cond})/v} \quad (7.34)$$

So we can write the internal energy balance for the three cases.

$$Compression\ and\ Expansion:$$

$$M * c_V * \frac{dT}{dt} + \left(T * \left(\frac{\partial p}{\partial T}\right)_v\right) * \left(\frac{dV}{dt} - v * \frac{dM}{dt}\right) = 0 \qquad (7.35)$$

$$Suction:$$

$$M * c_V * \frac{dT}{dt} + \left(T * \left(\frac{\partial p}{\partial T}\right)_v\right) * \left(\frac{dV}{dt} - v * \frac{dM}{dt}\right) = w_{suction} * (h_{suction} - h - p_{suction} * v_{suction}) \qquad (7.36)$$

$$Discharge:$$

$$M * c_V * \frac{dT}{dt} + \left(T * \left(\frac{\partial p}{\partial T}\right)_v\right) * \left(\frac{dV}{dt} - v * \frac{dM}{dt}\right) = w_{discharge} * \left(h - h_{discharge} + p_{discharge} * v_{discharge}\right) \qquad (7.37)$$

Finally we make the hypothesis of considering the enthalpy, the pressure and the specific volume at the discharge equal to the ones inside the cylinder obtaining the following energy balance during the discharge phase:

$$M * c_V * \frac{dT}{dt} + \left(T * \left(\frac{\partial p}{\partial T}\right)_v\right) * \left(\frac{dV}{dt} - v * \frac{dM}{dt}\right) = w_{discharge} * p * v \qquad (7.38)$$

We now show how we evaluate the instantaneous volume inside the cylinder. In Fig. 7.4 we show a schematization of the kinematics of the piston.

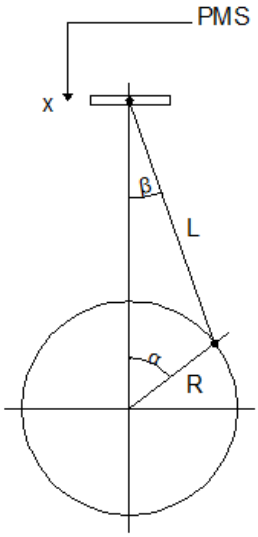

Figure 7.4 Sketch of the crank-connecting rod mechanism.

Knowing the length of the crank (R) and the length of the connecting rod (L) , the distance x from the dead superior point can be calculated through the following formula:

$$x = R + L - R * \cos(\alpha) - L * \cos(\beta) \quad (7.39)$$

We can apply the classical trigonometric relation obtaining the following expression of the position of the piston.

$$x = R * (1 - \cos(\alpha)) + L * \left(1 - \sqrt{1 - \left(R * \frac{\sin(\alpha)}{L}\right)^2}\right) \quad (7.40)$$

So we can finally compute the instantaneous volume of the compressor chamber as a function of the crank angle.

$$V_{cyl}(\alpha) = V_{dead} + A_{cyl} * R * (1 - \cos(\alpha)) + L * \left(1 - \sqrt{1 - \left(R * \frac{\sin(\alpha)}{L}\right)^2}\right) \quad (7.41)$$

Then we can also link the internal volume of the compression chamber with the time t using the following statement:

$$dt = \frac{d\alpha}{\frac{rpm}{60}} \quad (7.42)$$

7.3 Procedure to compute the outputs

The model allows us to compute four different parameters of the compressor: the compressor power, the flow rate, the heat released by the compressor and the temperature of the compressor body. We will now discuss the procedure to estimate these outputs from the theoretical model.

7.3.1 Compressor power

In the theoretical model we computed the instantaneous power for every $d\alpha$ through the following equation:

$$P_{inst} = -p * \frac{dV}{dt} \quad (7.43)$$

The compressor power was estimated as the average power of the compressor in the first three cycles according to this expression:

$$P_{average} = \frac{\int_0^{6\pi} P_{inst}\, d\alpha}{6\pi} \quad (7.44)$$

As we already stated we write the energy balance under certain hypothesis for an ideal case. So the average power that we compute from the theoretical model does not take into account the losses related to a real, i.e. not isentropic, compression. In Fig. 7.5 we see a comparison of an ideal and a real cycle without considering suction and discharge process.

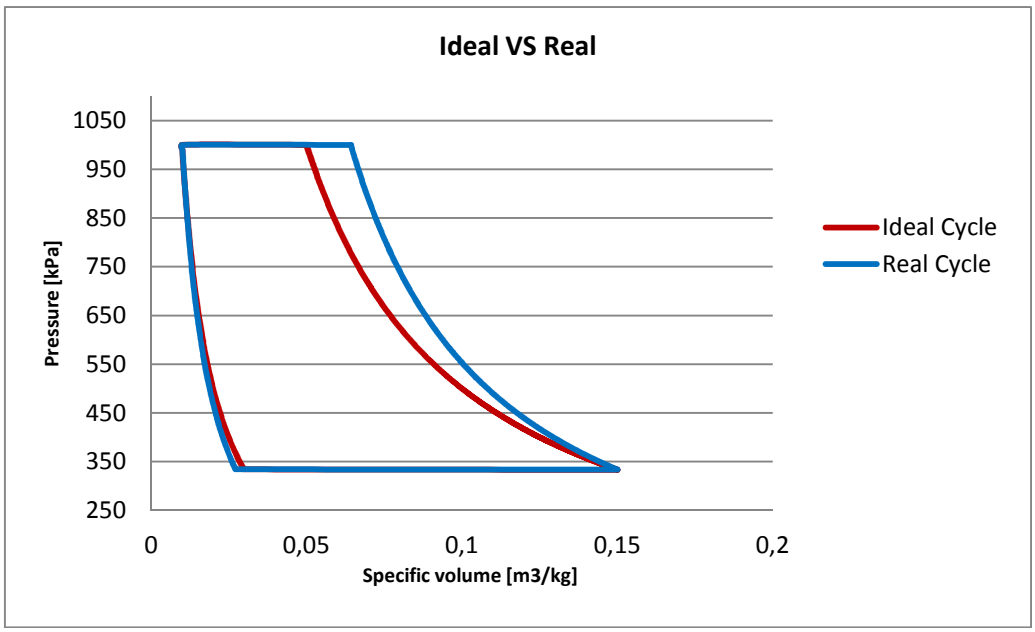

Figure 7.5 Comparison of an ideal and real compressor cycle without considering suction and discharge.

The difference of the areas of the two cycle represents the compression losses that we want to estimate. We can assume that in every operating condition the losses are proportional to the ideal power. So firstly, as Winandy et al. [19] did, we can take into consideration the losses of the real compression applying a proportional correction term to the theoretical average power. So we can write the average power in the following manner:

$$P_{average\_real} = \alpha_P * P_{average\_theoretical} \quad (7.45)$$

If we vary the operating conditions, i.e. for example a variation of the pressure ratio, we will see that the losses of the real cycle will not remain a fixed

percentage of the ideal work. To understand this concept we can assume that the shapes of the ideal and the real cycle correspond to two different parallelograms. In Fig. 7.6 we display two different simplified couples of real and ideal cycles for two different pressure ratios. In this simplified case we can easily compute the correction coefficient α and understand that it is not constant varying the pressure ratio.

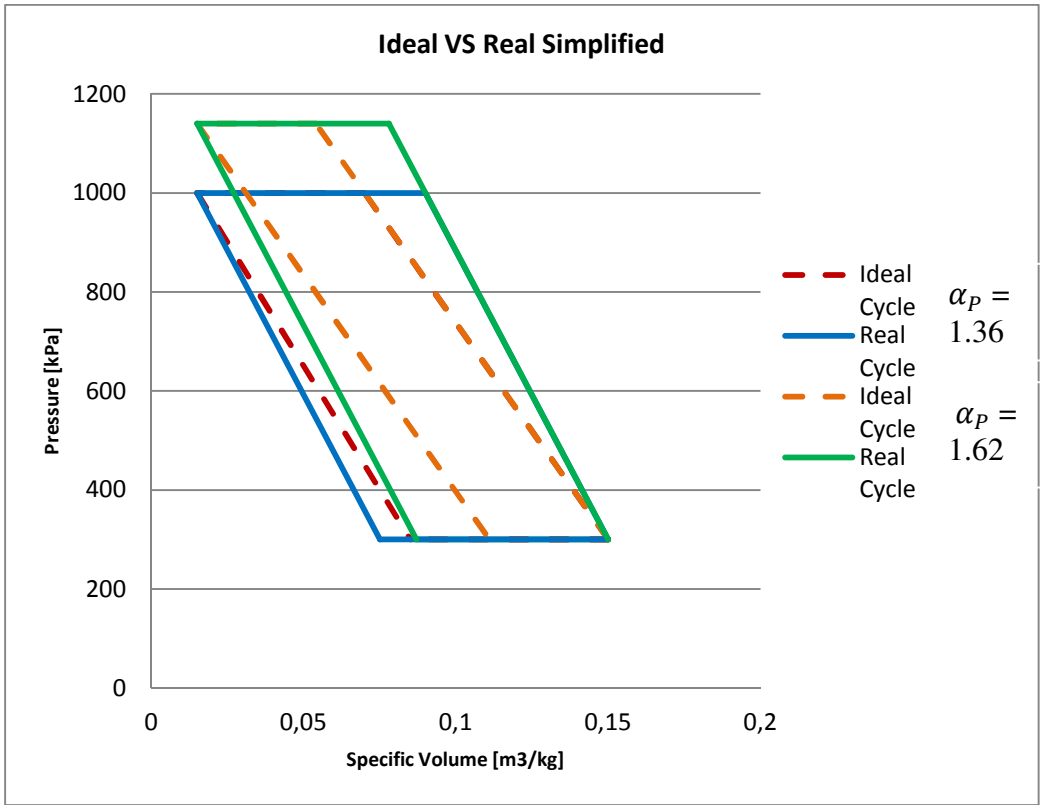

Figure 7.6 Comparison of different simplified ideal and real compressor cycles.

On the real scale we have two different simple methods to prove the same way that the corrective coefficient should vary with the pressure ratio. On the one hand we can divide the area of the cycles in very small parallelograms and we can compute the total area of the cycle as a sum of the areas of parallelograms. On the other hand, we can just compute the area of the cycles using a Montecarlo's method and then we can calculate the parameter α_P. So the percentage that represents the losses assumes different values according to different pressure ratios. We introduce this correction related to the pressure ratio in our model in the following way:

$$P_{average\_real} = \left(\frac{p_{cond}}{p_{evap}}\right)^{\gamma_P} \alpha_P * P_{average\_theoretical} \quad (7.46)$$

Since we want to have a prediction of the whole power required by the compressor we should also include a term that takes into account the hydrodynamic mechanical losses. As Winandy et al. [19] did, we assume that the term related to the mechanical losses is connected with the revolution speed (N) of the compressor. So we write the predicted power in the following manner:

$$P_{average\_real} = \left(\frac{p_{cond}}{p_{evap}}\right)^{\gamma_P} \alpha_P * P_{average\_theoretical} + P_{mecc\_0} * \left(\frac{N}{N_0}\right)^2 \quad (7.47)$$

N_0 is a arbitrary reference of the revolution speed.
Lastly we also include a term that represents the electrical losses of the compressor motor. So the predicted power of the model that should fit the experimental data is expressed by the following equation.

$$P_{average_{real}} = \left(\frac{p_{cond}}{p_{evap}}\right)^{\gamma_P} \alpha_P * P_{average_{theoretical}} + P_{mecc_0} * \left(\frac{N}{N_0}\right)^2 + P_{elet_0} \quad (7.48)$$

7.3.2 Mass flow rate

We decide to estimate the flow rate using the following expression:

$$\dot{m} = \rho_{suction} * V_{cyl} * N_{cyl} * \vartheta_{vol} * \frac{rpm}{60} \quad (7.49)$$

In order to apply this equation we should know the exact conditions at the inlet of the compressor chamber. We know the pressure, i.e. evaporating pressure, but we do not know exactly the temperature. In fact from the compressor datasheet we only know the suction temperature that is the temperature at the inlet of the compressor, but we do not know the temperature variation of the fluid in the suction tube of the compressor. So we make the hypothesis that the fluid increases its temperature of 5 °C in the suction tube. This value was chosen through a sensitivity analysis that showed that this temperature variation is the one that helps us to fit better the experimental data. So the only real unknown in this equation that should be evaluated through the model is the volumetric efficiency. We compute this term through the following definition:

$$\vartheta_{vol} = \frac{V_{real}}{V_{swept}} = \frac{\dot{m}}{\dot{m}_{ideal}} = \frac{\dot{m}}{\rho_{suction} * V_{cyl}} \quad (7.50)$$

As we can see in Fig. 7.7 the volumetric efficient is strongly dependent on the re-expansion volume. Since we do not have any information about this parameter from the compressor manufacturer we made a sensitivity analysis and we took a reasonable value of this parameter.

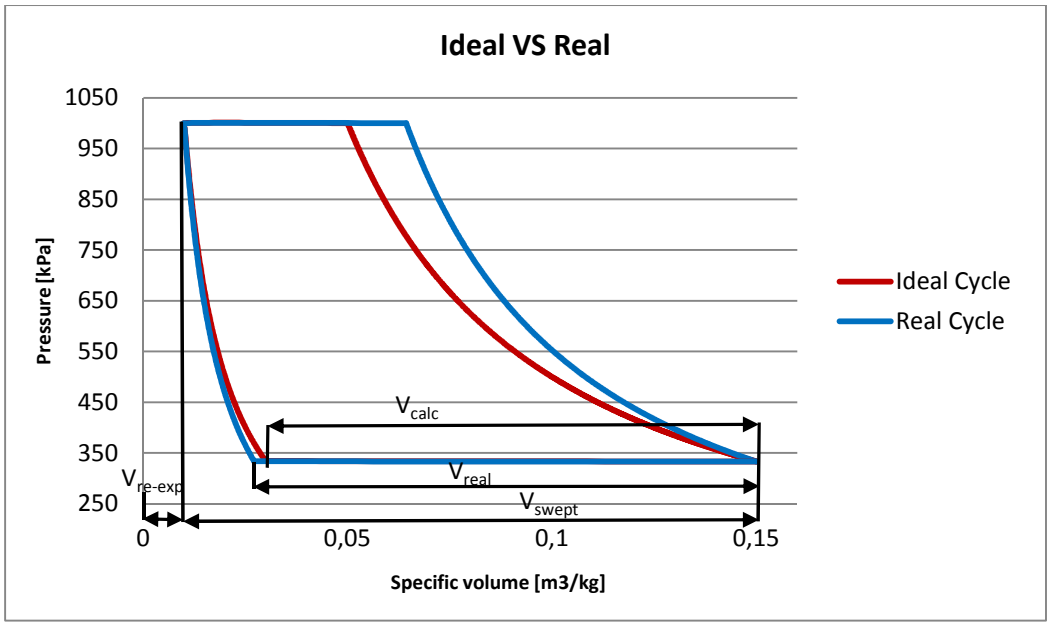

Figure 7.7 Sketch of the main relevant parameters to define the volumetric efficiency on a compressor cycle.

From the graph we can also conclude that the volumetric efficiency computed for an ideal cycle will be always different from the real one. Since the ideal and the real curve of re-expansion diverge, the more the pressure ratio gets higher the more the difference between the ideal and the real volumetric efficiency will grow. To take into account all these effects we apply the following correction:

$$\vartheta_{vol\_real} = \left(\frac{p_{cond}}{p_{evap}}\right)^{\gamma_{vol}} \alpha_{vol} * \vartheta_{vol\_theoretical} \quad (7.51)$$

Moreover we also include an additive correction to take into account the fluid leakages during the compression process. This additional coefficient allows us to have a better fitting of the predicted flow rate values with the experimental data. So in our model the volumetric efficiency was computed through the following formula:

$$\vartheta_{vol\_real} = \left(\frac{p_{cond}}{p_{evap}}\right)^{\gamma_{vol}} \alpha_{vol} * \vartheta_{vol\_theoretical} + \vartheta_{vol\_0} \quad (7.52)$$

7.3.3 Heat released and temperature of the compressor body

We compute the heat released by the compressor writing a stationary balance on the whole compressor. Fig. 7.8 schematizes the main parts of the compressor that were taken into account to design the balance equation.

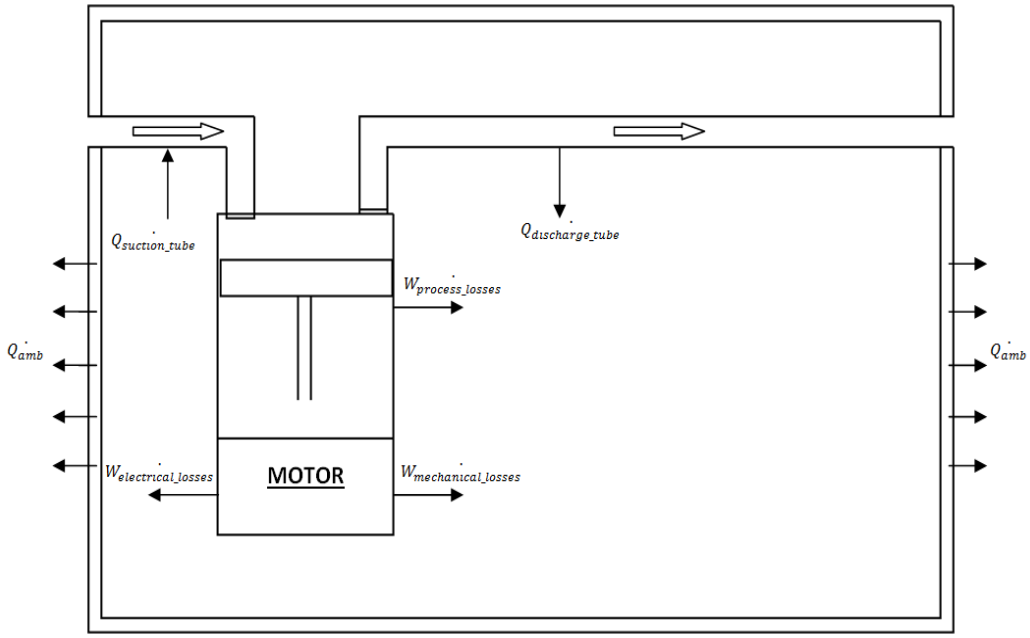

Figure 7.8 Sketch of the heat transfer problem inside the compressor.

From the picture we can see that we divided the compressor into four main parts: the compression chamber, the suction tube, the compressor motor and the discharge tube. With this simple representation of the real device we can write the energy balance in the following way:

$$\dot{W}_{electrical\_losses} + \dot{W}_{mechanical\_losses} + \dot{W}_{process\_losses} + \dot{Q}_{discharge\_tube} - \dot{Q}_{suction\_tube} = \dot{Q}_{amb} \quad (7.53)$$

The term $\dot{W}_{electrical\_losses}$ takes into account the released heat by the compression chamber. This heat corresponds to the difference between the theoretical work for adiabatic conditions computed by the model and the real work calculated applying the correction coefficients. So we can write this term in the following manner:

$$\dot{W}_{process\_losses} = P_{average\_real} - P_{average\_theoretical} = \left(\frac{p_{cond}}{p_{evap}}\right)^{\gamma_P} \alpha_P * \left(P_{average\_theoretical} - 1\right) \quad (7.54)$$

The term $\dot{W}_{mechanical\_losses}$ accounts for the friction heat released by the crank mechanism. So it can be written through the following expression:

$$\dot{W}_{mechanical\_losses} = P_{mecc\_0} * \left(\frac{N}{N_0}\right)^2 + P_{elet\_0} \quad (7.55)$$

Since our model is focused on a hermetic compressor we should also include a term related to the heat of the internal electrical motor writing the following equation:

$$\dot{W}_{electrical\_losses} = P_{elet\_0} \quad (7.56)$$

The fluid that exits the compression chamber moves into the discharge tube till the exit of the compressor. In this tube the fluid decreases its temperature giving additional heat to the compressor body. So we can write $\dot{Q}_{discharge\_tube}$ as follows:

$$\dot{Q}_{discharge\_tube} = \dot{m} * c_p * \left(T_{out_{compression\_chamber}} - T_{out_{compressor}}\right) \quad (7.57)$$

In the same way the heat absorbed by the fluid in the suction tube can be written trough the following equation:

$$\dot{Q}_{suction\_tube} = U_{suction-tube} * A_{suction-tube} * \left(T_{compressor-body} - T_{mean-suction}\right) = \dot{m} * c_p * \left(T_{in_{compression\_chamber}} - T_{in_{compressor}}\right) \quad (7.58)$$

Finally we can express $\dot{Q}_{amb}$ both considering the radiation and the natural convection processes using the same approximation that we adopt in the first model. So this term could be written in the following manner:

$$\dot{Q}_{amb} = (h_{rad-amb} + h_{conv-amb}) * A_{compressor} * \left(T_{compressor-body} - T_{amb}\right) \quad (7.59)$$

Since we make the hypothesis that our fluid heats of 5 °C in the suction tube, using equation (7.58) , we can directly compute the term $\dot{Q}_{suction\_tube}$.

Using equation (7.59) we can also estimate the temperature of the compressor body. We used the same correlation of section 6.2 to compute the natural convection heat transfer coefficient between the compressor and the ambient.
In order to compute the compressor body temperature we should estimate the heat transfer coefficient of the fluid in the suction tube. We make the hypothesis of having a uniform surface heat flux on the circular tubes caused by the heat compressor motor. Since our range of flow rates varies a lot for the different operating conditions, we implement an if-structure to use different correlations that fit every particular case. So we use two different correlations for the internal flow to compute the heat transfer coefficient in the laminar, the transition and the turbulent flow. In particular for the laminar flow we adopt the expression of Nusselt computed by solving heat transfer problem in a fully developed region into a circular tube characterized by uniform surface hat flux. For the transition and the turbulent flow we adopt the Gnielinski's correlation with the Petukhov's correlation to compute the Darcy's friction factor. So we can write the three correlation in the following manner:

$$Laminar:$$
$$Nu_D = 4.36 \quad (7.60)$$

$$Transition\ and\ Turbulent:$$
$$Nu_D = \frac{\left(\frac{f}{8}\right) * (Re_D - 1000) * Pr}{1 + 12.7 * \left(\frac{f}{8}\right)^{\frac{1}{2}} * \left(Pr^{\frac{2}{3}} - 1\right)} \quad (7.61)$$
$$with$$
$$f = (0.79 * \ln(Re_D) - 1.64)^{-2} \quad (7.62)$$

Moreover using equation (7.53) and (7.57) we can also obtain the discharge temperature at the outlet of the compressor. In fact we can compute both the term $\dot{Q}_{discharge_{tube}}$ and the discharge temperature at the outlet of the compressor chamber from the theoretical model, i.e. the temperature at the end of an isentropic compression. Since there are limited variations of temperature between the discharge of the compression chamber and the discharge of the compressor, we can make the hypothesis of stating that the value of the mean c_p in the discharge tube corresponds to the value of c_p at the outlet of the compression chamber. For example, in Fig. 7.9 we show the variation of c_p in a range of temperature that could be reached in the discharge tube for a selected operating condition (4500 rpm, evaporation temperature equal to 15 °C, condensation temperature equal to 35°C).

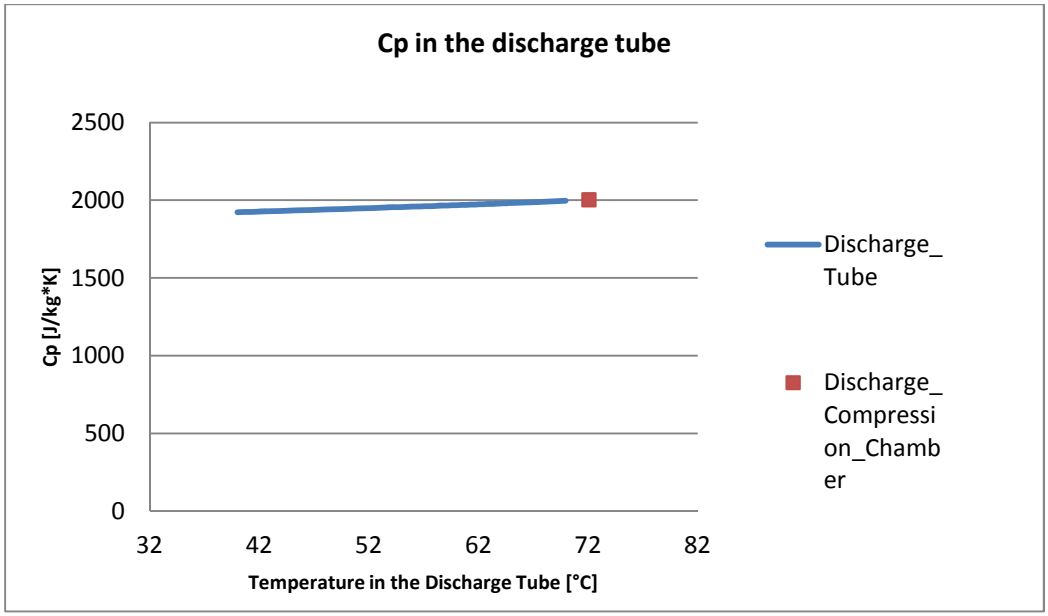

Figure 7.9 Variation of the specific heat at constant pressure in the discharge tube.

As we can see from the graph we have very small variation (less than 5%) of the c_p in the discharge tube. So we can reasonably assume a constant value of the c_p in the tube equal to the one at the discharge of the compression chamber. Once we did this hypothesis, the temperature at the compressor outlet can be easily computed through the following formula:

$$T_{out\_compressor} = T_{out\_compression\_chamber} - \frac{\dot{Q}_{discharge\_tube}}{\dot{m} * c_p} \quad (7.63)$$

7.4 Computational scheme

We developed our model using two different programs: Engineering Equation Solver (EES) and Microsoft Excel. The core of the model, i.e. the solution of the differential equations, is performed in EES. Then we make a minimization of the Absolute Average Deviation in Excel between the predicted values of the model and the experimental measurements taken from the datasheet of the compressor. So first we run a Macro in the EES model to have the predicted values for every operating condition that is displayed in the datasheet. The model requires different parameters to be run. In particular some of them are available in the datasheet (displacement, stroke, suction tube area, discharge tube area) and some others (dead volume, C_s, C_d, increase of temperature in the suction tube and the length of the connecting rod) were found through a sensitivity analysis. After that we compare the estimated and the real values of power and flow rate in Excel and we

minimize γ, α_P, P_{mecc_0}, P_{elet_0}, γ_{vol}, α_{vol} and ϑ_{vol_0} to pass from the ideal cycle computed by EES to the values related to the real cycle. Once we performed these steps we can compute the power and the flow rate for every condition. Then we make another small model in EES to calculate the heat released to the ambient and the temperature of the compressor body. This second model takes as inputs the operating conditions, the real power, the mass flow rate and the emissivity of the external surface of the compressor. In particular this last parameter was manually set to fit the experimental measurements. In Fig. 7.10 we try to summarize the computational scheme behind our model.

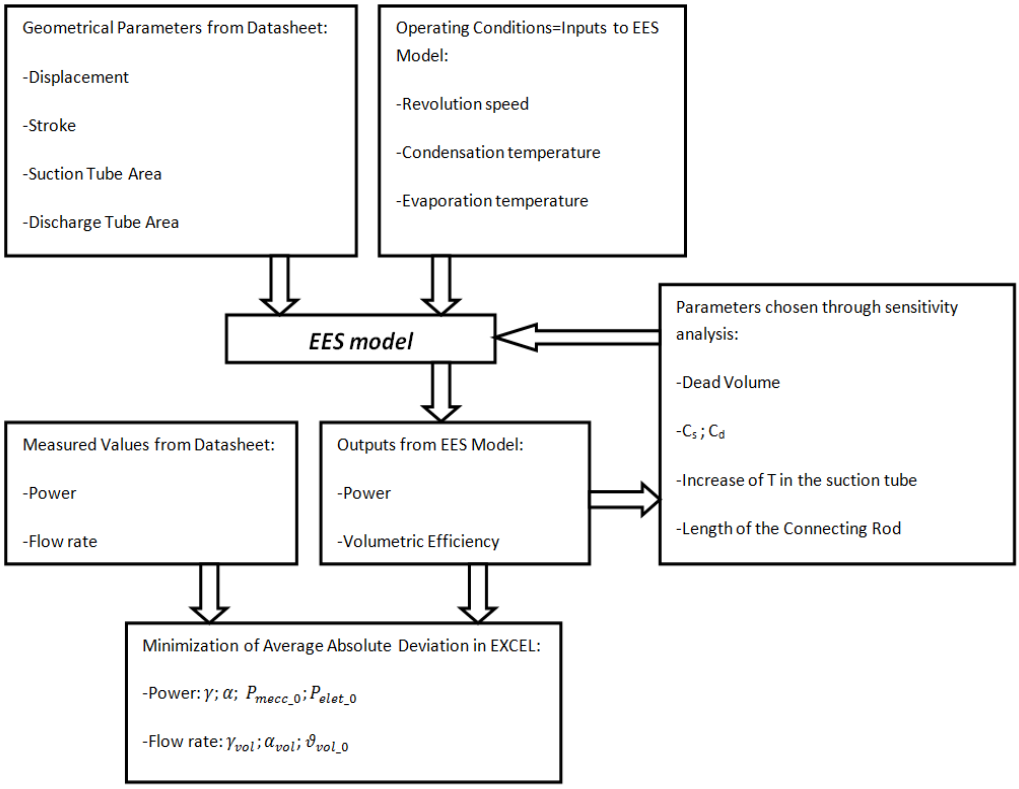

Figure 7.10 Sketch of the computational scheme used in the differential model.

As we already stated, we chose some parameters through a sensitivity analysis. In every case we vary one value keeping the others constant. So for each factor we run the model and we see which value of the parameter was the one that provided the best fitting of the experimental data. The range of variation of every parameter was chosen both in agreement with experimental measurements on similar compressors and on geometrical assumptions. In Fig. 7.11 and Fig. 7.12 we show the sensitivity analysis for the increase of temperature in the suction tube. This parameter has to be carefully selected because it plays a crucial role in the heat exchange part of the model.

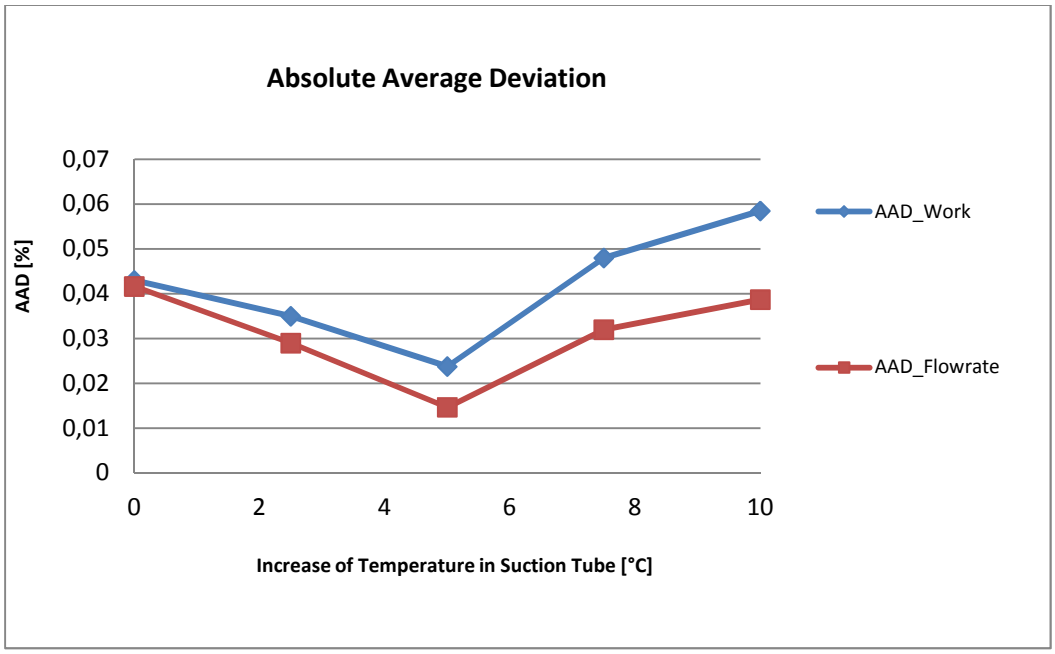

Figure 7.11 Sensitivity analysis on the increase of temperature of the refrigerant in the suction tube regarding the absolute average deviation.

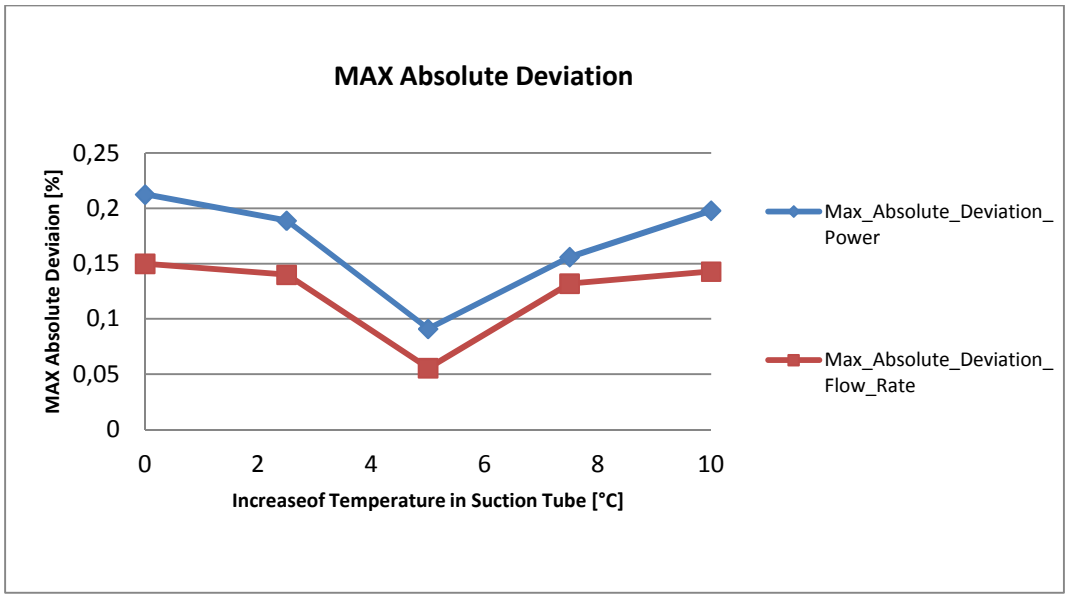

Figure 7.12 Sensitivity analysis on the increase of temperature of the refrigerant in the suction tube regarding the maximum absolute deviation.

From the graphs it is evident that both to fit the mass flow rate and the compressor power we should select a value of heating in the suction tube equal to 5 °C. Moreover in Fig. 7.13 and 7.14 we display the sensitivity analysis for the dead volume. We express the dead volume as a percentage of the

displacement. The dead volume should be accurately chosen because it affects a lot the volumetric efficiency computed by the model.

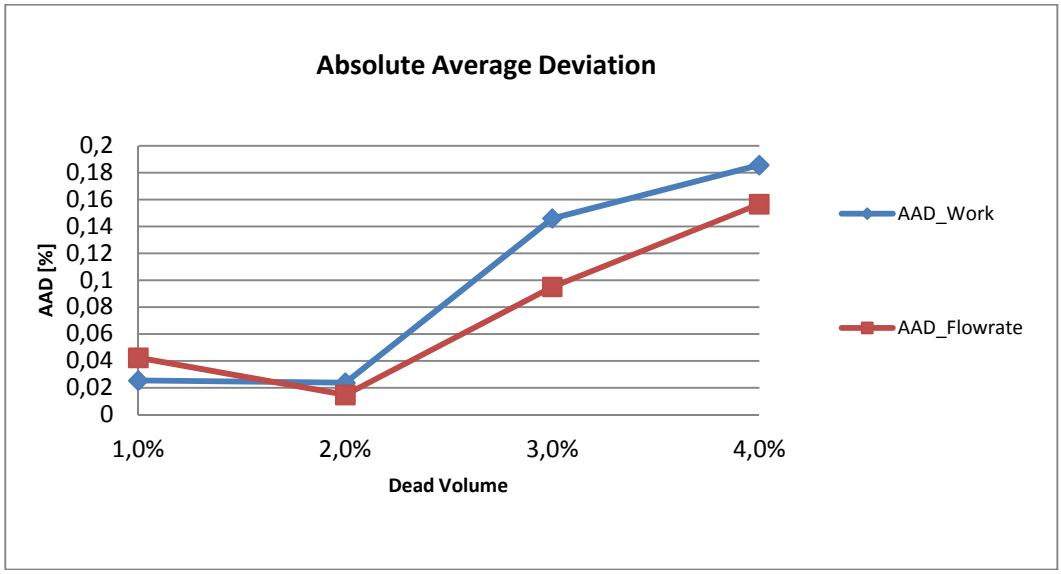

Figure 7.13 Sensitivity analysis on the dead volume of the compressor chamber regarding the absolute average deviation.

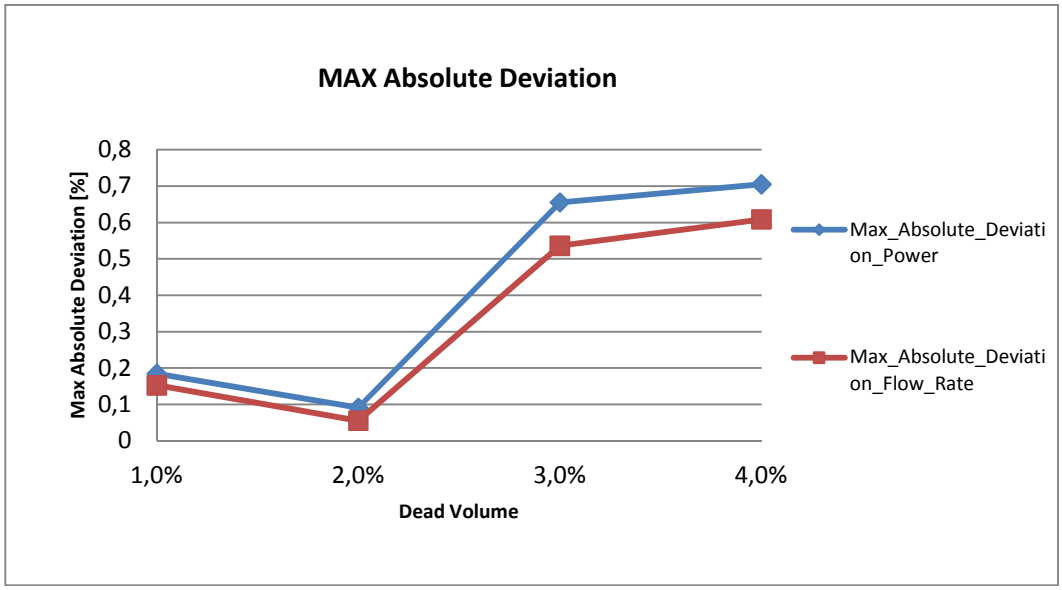

Figure 7.14 Sensitivity analysis on the dead volume of the compressor chamber regarding the maximum absolute deviation.

From the plots we realize that the best choice of the dead volume corresponds to 2% of the displacement. As other authors stated [20], this is a very typical value of dead volume for hermetic reciprocating compressors. Since C_s, C_d and the length of the connecting rod do not have a strong impact on the behavior and on

the performances of the model, we will not show the graphs of the sensitivity analysis of these parameter. The final values of these factors are displayed in the table 7.1.

Table 7.1 Some coefficients of the model determined through a sensitivity analysis.

Correction Coefficient for the area of the suction	C_s	0.3
Correction Coefficient for the area of the discharge	C_d	0.3
Length of the connecting rod of the compressor	L [m]	0.025

7.4 Results

Minimizing the Absolute Average Deviation between the predicted values of power and mass flow rate and the experimental ones, we obtain the values of the coefficients shown in table 7.2.

Table 7.2 Minimized correction coefficients of the model.

Correction factor related to the pressure ratio for the compressor power	γ_P	0,0640
Proportional correction factor for the compressor power	α_P	1,0138
Mechanical losses correction factor for the compressor power [W]	P_{mecc_0}	7,0002
Electrical losses correction factor for the compressor power [W]	P_{elet_0}	4,0352
Correction factor related to the pressure ratio for the volumetric efficiency	γ_{vol}	-0,2527
Proportional correction factor for the theoretical volumetric efficiency	α_{vol}	0,6253
Correction factor related to the leakages for the volumetric efficiency	ϑ_{vol_0}	0,4519

In Fig. 7.15 we show a comparison between the experimental and the predicted values of the VEMC9C compressor power at five different revolution speeds.

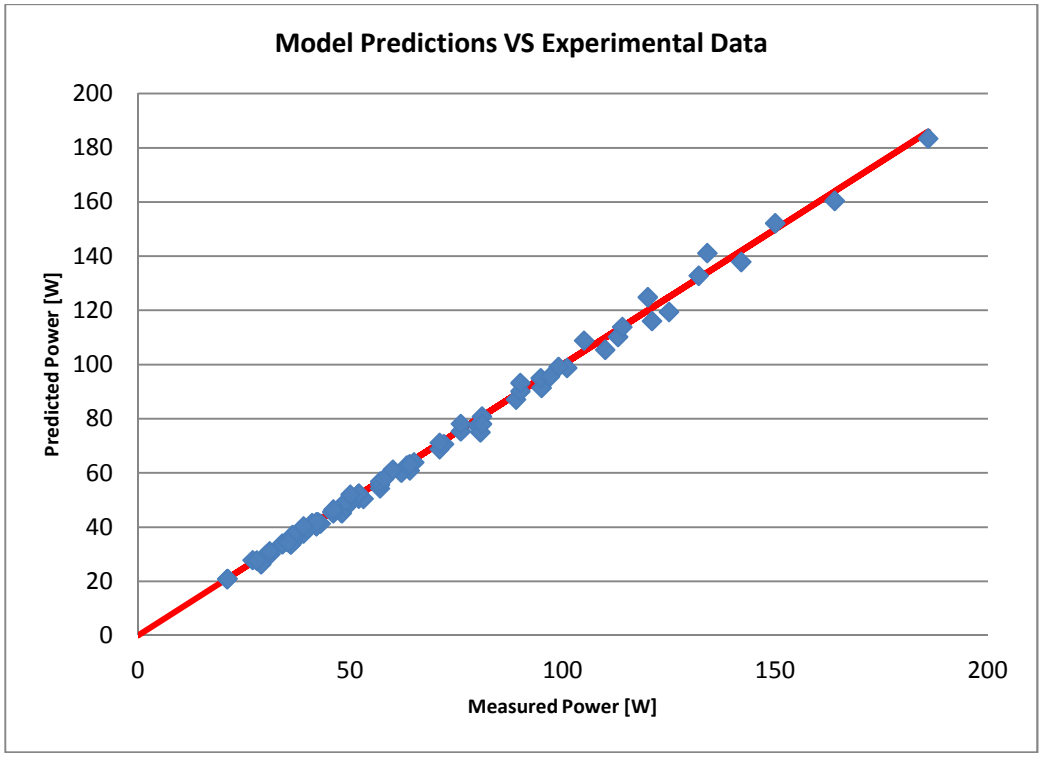

Figure 7.15 Comparison between predicted and measured values of the compressor power using the differential model.

From the graph we can see that the predicted values of the compressor power are in good agreement with the measurements of the compressor manufacturer. The measures of power and flow rate made by EMBRACO have an uncertainty of +-5%. Our model fits the 81 experimental points with a Absolute Average Deviation equal to 2.4 % and a maximum absolute deviation of 9.1 %. All the predicted points are in the range of -+5% from the experimental values except from four points that have relative errors equal to 6.7%, 6.9%, 5.9% and 9.1%. Three out of four of these points are placed at different revolution speeds at the highest pressure ratio, i.e. evaporation temperature equal to -35°C and condensation temperature equal to 55 °C. We do not manage to find any physical reasons for this behavior. Fig. 7.16 displays the comparison between the model and the measured values of the mass flow rate.

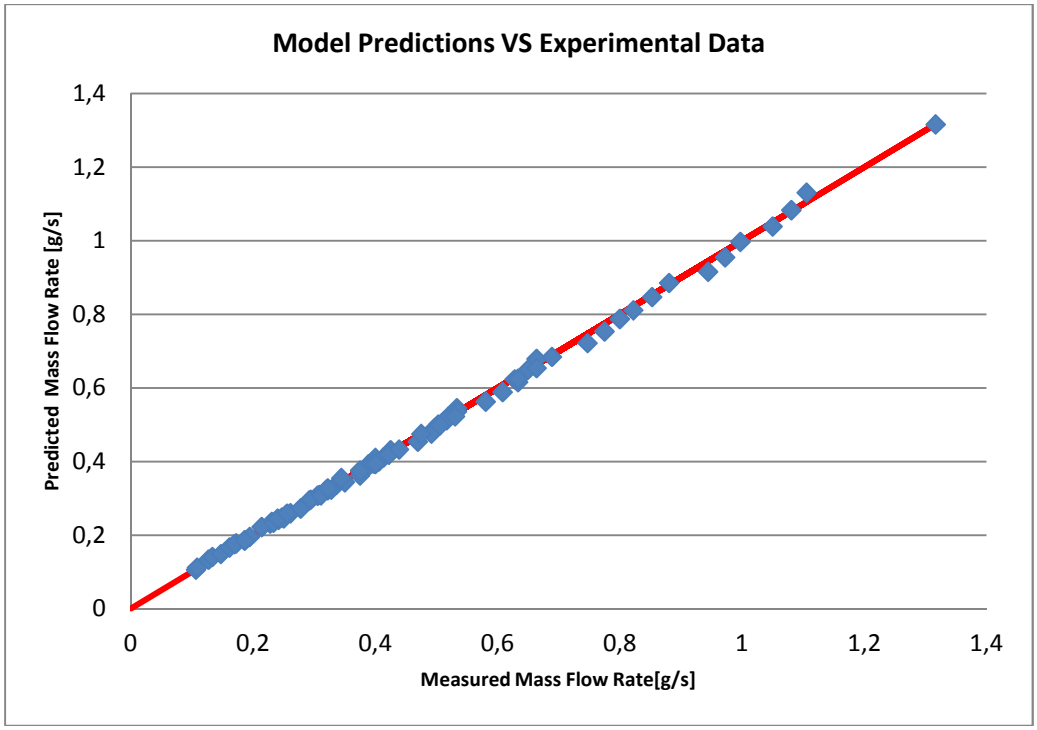

Figure 7.16 Comparison between predicted and measured values of the compressor mass flow rate using the differential model.

From the chart we can observe that the predicted values of the compressor mass flow rate are also in good agreement with the measurements of EMBRACO. Our model fits the 81 experimental points with a Absolute Average Deviation equal to 1.5 % and a maximum absolute deviation of 5.5 %. All the predicted points are in the range of -+5% from the experimental values except from one point that shows a relative error equal to 5.5%. We didn't manage to find any precise motivation for the relative error of this particular point. We also try to double check the physical meaning of the correction terms. We only manage to find data about the electrical part of the compressor motor and so we double check the correction term P_{elet_0} implemented in the model. For example we define the electrical efficiency of the compressor according to our assumption as in the following way:

$$\eta_{elet} = \frac{P_{elet\_0}}{P_{average\_real}} \quad (7.64)$$

In Fig. 7.17 we plot the electrical efficiency at different revolution speeds for a fixed value of the pressure ratio. In Fig. 7.18 we display the trend of the electrical efficiency for two different revolution speed varying the pressure ratio.

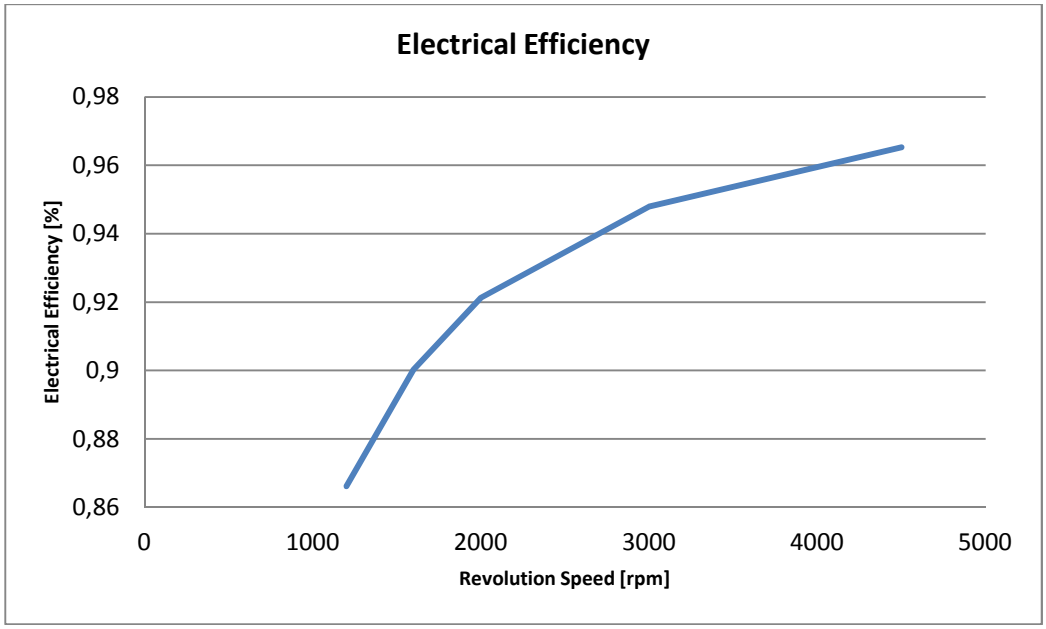

Figure 7.17 Trends of the electrical efficiency of the compressor varying the revolution speed.

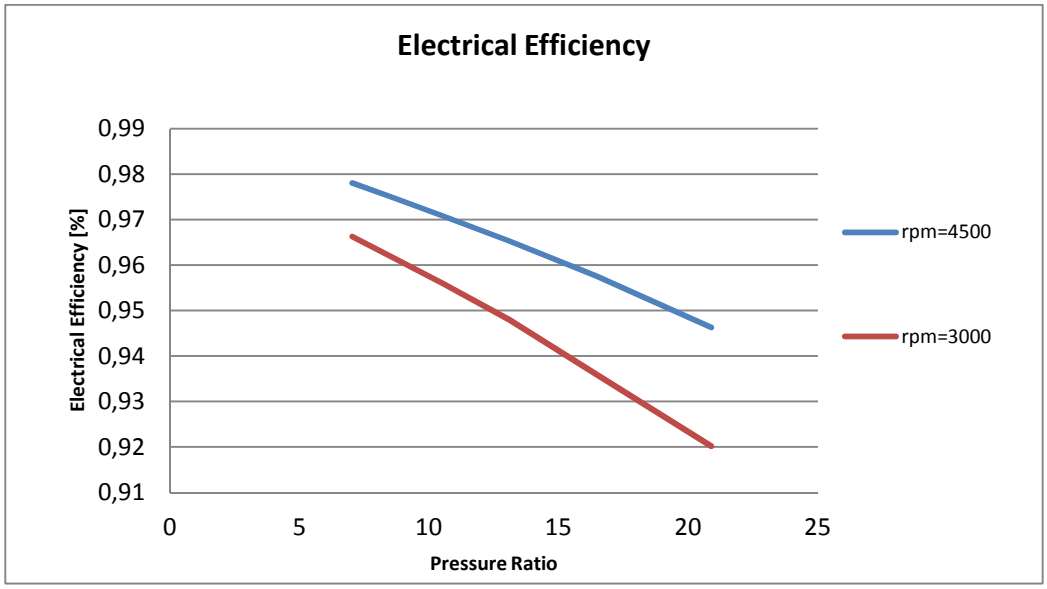

Figure 7.18 Trends of the electrical efficiency of the compressor varying the pressure ratio.

We try to make a comparison between the predicted trends and values of the electrical efficiency and some measured values for similar compressors taken from internal communications. We also compare the trends with some available graphs in the literature. The trends and the values of our model demonstrate a good agreement in both comparisons. So we have an initial confirmation of the assumption behind the term P_{elet_0} of the model.

Moreover we try to use our model for other similar hermetic reciprocating compressors of the same manufacturer. We consider the same model parameters that we found to be valid for our compressor and so we do not repeat all the sensitivity analysis.
First we try to apply our model on the VEM9ZC compressor. The reason behind the choice of this compressor was that it has similar geometrical parameters (displacement, bore, stroke) to the compressor on which we developed the model. So in Fig. 7.19 we show the comparison between the predicted and the experimental values of the power for VEM9ZC compressor.

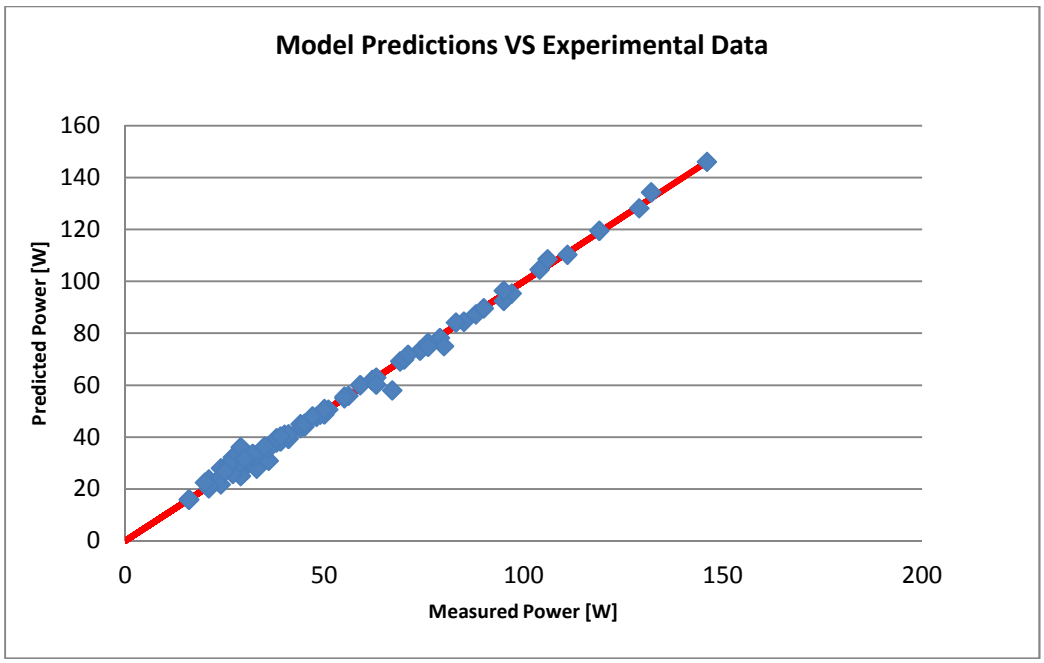

Figure 7.19 Comparison between predicted and measured values of the VEM9ZC compressor power using the differential model.

As we can see from the graph in this case we have a very good fitting between the predicted and the experimental values. The model manages to converge for 66 out of the 72 points displayed in the datasheet. In Fig. 7.20 we show the comparison between the model and the measured values of the mass flow rate of VEM9ZC compressor.

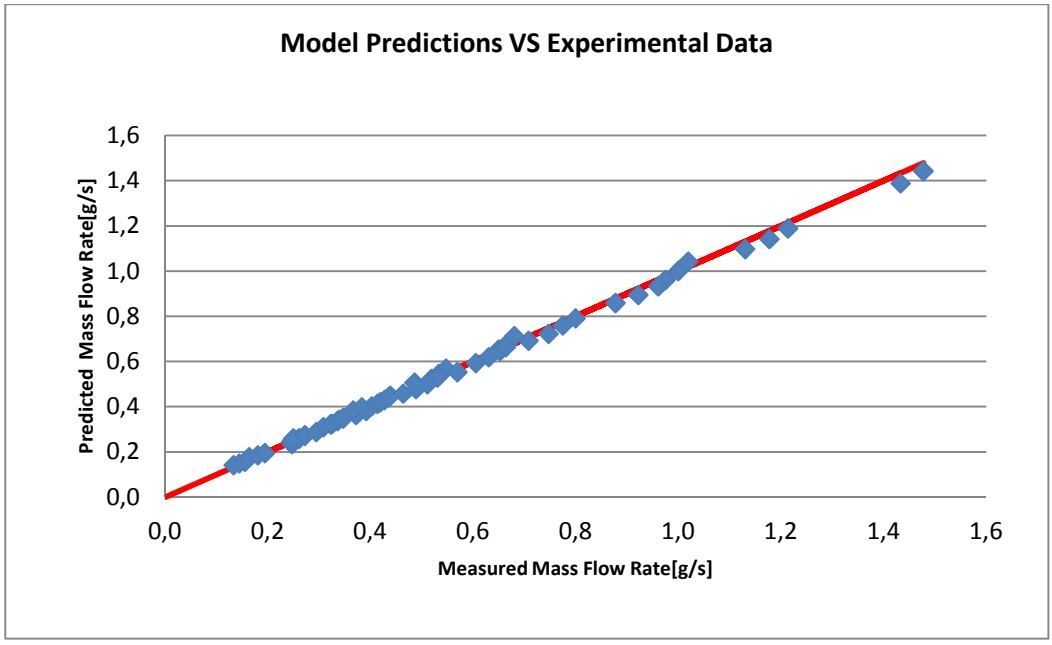

Figure 7.20 Comparison between predicted and measured values of the VEM9ZC compressor mass flow rate using the differential model.

In this case we still have a good agreement of the model and the reality. In the points where the model converges, it shows a good fitting of the experimental values. The significant results of the fitting with the experimental points are shown in the table 7.3.

Table 7.3 Main parameters related to the model predictions of power and mass flow rate for the VEM9ZC compressor.

Compressor VEM9ZC	*Average Absolute Deviation*	*Max Absolute Deviation*	*Number of points out of the range -+5% from the experimental data*
Power	*1.98 %*	*6.7 %*	*3*
Mass Flow Rate	*2.08 %*	*7.8 %*	*2*

Secondly, we apply our model to the VEMC7C compressor that has very different geometrical parameters from our standard compressor (i.e. different bore, stroke, displacement and diameters of suction and discharge lines). In Fig. 7.21 and Fig. 7.22 we show the comparison between the predicted and the experimental values of the compressor power and the mass flow rate.

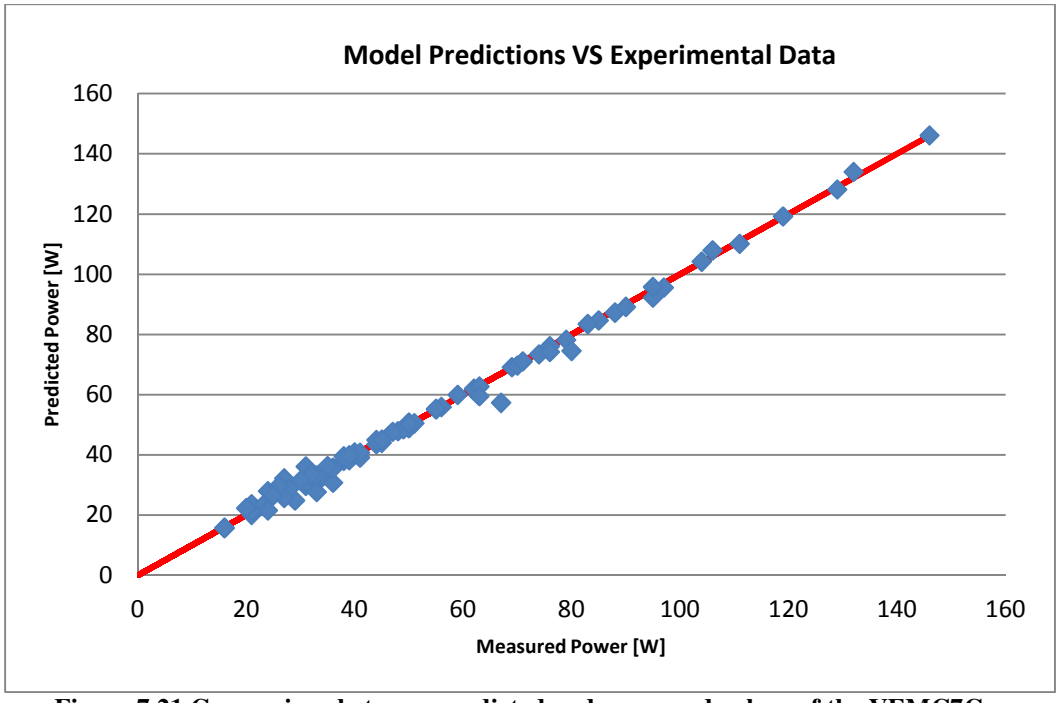

Figure 7.21 Comparison between predicted and measured values of the VEMC7C compressor power using the differential model.

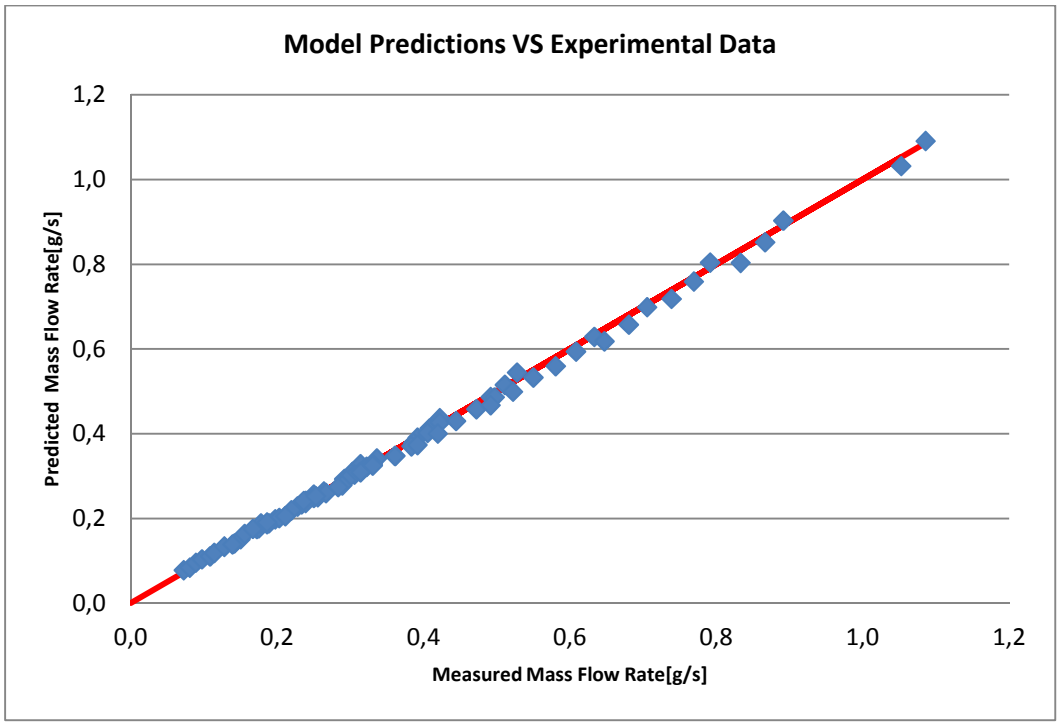

Figure 7.22 Comparison between predicted and measured values of the VEMC7C compressor mass flow rate using the differential model.

From these graphs we can conclude that the model does not manage to fit very precisely the experimental data. In fact in this case we only have an agreement between the predicted and the experimental value of ±15% for the compressor power and ±7% for mass flow rate. In this case, out of 81 fitted points, we have 15 points for the power and 7 points for the mass flow rate that are out of the ±5% range from the experimental value. The reason behind this behavior of the model lies in the sensitivity analysis on the dead volume. We performed this analysis only on our standard compressor obtaining a dead volume equal to 2% of the displacement. On the one hand, in the case of the VEM9ZC compressor we have a similar displacement to our standard compressor, the model fits precisely. On the other hand, in the case of the VEMC7C compressor we have a very different displacement and so we probably have also a different percentage of the displacement that would represent the dead volume. For this reason in the last case we do not have such a precise fitting as in the other cases. In order to have a better fitting also for the VEMC7C case we should perform again a sensitivity analysis on the dead volume.
Finally we also try to compare the predicted temperatures of the compressor body with some few measurements that we took with the experimental setup explained in chapter 2. Since these measurements requires lots of time because the appliance should reach a steady state from an off state, we just manage to measure six experimental points. The results are shown in Fig. 7.23.

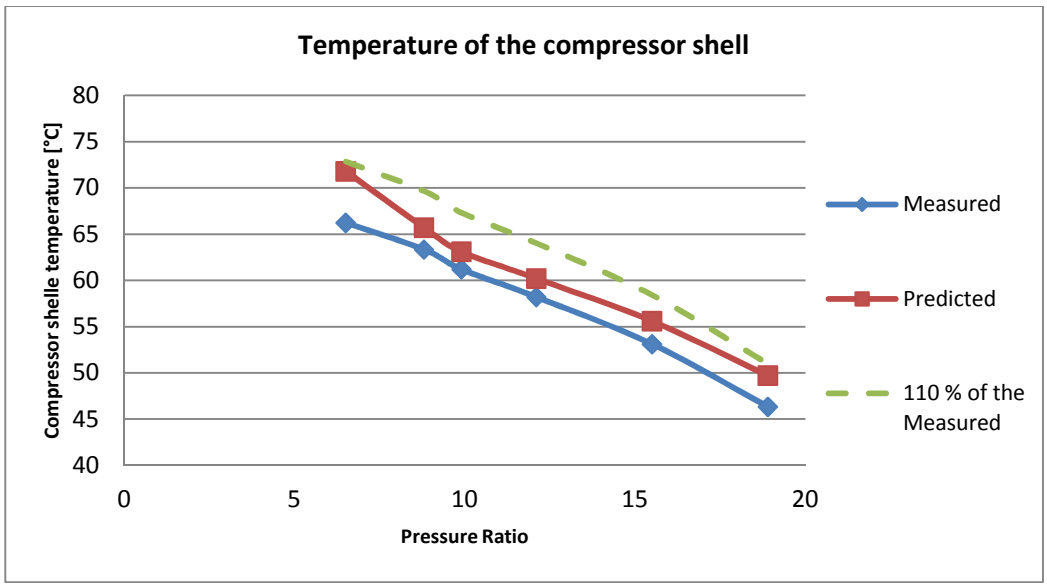

Figure 7.23 Comparison between predicted and measured values of the shell temperature of the VEMC9C compressor.

As we can see from Fig. 7.23 the model manages to predict the temperature of the compressor shell with an accuracy of 10 %. So the predicted temperatures by the model should not be considered the exact real compressor shell

temperatures, but just some values to have the order of magnitude of the phenomenon.

7.5 Comparison among different models

In this section we try to compare the results of the different models that we implemented for the VEMC9C compressor. In primis we make a comparison among the polytrophic model, the differential model and the experimental results. In Fig. 7.24 we show the different trends for the compressor power.

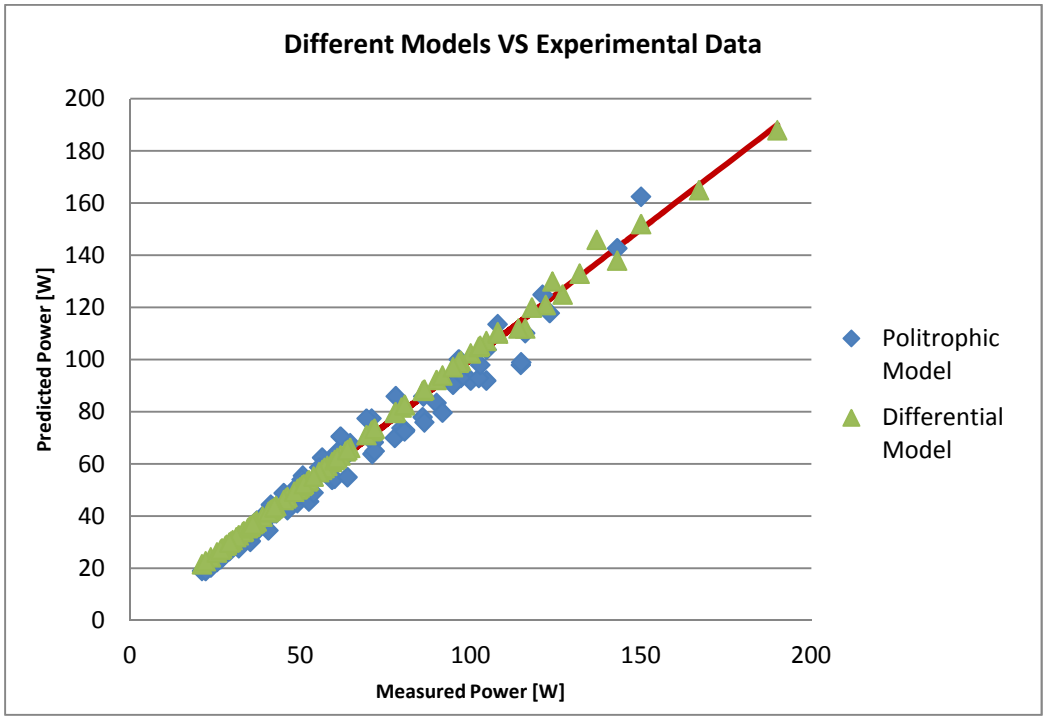

Figure 7.24 Comparison between polytrophic model, differential model and experimental data regarding the compressor power.

As we can see from Fig. 7.24 the polytrophic model fits good only for low power, while the differential model keeps its validity for the whole range of powers. The trend shown is Fig. 7.24 reflects the basic assumption behind the polytrophic approach. This model assumes the refrigerant to be an ideal gas and so it shows good results only in the points of low power where the ideal gas approximation better fits the refrigerant behavior.
Moreover, we also implement the EN 12900 model to calculate power input to the compressor. This model belongs to the models of the first category. We adopt this additional model to test the results of our model also on specific conditions that are not in the datasheet. The Appendix I of EN 12900 describes the procedure to extrapolate from the existing power measures supplementary

data for different temperature and pressure conditions. The standard states that if we consider a 4-D space with the evaporation temperature, the condensation temperature and the compressor speed on the axis, we can describe the power required by the compressor as a ipersurface. If we fix a value of one of the three axis parameters, EN 12900 claims that the power can be obtained using a simple correlation with ten coefficients among the power and the other two free axis parameters. The standard adopts the same procedure also to compute the mass flow rate for different conditions. For example, we can obtain the compressor power at a fixed compressor speed varying the evaporation temperature and the condensation temperature through the following expression:

$$P_{RPM} = f\left(T_{evap}; T_{cond}\right) = \\ = C_1 + C_2 * T_{evap} + C_3 * T_{cond} + C_4 * T_{evap}^2 + C_5 * T_{evap} * T_{cond} + C_6 * T_{cond}^2 + C_7 * T_{evap}^3 + + C_8 * T_{evap}^2 * T_{cond} + C_9 * T_{evap} * T_{cond}^2 + C_{10} * T_{cond}^3 \quad (7.65)$$

Using Matlab™ we found the ten coefficients for the five revolution speeds of the compressor datasheet. Then, as we can see in Fig. 7.25 and Fig. 7.26, we compare the EN12900 model with the experimental data.

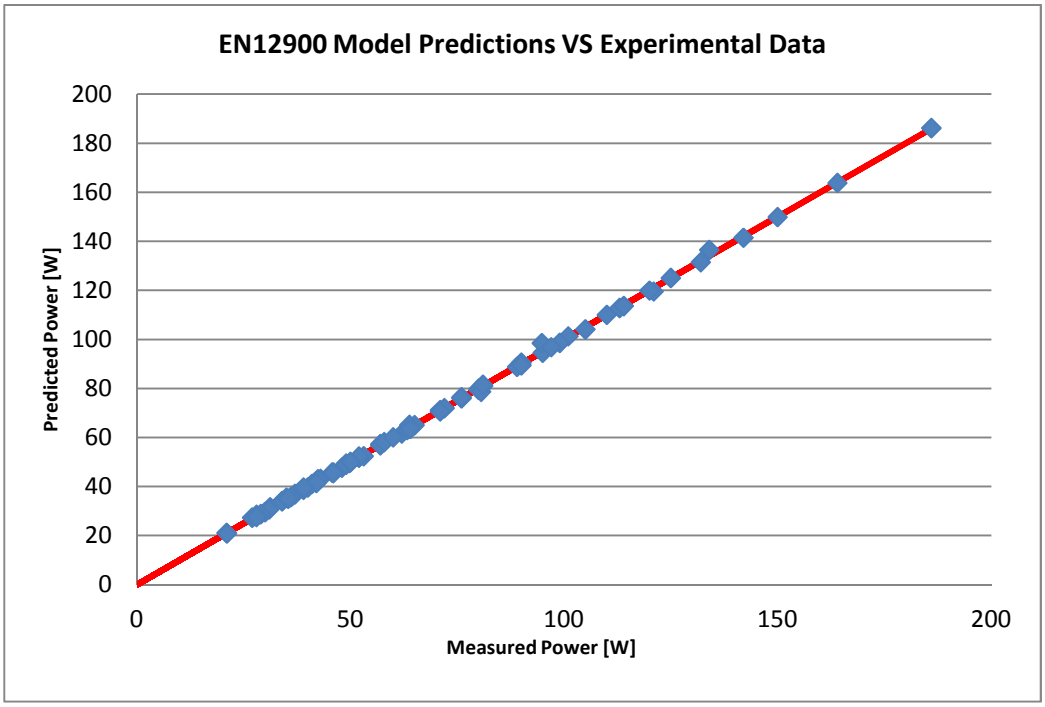

Figure 7.25 Comparison between predicted and measured values of the compressor power using the EN12900 model.

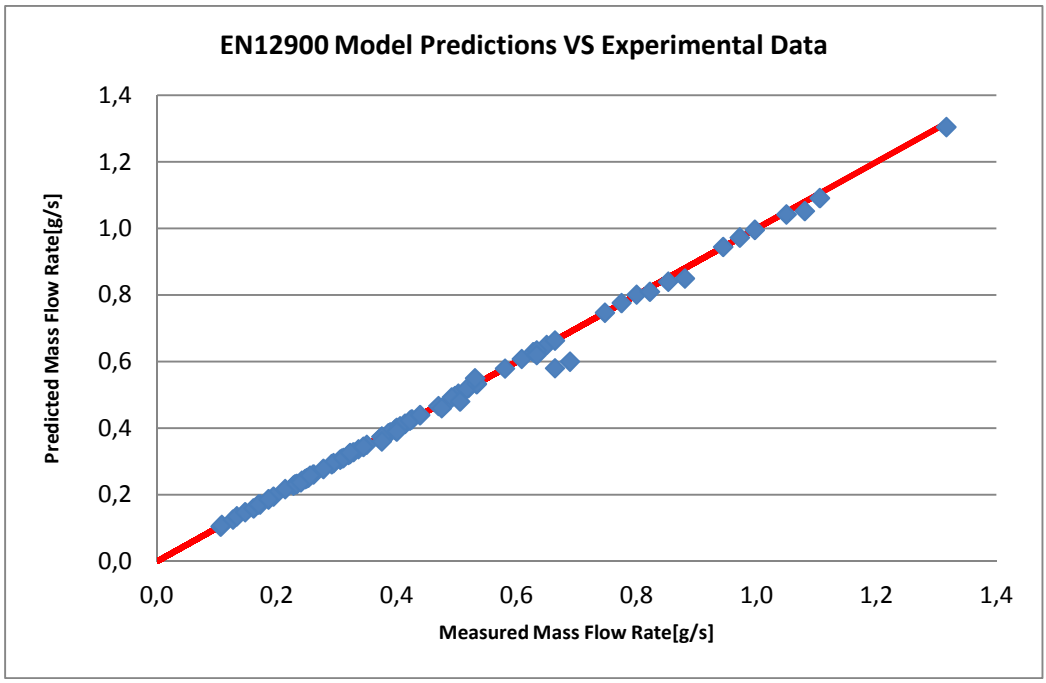

Figure 7.26 Comparison between EN12900 predicted and measured values of the compressor mass flow rate using the EN12900 model.

This model shows a very precise agreement with the experimental values. It converges for all the considered points with a good accuracy in the fitting. The main indicators about the accuracy of the ten coefficients fitting are shown in Tab. 7.4.

Table 7.4 Indicators of the fitting between the experimental and the predicted values of power and mass flow rate for VEMC9C compressor.

EN12900 model	*Average Absolute Deviation*	*Max Absolute Deviation*	*Number of points out of the range -+5% from the experimental data*
Power	*0.63 %*	*3.92 %*	*0*
Mass Flow Rate	*0.82 %*	*9.54 %*	*2*

From these results we can conclude that the ten coefficient model is widely spread among compressor manufacturers because of its simplicity and of its precision in the fitting. Finally in Fig. 7.27 and Fig. 7.28 we compare the differential model with the EN12900 model.

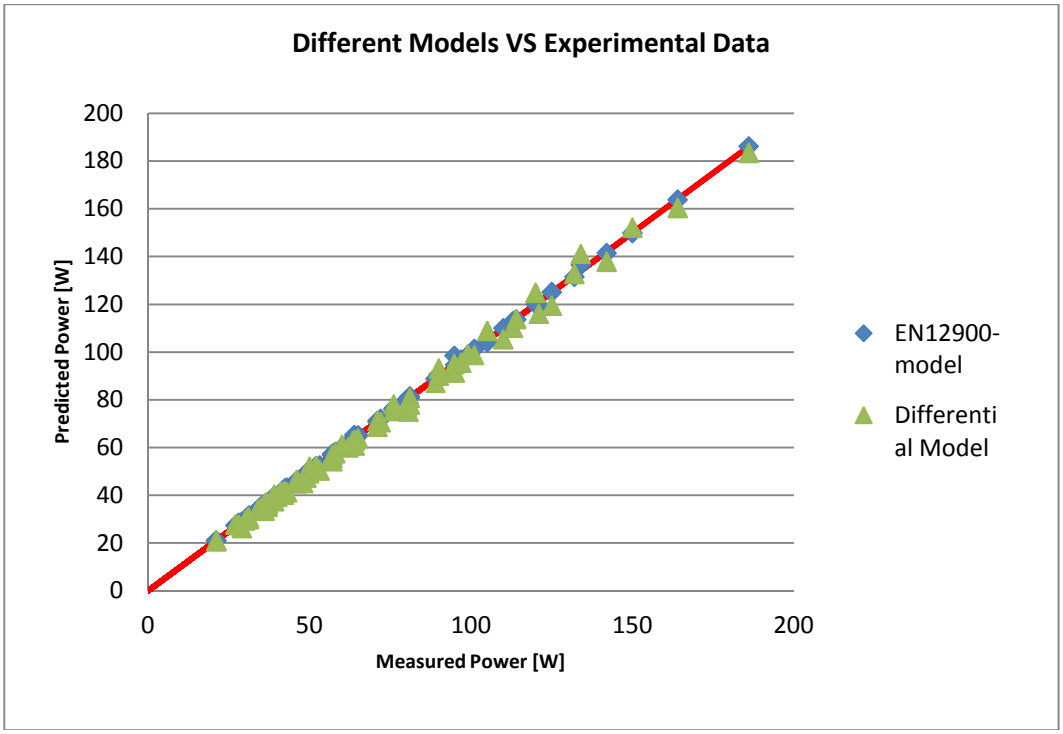

Figure 7.27 Comparison between EN12900 model, differential model and experimental data regarding the compressor power.

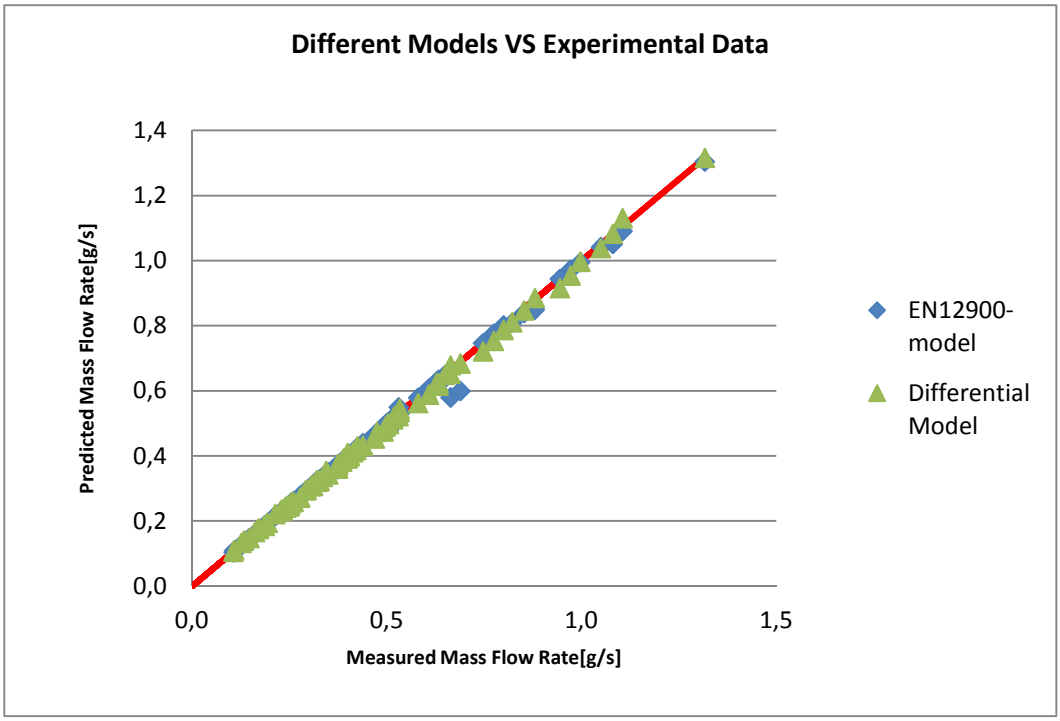

Figure 7.28 Comparison between EN12900 model, differential model and experimental data regarding the mass flow rate.

From the graphs we can see that both the models show a good match with the experimental data. Every model has different advantages and drawbacks. On the one hand, the EN12900 model requires different minimizations (one for every revolution speed) to get the power and mass flow rate, while the differential model necessitates only a single general minimization. On the other hand, the computational time of the EN12900 model is very low and fragmented (i.e. we run lots of different fast minimization), while the computational time of the differential model is longer and concentrated (i.e. we run the minimization only after the calculation of the results from the EES model for all the points of the datasheet). Finally, even if the ten coefficient model is very simply to run, it completely lacks of physical assumptions. In other words the first category models are only a best fitting of the experimental data, but they do not rely on a real analysis of the compressor.

7.6 Conclusions

Since the first polytrophic model did not show a high accuracy, we implemented the second differential model for the VEMC9C compressor. This model relied on the principles of conservation of energy and mass. Using this second model we managed to have a fitting of the experimental data in the range -+5% (i.e. the range of uncertainty of the measurements). The differential model relied both on some approximations that we made to solve the energy and mass balances and both on some physical assumptions that allowed us to shift the ideal compression results of the differential equations to the real compression. The model showed a good behavior for different compressors. Every time we want to apply this model to a new hermetic reciprocating compressor we should make the sensitivity analysis at least on the dead volume. While the EN12900 model required different quick minimizations for all the different revolution speeds of the compressor, this differential model required only one minimization after a long (30 minutes) run of the EES part of the model. Our model fitted around 90 conditions at five different revolution speeds (1200 rpm, 1600 rpm, 2000 rpm, 3000 rpm and 4500 rpm). In the literature that we analyzed we did not find any differential model for hermetic compressor that managed to fit the experimental points of power and mass flow rate for a large range of revolution speed as our model did.
The next step for the future could be to implement a heat transfer correlation in the energy balance to compute directly the heat released by the compression chamber. In the literature we found very few attempts in this way and so we believed that our model could be a relevant starting point for future work.

8. Solubility model

A basic topic in the development of the new SDE refrigeration cycle is the mass distribution. In this field there are lots of publications regarding the mass content in the condenser and in the evaporator, but very few papers about the refrigerant mass inside the compressor. The reason behind this fact is that the most part of the refrigerant mass is assumed to be located in the two heat exchangers. Anyway the small part of refrigerant in the compressor plays a non negligible role in the whole system simulations of household refrigerators. So a simple model to compute the refrigerant mass that is dissolved in the oil inside the compressor is developed. In particular the focus is on the oil inside of the VEMC9C compressor.

8.1 Literature on the subject

In order to develop a simple model for solubility of the mixture of R600a and alkylbenzenes oil that is contained in the VEMC9C compressor, we studied the literature regarding this topic.
As a part of the effort to create a simple model for solubility of a mixture of R600a and compressor oil, different models were proposed in the last ten years. We selected three relevant papers about the subject.
The first paper of Neto and Barbosa [21] faces the problem of solubility with two different approaches that rely on the phase equilibrium equation. In particular, they propose different methods to calculate the activity coefficients of the liquid phase. Their results show that the simplest approach of Raoult's for ideal solutions is applicable to the R600a-polyol oil (POE ISO 10) solutions. In fact the activity coefficients computed with Heil and Prausnitz and with Flory-Huggins models result to be more or less equal to 1. This fact means that the mixture, as in Raoult's law hypothesis, can be considered an ideal mixture. So at the end they conclude that if we have temperature and pressure of a R600a and polyol solutions we can calculate the solubility very simply using the Raoult's approach.
Another important study on the subject was made by Neto and Barbosa [22] in 2010. The authors propose to calculate solubility through a diffusion model based on Fick's law and then measure the solubility through an experimental campaign. They calculate refrigerant mass solubility through the Peng and Robinson (1976) EoS with a single interaction parameter. So they developed a model for solubility of a mixture of R600a and alkylbenzenes lubricant oil.
Another important study on the topic was made by Sanderson [23]in 2007. In chapter 4 the author, using data provided by the oil manufacturer, developed an experimental correlation to compute the solubility of a mixture of R600a and

JomoFreol S10 mineral oil. The author also plots the results of this correlation in a 3D surface with temperature, pressure and solubility on the axis.
From the first paper we figured out the theoretical background of our solubility model.
In addition this dissertation shows us experimental data to compare the results of our model. In both the papers from Neto and Barbosa[21-22] there are comparison between theoretical models and experimental data. This fact was useful to test how much the outputs of our model correspond to the ones of more sophisticated models.
The last paper gives us solubility values based only on experimental considerations. This paper was important to compare a pure experimental model to our pure theoretical model.

8.2 Theoretical model

Solubility is defined as the mass fraction of a single species in the liquid phase on the total mass of both species in both phases. So solubility is computed with the following formula:

$$\Omega_i = m_i / \sum_i m_i \quad (8.1)$$

The starting point of the model of solubility is the phase equilibrium of every species in the mixture. In theoretical thermodynamic the chemical potential μ_i provides the primary criterion for phase equilibrium. In order to simplify calculations we considered a different property, called fugacity. The fugacity (f_i) of a real gas is an effective pressure which replaces the true mechanical pressure. This parameter represents the pressure of an ideal gas that embodies the same chemical potential as the real gas. This factor takes the place of μ_i, but it does not show the same undesirable characteristics. So we can write the phase equilibrium in terms of fugacity.

$$f_i^V = f_i^L \text{ for } i = 1,2 \quad (8.2)$$

The fugacity of every species (1-R600a and 2-oil) should be the same to be in a equilibrium state.
Now we can take into consideration the vapor phase fugacity.

$$f_i^V(T, P, y_i) = \varphi_i(T, P, y_i) * y_i * P \quad (8.3)$$

If we suppose that our mixture is ideal the fugacity coefficient won't be a function of the molar vapor fraction y_i.

$$f_i^V(T, P, y_i) = \varphi_i(T, P) * y_i * P \quad (8.4)$$

Then we can also make the hypothesis that the vapor is ideal. In this case the fugacity coefficient will be equal to one and we will obtain the following expression for the fugacity of the vapor phase:

$$f_i^V(T, P, y_i) = y_i * P \quad (8.5)$$

Moreover we analyze the fugacity of the liquid phase. In general the fugacity of the liquid phase is computed with the following formula:

$$f_i^L(T, P, y_i) = \gamma_i(T, P, x_i) * x_i * f_i^L(T, P) \quad (8.6)$$

The fugacity of a pure species in the liquid phase ($f_i^L(T, P)$) is calculated as follows:

$$f_i^L(T, P) = \varphi_i * P_i^{sat} * EXP(v_i^{LIQ} * (P - P_i^{sat}) / R * T) \quad (8.7)$$

The exponential term, the so called Poynting factor, is a corrective parameter that shows the effect of the pressure for the liquid fugacity. If the pressure P is not very high, it will have the same order magnitude of P_i^{sat} . In this case the corrective term can be neglected. So for the values of pressure of our model, we can assume that the Poynting factor is negligible. Then we can also make the hypothesis that, as we said before, the vapor could be considered as ideal. In this case we will obtain the following formula to compute the fugacity of the pure species in the liquid phase:

$$f_i^L(T, P) = P_i^{sat} \quad (8.8)$$

So the fugacity of the component in the mixture will be given by the following expression:

$$f_i^L(T, P, y_i) = \gamma_i(T, P, x_i) * x_i * P_i^{sat} \quad (8.9)$$

Taking into account all the hypothesis that we have done, we can re-write the phase equilibrium as follows:

$$f_i^V = y_i * P = \gamma_i(T, P, x_i) * x_i * P_i^{sat} = f_i^L \quad (8.10)$$

Following the approach of Neto and Barbosa[21], we can compute the solubility using the Raoult's law. This approach relies on the hypothesis that we have an ideal solution in the liquid phase. This fact means that the activity coefficient $\gamma_i(T,P, x_i)$ is equal to one. So we obtain the so called Raoult's law.

$$f_i^V = y_i * P = x_i * P_i^{sat} = f_i^L \quad (8.11)$$

Following the approach developed by Neto and Barbosa we also assume that refrigerant is the only species in the vapor phase. Basically we hypothesizes that the oil cannot evaporate. The consequence of this assumption is that $y_1=1$ and so we can compute the molar fraction in the liquid phase very simply using the following formula:

$$x_1 = P/ P_1^{sat} \quad (8.12)$$

We compute very simply the saturation pressures of isobutene at a given temperature using the Antoine's law.

$$P_i^{sat}(T)[kPa] = A - B/(C + T[Celsius]) \quad (8.13)$$

The three coefficients A,B,C were taken from a chemical handbook [8] used. In particular A = 13.8254, B = 2181.79 and C = 248.87.
Finally we calculate the refrigerant solubility from its molar fraction using this simple formula:

$$\Omega_1 = x_1/(x_1 * MM_1 + (1 - x_1) * MM_2) \quad (8.14)$$

Where MM_1 is the Molar Mass of the refrigerant and MM_2 is the molar mass of the lubricant oil.

8.3 Results

Using the Raoult's approach we obtain different results depending on the mixture composition.
On the one hand, we obtain very similar results to the experimental ones of Neto and Barbosa both with the mixture of R600a and polyol oil [21](POE ISO 10) and with the mixture of R600a and alkylbenzenes oil [22]. In fact from Fig. 8.1 and Fig 8.2 we can see that we have comparable trends of bubble point pressure varying solubility for different temperatures.

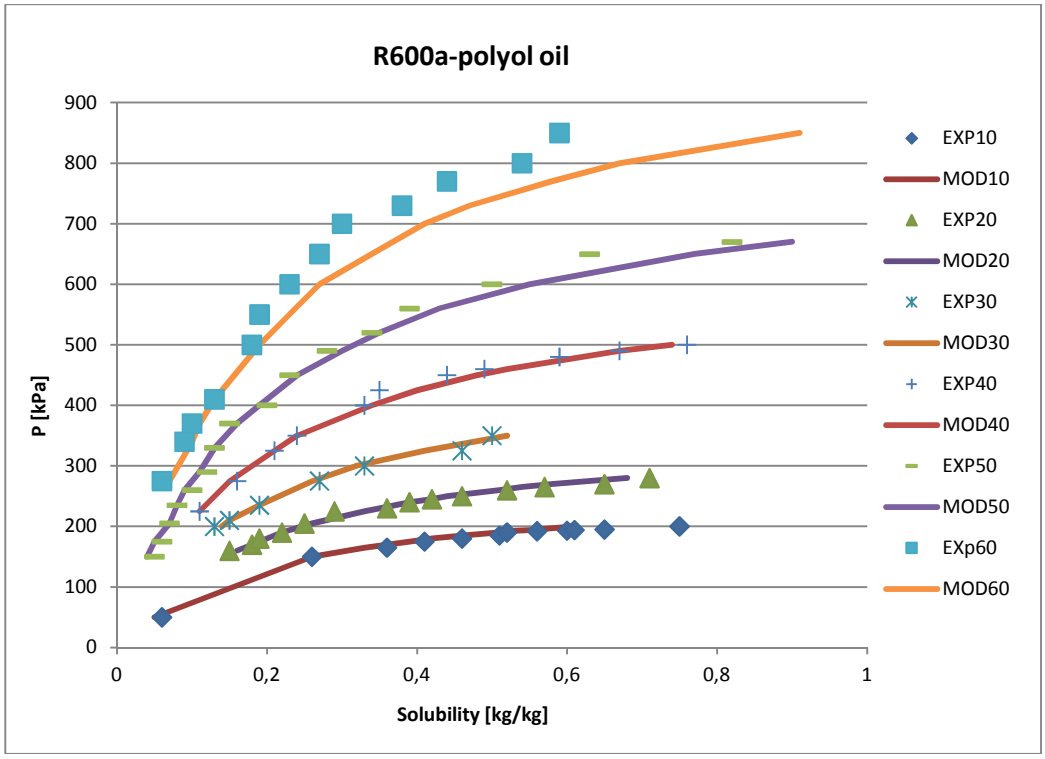

Figure 8.1 Trends of bubble point pressure varying solubility for different temperatures (10 °C, 20 °C, 30 °C, 40 °C, 50 °C, 60 °C) for R600a-polyol oil mixture.

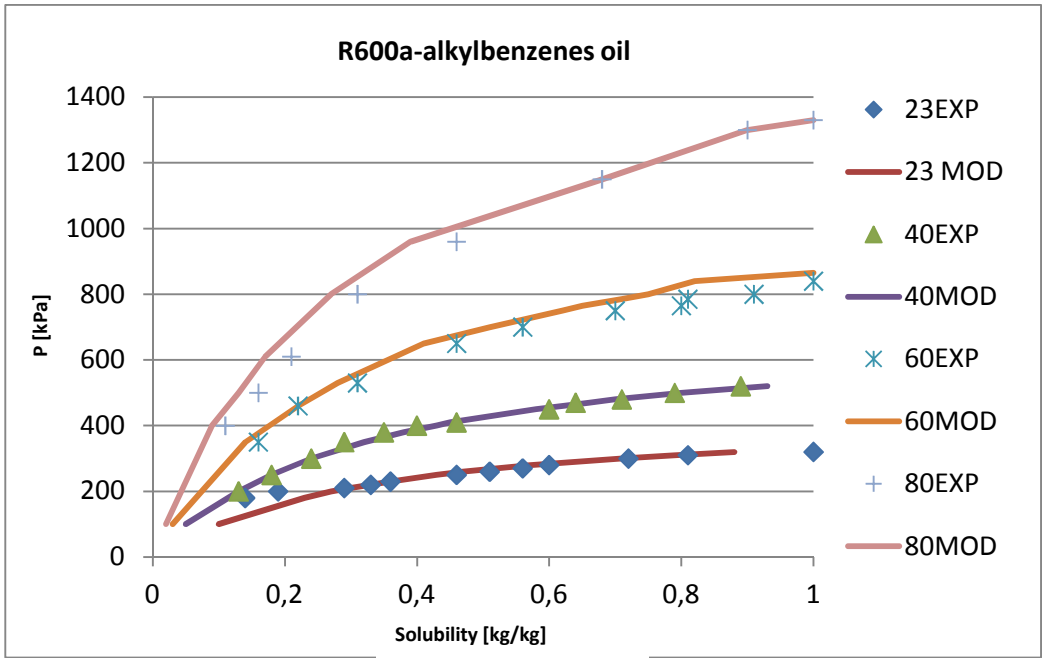

Figure 8.2 Trends of bubble point pressure varying solubility for different temperatures (23 °C, 40 °C, 60 °C, 80 °C) for R600a-alkylbenzenes oil mixture.

These results prove that the hypothesis of ideal solution is applicable to these two mixtures. We also apply this simple model to a mixture of Azmol oil and R600a. The molar mass of Azmol was taken from a study of thermo physical properties of refrigerants [24]. The Raoult's approach showed good results very similar to the ones reported by Zhelezny [25]. In Fig. 8.3 we can see that in this particular case our model fits perfectly the experimental results.

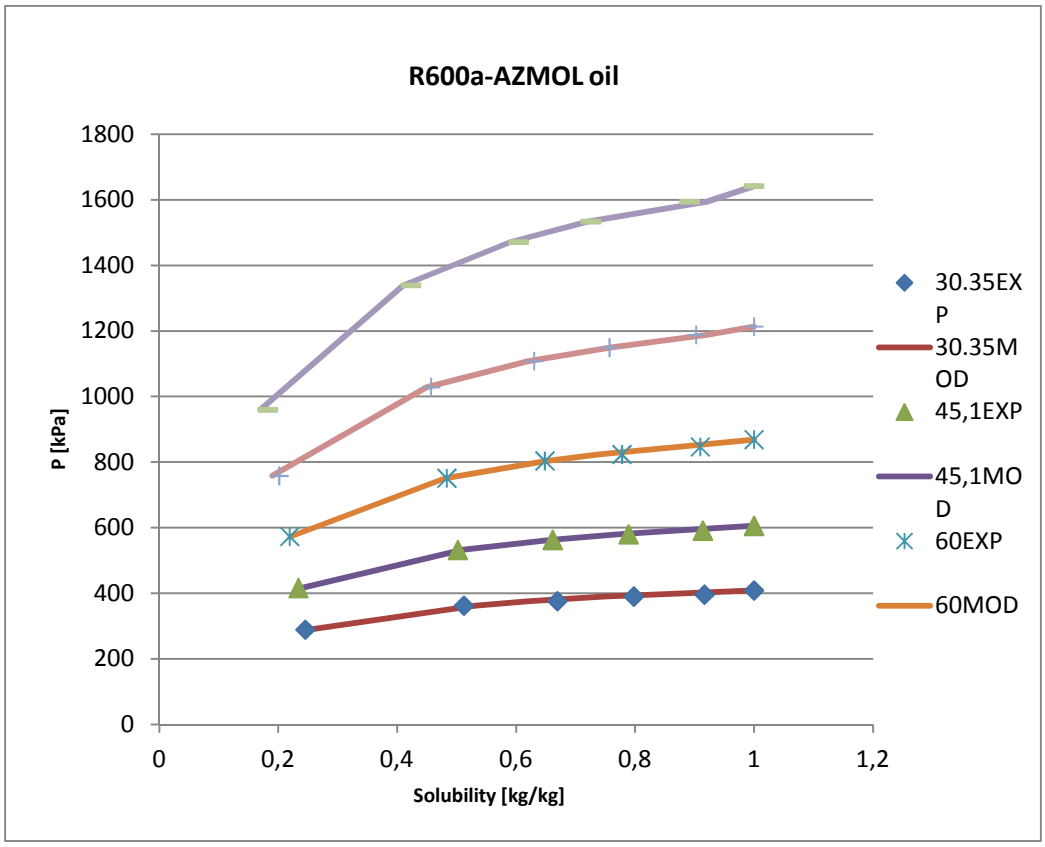

Figure 8.3 Trends of bubble point pressure varying solubility for different temperatures (30.35 °C, 45.1 °C, 60 °C) for R600a-AZMOL oil mixture.

In order to quantify the accuracy of our solubility we calculate the Root Mean Square (RMS) deviation, the Average Absolute Deviation (AAD) and the Bias between the results of our model and experimental data of the mentioned papers. The values are shown in table 8.1.

Table 8.1 Root Mean Square, Absolute Average Deviation and Bias for different mixtures.

R600a-polyol oil		R600a-alkylbenzenes oil		R600a-AZMOL oil	
RMS (%)	1,54	RMS (%)	2,29	RMS (%)	0,68
AAD (%)	9,01	AAD (%)	9,37	AAD (%)	2,63
Bias (%)	2,78	Bias (%)	-2,42	Bias (%)	-1,60

These indicators tell us how much we can consider a mixture as an ideal one. For our purposes we would like to know from this model the solubility with an error from 5% to 20%. In other words we want to estimate the refrigerant mass that is dissolved in the oil for our range of pressure and temperature with an accuracy of ±0.5 g. So for our application, we see that for the three considered mixtures the assumption of ideal behavior is acceptable.
In our household appliance we have a mixture of R600a and alkylbenzenes oil. In particular we want to estimate the solubility in the range of pressures that we reach during the FC and RC operating times and when the compressor is shut down. From the evaporation temperatures of FC and RC and ambient temperature we can deduce the range of pressure interesting for our application. So, considering T_{evapFC} = -30 °C, T_{evapRC} = -5 °C and T_{amb} = 25 °C, we obtain a range of pressure from 40 kPa to 350 kPa. In Fig. 8.4 and in Tab. 8.2 we show the results of the fitting between the predicted and the experimental values for he compressor.

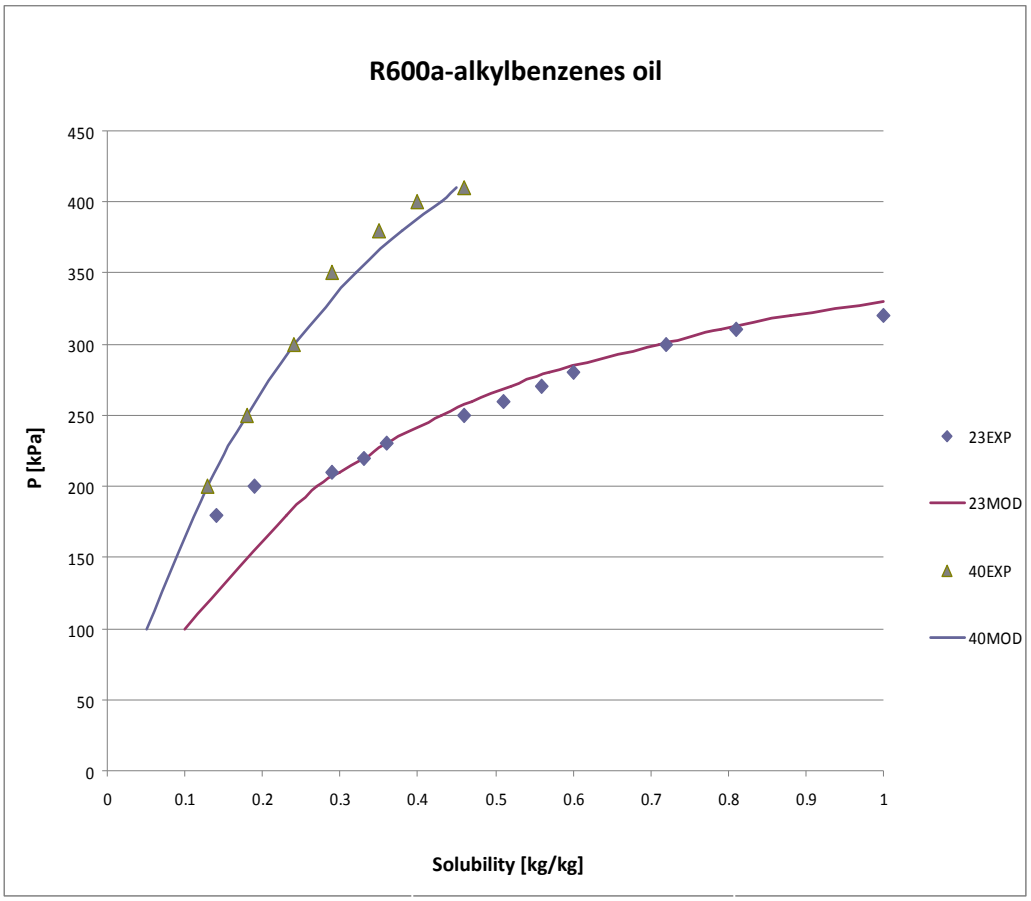

Figure 8.4 Trends of bubble point pressure varying solubility for different temperatures (23 °C, 40 °C) for R600a-alkylbenzenes oil mixture in the range of compressor pressures.

Table 8.2 RMS, ADD and Bias for a mixture of R600a and alkylbenzenes oil in the range of compressor pressures.

R600a-alkylbenzenes oil	
RMS (%)	1.873638
ADD (%)	4.204539
Bias (%)	2.132926

From Fig. 8.4 and from table 8.2 we can see that the ideal mixture model is widely applicable for the range of pressures in which our compressor operates. In fact we have small deviations between the predicted values of Raoult's model and the experimental data.
On the other hand this simple model of solubility is not applicable to mixture of R600a and FREOL S10 mineral oil. In fact we obtain different results from the reliable experimental ones of Sanderson [23]. Moreover the Raoult's model showed unacceptable results also in the case of a mixture of R134a and Polyol ester oil (ICI EMKARATE RL10H). In fact the outputs of our model do not fit with the experimental results obtained by Grando [26].
For these two last mixtures we cannot know the molecular masses of the oils. In fact neither the authors of the papers and the oil manufacturers were able to give us these data. So we try to hypothesize different molecular weights of the oils and we compare the outputs of our model with the experimental data we have. We didn't find any molecular mass that gives us results significantly similar to experimental ones. In Fig. 8.5 we try to vary the molecular mass of the oil for the R134a-EMKARATE RL10H mixture in a realistic range (between 100 g/mol to 700 g/mol) and we show that there are no matches between experimental results and predicted values of our model.

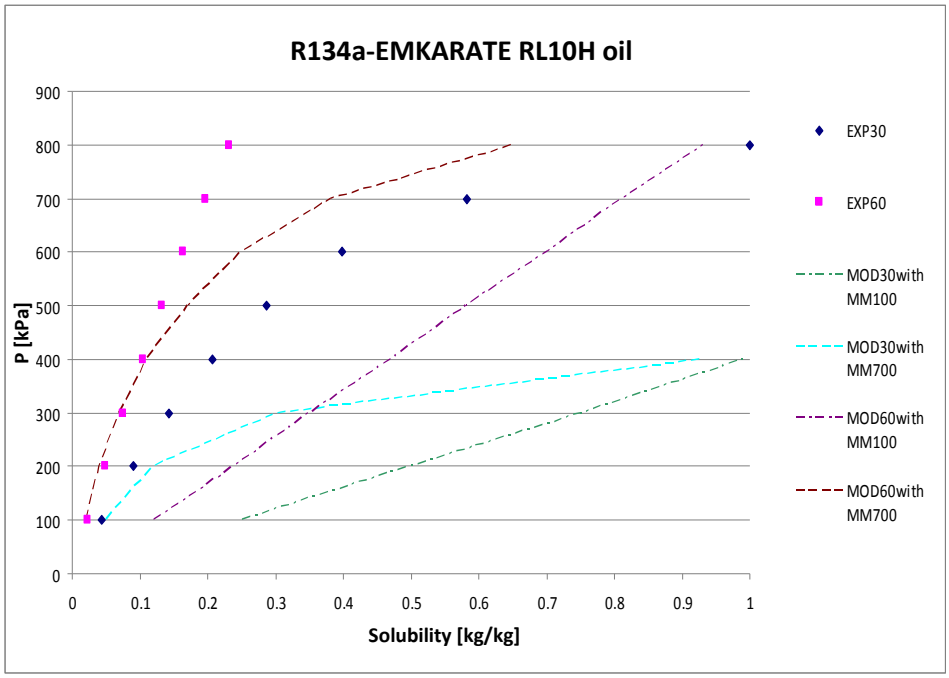

Figure 8.5 Trends of bubble point pressure varying solubility for different temperatures (30 °C, 60 °C) for R134a-EMKARATE RL10H oil mixture with different molecular masses of the oil.

We also apply the same method to the mixture of R600a-FREOL S10 oil. Results are shown in Fig. 8.6

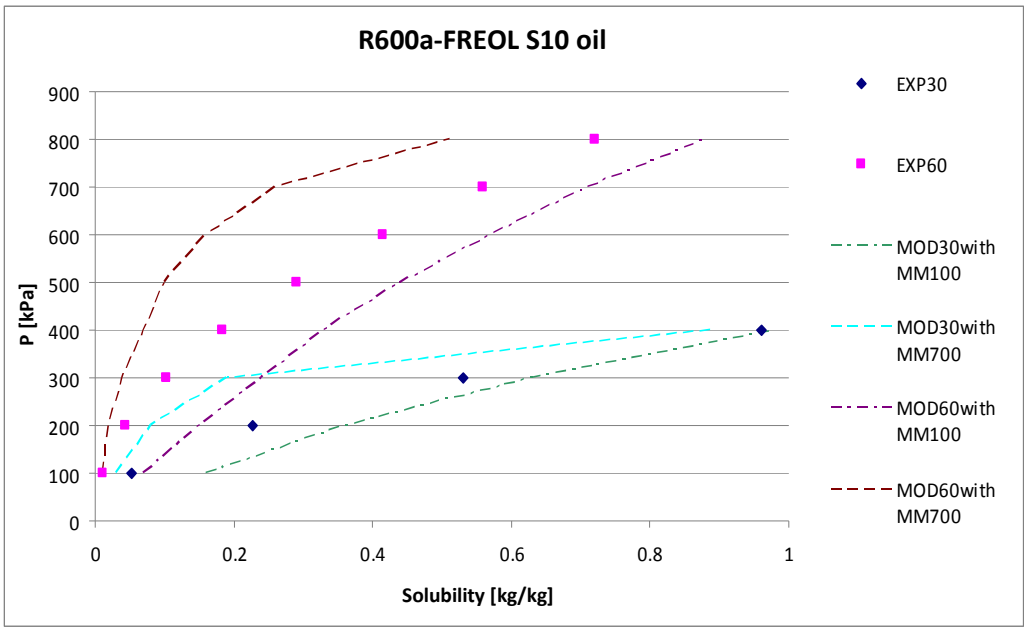

Figure 8.6 Trends of bubble point pressure varying solubility for different temperatures (30 °C, 60 °C) for R600a-FREOL S10 oil mixture with different molecular masses of the oil.

So we can conclude that our model is not applicable to the cases of R600a-FREOL S10 and R134a- EMKARATE RL 10H mixtures.

8.4 Conclusions

We developed a simple model to compute solubility of refrigerant in the compressor oil. This model relied on hypothesis related to the ideality of the considered mixtures. The comparison between the outputs of the model and the available experimental data showed that the model was applicable only to some mixtures of oil and refrigerant. We could assume that these mixtures had quite-ideal behaviors and so Raoult's law could describe them in an accurate manner. These behaviors were probably related to the molecular structure of the considered oils and refrigerants. In the case of ideal mixture we have few effects of miscibility because oil and refrigerant have very different molecular structures and so they do not manage to have strong interaction among them when they are blend.
On the other hand for some other mixtures, like R600a and FREOL S10 oil, we could not apply the Raoult's model because the mixture did not show an ideal behavior. In this cases if we study the molecular structures of the oil and the refrigerant we will probably know that molecules in the mixture build strong interactions among them.

9. Cycle simulation model

9.1 Introduction

In this section we try to merge all the results of the previous chapters through a simulation of the entire thermodynamic cycle. The aim of this section is to predict the energy consumptions of the RC cabinet of the SDE prototype. In order to achieve this goal, we merge the differential model of the compressor to an available stationary model of the cycle. This model represents the refrigeration system (energy system) as a group of different physical components that exchange information between them through particular methodologies based on the global balance equations of mass, momentum and energy. This modular approach considers each component as a ‘‘black box’’ with its peculiar inputs and outputs. The model relies on the simplest steady-state modelling approach for refrigeration circuit. The model embodies both the differential compressor model explained in chapter 7 and some overall heat transfer coefficients of compressor shell, condenser and evaporator measured by M. Visek[7]. The model is based on several standard assumptions about the refrigeration circuit: no pressure drop in heat exchangers, isenthalpic expansion in capillary, negligible kinetic and potential energy, constant efficiency of suction line capillary tube heat exchanger. The model is made of four main components: capillary tube suction line heat exchanger, compressor, evaporator and condenser. Each component includes the three balance equations (mass, momentum and energy). Since this model adopts a steady state approach, the mass balance equations are implicitly satisfied assuming a single mass flow rate in the entire cycle. Since we assume to have no pressure drops, no kinetic and potential energies, the momentum balance equations are neglected. Finally every component should fulfil its relative energy balance equation. The model has seven inputs that we can set in every simulation: ambient temperature, power of the RC fan, freezing temperature of the PCM, RC time averaged air temperature, SH_{RC} (RC Super Heating), SC_{RC} (RC Sub Cooling) and $UA_{air\text{-}EVAP\_RC}$. SH_{RC} represents the temperature difference between the exit of the evaporator and the compressor inlet. SC_{RC} symbolizes the temperature difference between the condenser outlet and the entrance of the capillary tube. $UA_{air\text{-}EVAP\_RC}$ correspond to the overall air heat transfer coefficient between the cabinet back surface where we have the foamed-in evaporator and the internal air of the refrigerator. The model predicts the energy consumption per day and the COP of the appliance.

In this chapter we will use the stationary model for two different targets. On the one hand we run the simulations in the same measure conditions of chapter 3 to make a comparison between the predicted and the experimental values of energy

consumptions, COP and compressor run time. On the other hand we will use the $UA_{air\text{-}EVAP\_RC}$ values that we measured in chapter 4 as inputs for the stationary model to simulate the behaviour of a possible refrigerator prototype where we adopt both the PCM and the new fans and multiflows.

9.2 Testing the stationary model

The aim of this section consists in understanding the accuracy of the predicted values by the cycle stationary model. We run the simulations for all the conditions where we measured the consumptions in chapter 3. In particular we decide to assume a super heating equal to 10 °C and a sub cooling equal to 5 °C as Visek did [7]. In Fig. 9.1 we show the comparison between the predicted and the experimental values of the energy consumptions during a day for different freezing temperatures of the PCM (0 °C, -2 °C, -4 °C) and different time averaged RC air temperatures.

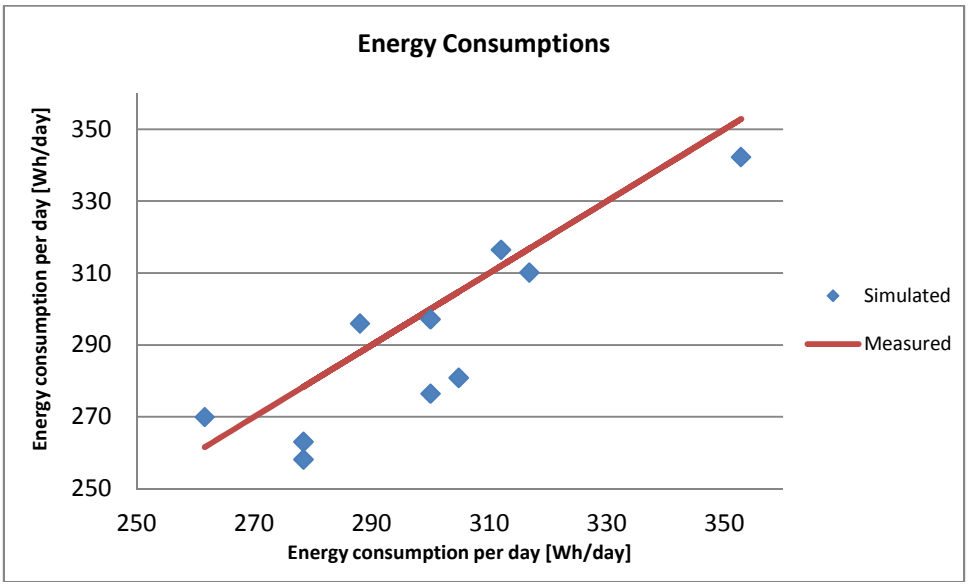

Figure 9.1 Comparison between predicted and experimental values of the energy consumption per day of the prototype.

As we can see in Fig. 9.1 the stationary model manages to predict the energy consumptions in an accurate manner. In fact the results of the simulations fit the experimental measures with an AAD equal to 4.2 % and a absolute maximum deviation of 7.8 %. Moreover in Fig. 9.2 we show the comparison between the results of the model and the measurements related to the COP in the different cases.

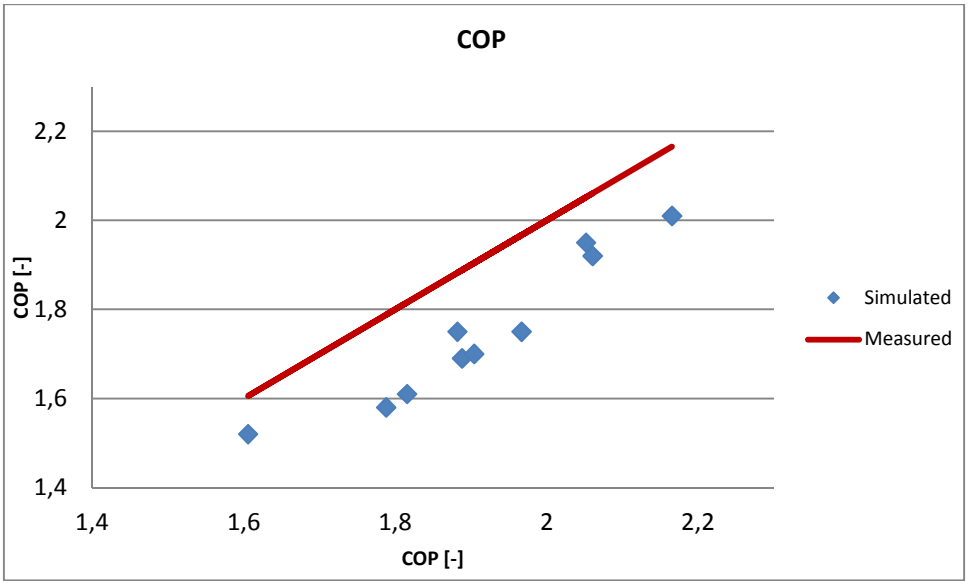

Figure 9.2 Comparison between predicted and experimental values of the COP of the prototype.

As we can see in Fig. 9.2 the model tends to underestimate the COP. In particular it manages predict the experimental values with an AAD equal to 8.6 % and a absolute maximum deviation of 11.6 %. So such a stationary model manages only to provide a preliminary estimation of the COP. In particular this behavior seems to be caused by a wrong estimation of the RC thermal load. This load is estimated using the external ambient temperature, the internal air temperature in the RC cabinet and a constant value of thermal resistance for the walls of the refrigerator. Since in the reality the RC air temperature continuously varies between the upper and the lower bounds of the control system, the assumption embedded in the stationary model about the stability of the RC internal temperature probably produces the discrepancy between the predicted and the experimental values of COP.
The comparison between the experimental and the predicted values of energy consumptions per day and COP provides a picture of the advantages and disadvantages of the stationary model. On the one hand, the model is accurate only in predicting the refrigerator consumptions, on the other hand it can help the users to have a preliminary estimation of the performances of the appliance.

9.3 Estimations for future improvements

In this section we apply the stationary model to understand the possible improvements related to the adoption of the fan and the multiflows tested in chapter 4 in the existing prototype with the embedded PCM. We will run the simulation with the RC internal air temperature equal to 5 °C and the external

ambient temperature equal to 25 °C as in the energy consumption tests. We test the coupling of fans and multiflow with the PCM in the best configuration individuated in chapter 3. So we decide to run the model using water as PCM and the compressor frequency equal to 54 Hz. Finally we decide to simulate the best configurations obtained coupling each fan and multiflow at different voltages. We run each test using the input values of $UA_{air\text{-}EVAP\_RC}$ that we measured in the previous tests reported in chapter 4. In Fig. 9.3 we display the results of the simulations.

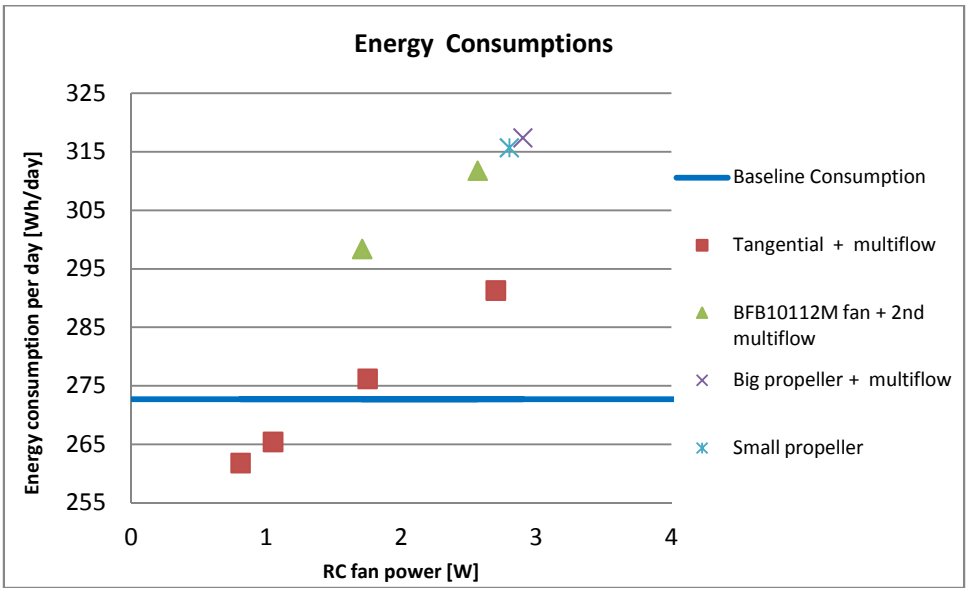

Figure 9.3 Predicted values of energy consumption per day for the simulated prototype with water as PCM and compressor frequency equal to 54 Hz.

The baseline consumption represents the case of a prototype with only a PCM (freezing temperature equal to -1 °C) in the RC cabinet without any fan or multiflow. As we can see in Fig. 9.3, the tangential blower coupled with the multiflow is the only fan that manages to reduce the overall energy consumptions of the refrigerator. The tangential fan provides predicted energy savings of 4.0 % (at 9 V) and of 2.7 % (at 10 V). So the tangential fan has a positive impact on the total consumptions only at low powers (i.e. 9 V and 10 V supply voltages). In fact we showed in chapter 4 that the tangential fan blows the air more efficiently at low voltages. All the other fans do not manage to lower the energy consumptions. On the one hand, the adoption of a fan increases the heat transfer between the back wall of the cabinet and the internal air. On the other hand, the utilization of a fan implies additional energy consumptions. In particular the fan has a double impact on the energy performance. It requires some power to be run and it represents an additional thermal load inside the RC cabinet. These are the reasons, for example, because the standard fan is normally switched off during the energy consumption test even if we showed that it

enhances the heat exchange between the back wall and the RC cabinet air. Furthermore from Fig. 9.3 we can conclude that the standard and the centrifugal fans should not be consider to increase the heat transfer inside a future prototype.

9.4 Conclusions

In this chapter we applied a stationary model to simulate the behavior of the appliance. In particular we discovered that such kind of model managed to predict accurately the real energy consumptions, while it only provided a preliminary picture about the COP. We also tried to simulate a new configuration of the refrigerator where we merged the experimental measurements taken in chapter 4 in the stationary model forecasts. We found out that the adoption of a tangential blower inside the cabinet could represent a future direction to reduce the consumptions. In particular we underlined that the tangential fan could lower the consumption of 4.0 % from the baseline case where we run the compressor at 54 Hz with water as PCM. In the future we propose to build a prototype of a SDE refrigerator with a PCM and a tangential blower. In particular we suggest to make a deep CFD analysis of the air flows into the cabinet to design and to optimize the coupling of the fan and the back wall. Moreover we also believe that the adoption of tangential fans should be also implemented in appliances without PCM. In this cases we expect to have similar reductions of the energy consumptions. Furthermore, while the PCM implies non negligible costs related to the production process, the tangential fans show very good characteristics from the economic point of view. In fact, these devices reveals to be cheap and reliable. Finally we also propose to run an acoustic analysis on such kind of fans to understand the possible problems related to the acceptability of the new product by customers.

10. Conclusions and future developments

In this thesis we decided to study the SDE refrigeration technology for the household appliances that showed good characteristics related to the reduction of the energy consumptions.
The first part of the work focused on experimental activities related to the optimization of the freezing temperature of a PCM positioned on the back wall of the RC cabinet. We created the experimental apparatus to acquire all the relevant parameters of an available SDE prototype. We built up the electronic circuit that allowed us to measure the pressures, the temperatures and the compressor power of the refrigerator. We connected this hardware to three different NI boards that passed the physical signals to a Labview software. Using this software we were able to acquire and save the relevant test factors on a personal computer. So we ran several tests to optimize the freezing temperature of the PCM in the "energy consumption test" conditions expressed by the standard EN ISO 15502. The final result of this experimental campaign consisted in the identification of the PCM freezing temperature that minimized the energy consumptions of the appliance. We individuated an optimum freezing temperature equal to - 1°C.
Moreover we conducted another experimental campaign about the heat transfer between the foamed-in evaporator and the RC cabinet air. We focused our attention on the air side heat transfer testing different fans and multiflows (i.e. air channels) positioned on the back wall of the cabinet. We started to measure the air speeds provided by the standard fans and multiflows installed in the refrigerator and then we selected and tested also a centrifugal and a tangential fan with some designed multiflows. We concluded that the tangential fan showed the best characteristics in terms of improvements of the air heat transfer coefficient on the back wall.
In the next four chapters of the thesis, we developed a new compressor model to predict accurately the required compressor power, the refrigerant mass flow rate and the quantity of refrigerant dissolved in the lubricant oil. We created both a polytrophic and a differential model for the compressor and we finally made a comparison between the predicted values of the outputs to understand the advantages and the limits of every model. Furthermore we also produced a simple and effective solubility model of the refrigerant in the VEMC9C compressor oil based on the Raoult's law.
In the last chapter we included the compressor model in the available stationary simulation of the SDE refrigerator to predict the energy consumptions of the prototype. The first step consisted in testing the model comparing the simulated values of energy consumption per day and COP with the experimental ones that we measured in chapter 2. Moreover we tried to simulate the energy

consumptions of a possible future SDE prototype that embodies both the PCM and the tangential fan in the RC cabinet.
At the end of this work we would like to underline two different directions for future improvements. On the one hand, we propose to produce a new SDE prototype merging the positive characteristics of the PCM and the tangential fan in terms of reduction of energy expenses. This prototype should be based both on the results of this thesis and on a deep CFD analysis of the air flows in the RC cabinet. On the other hand, we believe that the creation of a dynamic model for the SDE refrigerators could be a crucial step for further improvements. This model could include the differential compressor model of this thesis, but still lots of work is required to model and harmonize the behavior of all the other components of the refrigerator.

Nomenclature

Main symbols

AAD	Average Absolute Deviation.
AED	Alternative Evaporator Duty cycle.
CAP	Cooling Capacity.
C_d	Correction Coefficient for the area of compressor the Discharge.
COP	Coefficient of Performance.
cov	Co-variance.
C_s	Correction Coefficient for the area of the compressor Suction.
$\overline{\overline{D}}$	Strain deviator tensors.
div	Divergence.
E_{BB}	Black Body Emissive power
EEI	Energy Efficiency Index.
EES	Engineering Equation Solver.
EU	European Union.
f_i	Fugacity of the i component.
F_{ij}	View Factor between the i surface and the j surface.
FC	Freezer Compartment.
G	Irradiation.
Gr	Grashof's number.
GWP	Global Warming Potential .
J	Radiosity.
k_{ft}	Cryoscopic constant.
LBP	Low Back Pressure.
m_i	Mass of the i component.
MM	Molar Mass.
n	Exponent of the real polytropic process.
N_{cyl}	Number of cylinders of reciprocating compressor.
NI	National Instruments.

NTC	Negative Temperature Coefficient.
Nu	Nusselt's number.
ODP	Ozone Depletion Potential.
PCM	Phase Change Material.
P_{elet_0}	Electrical losses correction factor for the compressor power.
P_i^{sat}	Saturation pressure of the i component at a fixed temperature.
P_{mecc_0}	Mechanical losses correction factor for the compressor power.
Pr	Prandtl's number.
Ra	Rayleigh's number.
RC	Refrigerator Compartment.
Re	Reynold's number.
RMS	Root Mean Square.
rpm	Round per minute.
SDE	Sequential Dual Evaporator.
SEDS	Single Evaporation Dual Source.
SLHX	Suction Line Heat Exchanger.
T_{ai}	Standard ambient temperature in the position i according to EN ISO 15502.
$\overline{T_{amb}}$ test	Standard ambient temperature of the refrigerator cabinet during a according to EN ISO 15502.
T_{pcmi}	Temperature of the Phase Change Material in the position i.
tr	Matrix trace .
$\bar{\bar{T}}$	Strain tensor.
T_{RC}	Refrigerator cabinet internal temperature.
$\overline{T_{RC}}$	Refrigerator cabinet internal temperature during a test according to EN ISO 15502.
$UA_{air\text{-}EVAP\_RC}$	Overall air heat transfer coefficient between the cabinet back surface and the internal air of the refrigerator.
V_{cyl}	Displacement of every cylinder of reciprocating compressor.
$w_{discharge}$	Compressor cylinder outlet flow rate.
W_{fm}	Total power related to the mass forces.

W_{fs}	Total power related to the superficial forces.
$W_{revC/E}$	Total reversible work of compression or expansion.
$w_{suction}$	Compressor cylinder inlet flow rate.
x_i	Molar liquid fraction of the i component.
y_i	Molar vapour fraction of the i component.

Relevant Greek letters

α_P	Proportional correction factor for the compressor power.
α_{vol}	Proportional correction factor for the volumetric efficiency.
β	Compression ratio.
γ	Exponent of the ideal polytropic process.
γ_i	Activity coefficient of the i component.
γ_P	Correction factor related to the pressure ratio for the power.
γ_{vol}	Correction factor related to the pressure ratio for the volumetric efficiency.
ϵ	Emissivity.
η_{ex}	Exergetic efficiency.
η_{iso}	Isentropic efficiency.
ϑ_{vol}	Volumetric efficiency.
ϑ_{vol_0}	Correction factor related to the leakages for the volumetric efficiency.
μ_i	Chemical potential of the i component.
φ_i	Fugacity coefficient of the i component.
Φ_D	Total dissipation function.
$\Phi_i^{ADV(j)}$	Flux number i of the species j.
Φ_{neti-j}	Net radiative heat flux from the i surface the j surface.
Φ_T	Total Thermal Flux.
$\overrightarrow{\varphi_T}$	Punctual heat flux vector.
Ω_i	Solubility of the i component.

Bibliography

[1]P. Bertoldi, B. Hirl, N. Labanca, Electricity Consumption and Efficient Trends in the EU-27 - Energy Efficiency Status Report 2012 [Report] - Ispra: JRC Scientific and Technical Reports, 2012

[2] A. Ors, Investigation of two performance improvement options for household refrigerators // Master of Science Thesis, University of Maryland (2006)

[3] Park J. K., Park, S. T., Kwak, T. H., Im K. S., Dual-Controlled Indirect Cooling Refrigerator/Freezer Using Two Capillary Tubes and an Air Flow Switching System // Purdue International Refrigeration Conference, R-12, 1998.

[4] Lorenz, A., Meutzner, K., On Application of Non-azeotropic Two Component Refrigerants in Domestic Refrigerators and Home Freezers // XIV International Congress of Refrigeration, Moscow, 1975.

[5] Simmons K. E., Haider I. and Radermacher R. Independent Compartment Temperature Control of Lorenz-Meutzner and Modified Lorenz-Meutzner Cycle Refrigerators [Journal] // ASHRAE Transaction. - 1996. - pp. 1085-1092.

[6] Lavanis, M., Haider, I., Radermacher, R., Experimental Investigation of an
Alternating Evaporator Duty Refrigerator/Freezer // ASHRAE Transactions 1998, Vol. 104, P. 2.

[7] M. Visek, Study of innocative techniques aismed at reducint everngy consumption in domestic refrigeration systems // Doctoral dissertation, Politecnico di Milano (2013)

[8] J.M. Smith, H.C. Van Ness, M. M. Abbott, Introduction to chemical engineering thermodynamics, McGraw Hill Internation Edition (2005)

[9] F. P. Incropera, D. P. Dewitt, T. L. Bergmna, A. S. Lavine, Fundamentals of Heat and Mass Transfer [Book] // John Wiley & Sons, sixth edition (2007), pp. 583-584

[10] A. Jakobsen, B. D. Rasmussen, Review of Compressor Models and Performance Characterizing Variables // International Compressor Engineering Conference (2000), Paper 1429

[11] J.S. Van der Meer, S. W. Brok, S. Touber, Modelling of Cylinder Heat Transfer - Large Effort, Little Effect? // International Compressor Engineering Conference (1980), Paper 305

[12] R. P. Adair, E.B. Qvale, J.T. Pearson, Instantaneous heat transfer to the cylinder wall in reciprocating compressors // International Compressor Engineering Conference (1972), Paper 45

[13] A. Cavallini, L. Doretti, G.A. Longo, L. Rossetto, B. Bellao, A. Zannerio, Thermal Analysis of a Hermetic Reciprocating Compressor // International Compressor Engineering Conference (1996), Paper 1160

[14] A. Cavallini, D. Del Col, L. Doretti, L. Rossetto, G.A. Longo, A. D. Pinto , A. Zannerio, Unsteady-State Analysis of the Compression Cycle of a Hermetic Reciprocating Compressor // International Compressor Engineering Conference (1998), Paper 1353

[15] M. L. Todescat, F. Fagotti, A. T. Prata, R. T. S. Ferreira, Thermal Energy Analysis in Reciprocating Hermetic Compressors // International Compressor Engineering Conference (1992), Paper 936

[16] W. J. D. Annand, Heat Transfer in the Cylinders of Reciprocating Internal Combustion Engines // Proc. of J. Mech. Engrs. (1963), vol. 117 , pp. 973-996

[17] A. Galliani and E. Pedrocchi, Analisi exergetica [Book] // Milano - Polipress (2006), pp. 119-124

[18]C. J. L. Hermes, C. Melo, How to get the most out from a reciprocating compressor semi-empirical model using a minimum data set // International Conference on Compressor and Coolants, Papiernicka, Slovak Republic (2006)

[19] E.Winandy, C. Saavedra O. , J. Lebrun,Simplified modeling of an open-type reciprocating compressor// International Journal of Thermal Science (2001)

[20] C. J. L. Hermes, Uma metodologia para a simulacao transiente de refrigeradoresdomesticos// Universidade Federal de Santa Catarina (2006), Florianopolis, SC, Brasil

[21] Moises A. Marcelino Neto, Jader R. Barbosa, Solubility, density and viscosity of a mixture of R-600a andpolyol ester oil //International journal of refrigeration 31 (2008) 34 - 44

[22] Moises A. Marcelino Neto, Jader R. Barbosa,Abosorption of isobutane (R600a) in lubrificant oil // Chemical Engineering Science 66 (2011) 1906 – 1915

[23] Cara Sanderson Martin, Investigation of refrigerant distribution in household refrigerator with a focus on the role of accumulator // Master of Science Thesis, University of Maryland (2007)

[24] Yury V. Semenyuk, Vitaly V. Sechenyh, Vitaly P. Zhelezny, Pavel V. Skripov, Thermophysical properties of compressor oils for refrigerating plant, Journal of synthetic lubrification 25 (2008) 57 – 73

[25] Petr V. Zhelezny, Vitally P. Zhelezny, Denis A. Procenko, Sergey N. Ancherbak, An experimental investigation and modeling of the thermodynamic properties of isobutene-compressor oil solutions: some aspects of experimental methodology, International journal of refrigeration 30 (2007) 433-445

[26] F. P. Grando, M Priest and A. T. Prata, Lubrication in refrigeration systems: Numerical model for piston dynamics considering oil-refrigerant interaction // Proceedings of the Institution of Mechanical Engineers, Part J: Journal of Engineering Tribology 2006 220: 245